SPATIAL CHARACTERIZATION OF THE NATURAL MECHANICAL VIBRATIONS OCCURRING IN-VIVO DURING ISOMETRIC CONTRACTIONS OF THE BICEPS BRACHII MUSCLE: TOWARDS PASSIVE ELASTOGRAPHY OF SKELETAL MUSCLES

A Dissertation
Presented to
The Academic Faculty

by

Akibi A. A. Archer

In Partial Fulfillment
of the Requirements for the Degree
Doctor of Philosophy in the
George W. Woodruff School of Mechanical Engineering

Georgia Institute of Technology
December 2012

SPATIAL CHARACTERIZATION OF THE NATURAL MECHANICAL VIBRATIONS OCCURRING IN-VIVO DURING ISOMETRIC CONTRACTIONS OF THE BICEPS BRACHII MUSCLE: TOWARDS PASSIVE ELASTOGRAPHY OF SKELETAL MUSCLES

Approved by:

Dr. Karim G. Sabra, Advisor
George W. Woodruff School of
Mechanical Engineering
Georgia Institute of Technology

Dr. Micheal Leamy
George W. Woodruff School of
Mechanical Engineering
Georgia Institute of Technology

Dr. Minoru Shinohara
School of Applied Physiology
Georgia Institute of Technology

Dr. Dave Muir
School of Electrical Engineering
University of Technology, Jamaica

Dr. Jun Ueda
George W. Woodruff School of
Mechanical Engineering
Georgia Institute of Technology

Date Approved: August 09 2012

ACKNOWLEDGEMENTS

I would like to first give thanks to the Creator, because without the Creator none of this work would be possible. There were many people that have supported me during my studies while at the Georgia Institute of Technology, I will be forever grateful of their support. My research work would not have been possible without them. My family and friends have been a continuous support system for me throughout my academic career. I would like to thank my parents for pushing me to excel and knowing that I can. The encouragement of my family and friends kept me going through times that were challenging. To them I give the most thanks. I would like to give thanks to my dissertation committee comprising of Dr. Karim G. Sabra, Dr. Minoru Shinohara, Dr. Michael Leamy, Dr. Dave Muir and Dr. Jun Ueda. My deepest gratitude is to my advisor, Dr. Karim G. Sabra whose knowledge and expertise guided me through the research process. I would also like to thank my lab mates for their assistance with different portions of my research project. A special thanks goes to Ashley N. Johnson who steadily assisted me with the progression of my research. Also to Perry Atangcho and Malika Grayson, who assisted me with collecting and analyzing data for my research. There were other people at the Georgia Institute of Technology that made my life easier, who were not directly related to research. In that regard I would like to thank Dr. Camellia Henry, Terri Keita, Trudy Allen and Glenda Johnson. Last but not least I would like to give thanks to my ancestors whose scientific expertise and understanding has been instilled in me and given me the necessary commitment and strength to succeed.

TABLE OF CONTENTS

LIST OF TABLES

LIST OF FIGURES

CHAPTER I

INTRODUCTION

1.1 Background

1.1.1 Skeletal Muscles Physiology

Skeletal muscles are tailored for force generation and movement in the human body. Due to the relationship of structure-function of the skeletal muscle, muscle's structure must also be taken into consideration when studying muscle function. All skeletal muscles attach to connective tissue (tendons) in order to connect to the bone. The skeletal muscle architecture can be defined as the arrangement of muscle fibers relative to the axis of force generation [42].

For example, the biceps brachii studied in this thesis has muscle fibers that extend parallel to the axis of force generation and are defined as longitudinal or parallel muscle. In addition to the muscle architecture, human skeletal muscles contain a mixture of muscle fiber types and motor units, such as heterogeneous muscles containing slow contracting (high endurance) and fast contracting (low endurance) fibers. The proximal end the biceps brachii has two distinct muscle fiber groups; the short head which originates at the tip of the coracoid process and the long head which originates at the supraglenoid tubercle. Both heads of the muscle join together and have an insertion point at the radial tuberosity (see Fig. 1). The biceps brachii (at least in its lower section) is fusiform (wide in the middle and is tapered at the ends) with almost parallel muscle fibers (see Fig. 1) [33]. The specific tendons that drive the elbow flexion mechanism, attaching the biceps to the skeleton, differ at the extremities. The origin tendons of both bicep heads attach separately to the relatively fixed bone of the articulation (at the shoulder scapula). The insertion tendon is attached

to the moving part of the articulation (at the humerus) (Fig. 1).

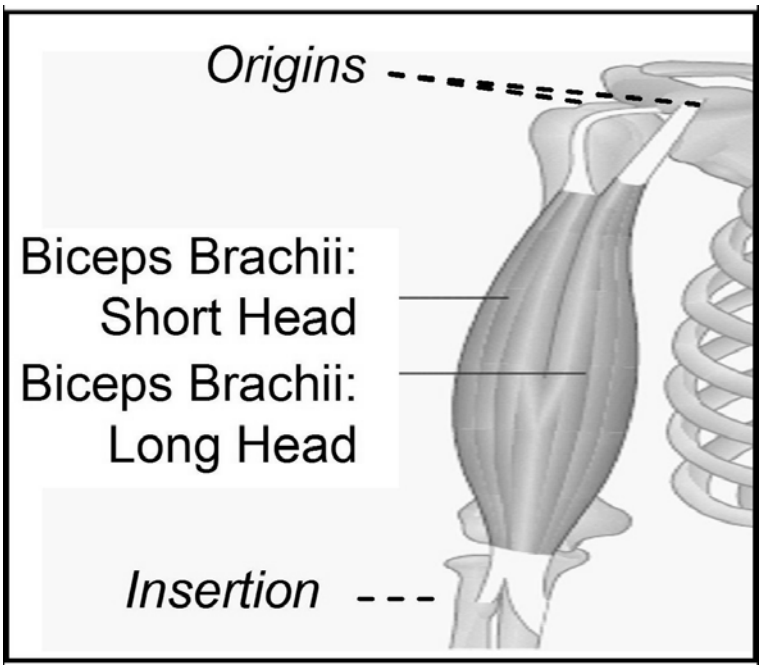

Figure 1: Anatomical drawing of the biceps brachii muscle (adapted from [33]).

In addition to the physiology of the skeletal muscle, the conditions under which the muscle is tested is also important. Meaning, the position of the muscle, voluntary or involuntary contractions and dynamic or isometric conditions all play a role in how the muscle behaves.

Throughout this dissertation, the testing conditions are isometric and voluntary contractions. In physiological terms, an isometric contraction is a contraction where the muscle length does not change. This type of contraction can be experimentally tested in-vitro on a dissected muscle, but because of the semi-elastic properties of tendons, a constant muscle length can not be assured in-vivo. Therefore for this dissertation, an isometric muscle contraction is defined as a muscle contraction at which the joint angle of which the muscle is operating does not change. The joint muscle of interest in this dissertation is the biceps brachii, and the kinesiological

articulation of interest is elbow flexion with an angle of 90 degrees (angle between the humerus and the ulna). In addition, in this dissertation, all of the contractions are voluntary contractions.

During sustained voluntary contractions, there are a few factors that can influence measurements. In general, muscle fatigue has a complex nature during voluntary contractions. To produce voluntary contractions, at least four major anatomical components are involved: the central nervous system, the peripheral nerve, the neuromuscular junction, and the skeletal muscles. Fatiguing can be initiated at any one of these components. As it may be assumed, low-force voluntary contractions can be maintained longer than high force contractions.

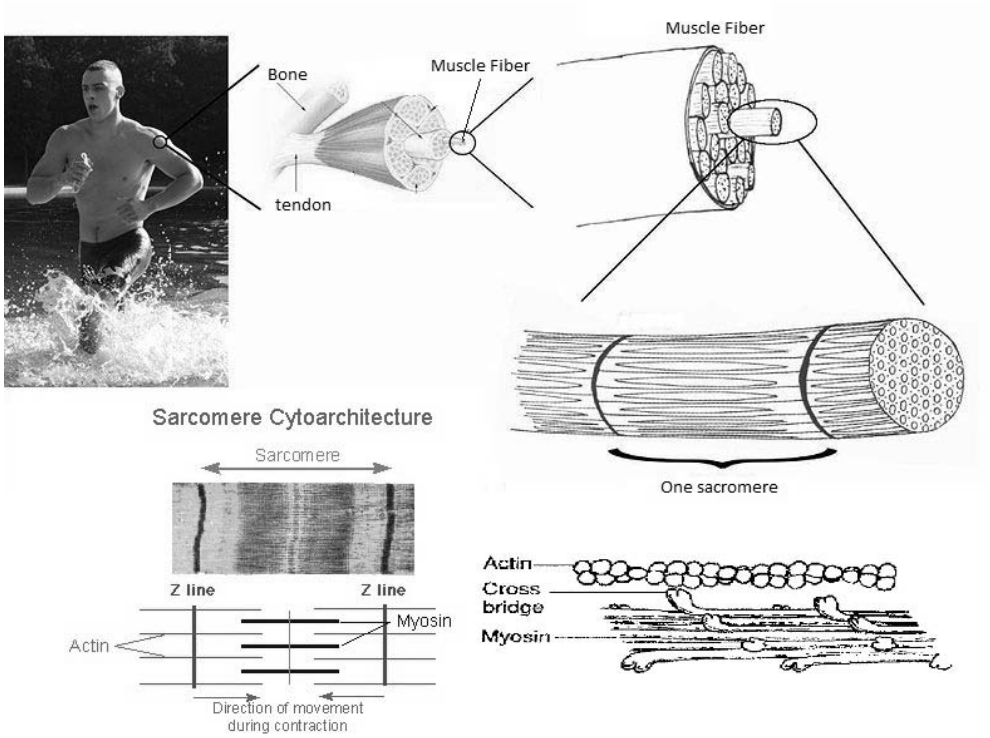

Figure 2: Anatomical breakdown of skeletal muscle from whole limb to actin and myosin level including cross-bridge (adapted from [49]).

It is well known that the properties of skeletal muscle change under different

conditions. For example, a person can feel that their muscle feels harder the more they contract the muscle. The main reason that skeletal muscle changes properties is to reflect a change in the muscle activation level. For instance, muscles typically feel 'harder' during contraction due to a physiological change, the shortening of the acto-myosin filaments composing the striated muscle fibers [37]. It can be seen in Figure 2 how the acto-myosin filaments make up the sarcomere and it also indicates the direction of movement of the filaments during a contraction. The cross-bridge between the actin and myosin filaments are responsible for the force production and thus have an effect on the stiffness of the muscle. With this being said, the macroscopic viscoelastic properties of muscles are directly related to the tension provided by the muscle fibers [48].

1.1.2 Surface Mechanomyogram (S-MMG)

During muscle contraction there is a reduction in length along the long axis of the muscle contractile element [78], due to the movement of the acto-myosin filaments. The skeletal muscle can be modeled as having no change in volume during contraction [8], therefore the shortening in the length along the parallel axis of the muscle is coupled with geometrical changes in the transverse axis dimension. The changes in the transverse axis dimension cause vibrations that can be sensed at the skin's surface. Because of this, low frequency (<100 Hz) and continuous surface mechanical oscillations, also called "muscle noise", are naturally generated by skeletal muscle. Typical sensors used to record these mechanical oscillations are skin-mounted accelerometers, condenser microphones, or laser displacement sensors [54, 67, 68, 80]. This dissertation measures these vibrations by using accelerometers at the surface of the skin above the biceps brachii muscle. Independent of the type of sensors used, recordings of muscle mechanical oscillations with these sensors are called surface mechanomyograms (S-MMGs) (See. Fig 3)[53].

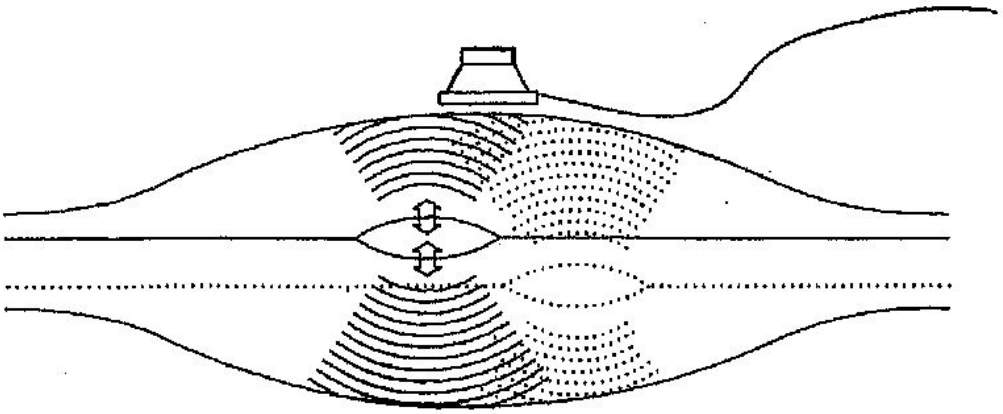

Figure 3: Schematic representation of the hypothesized MMG generation process resulting from vibrations generated by dimensional changes of the active muscle fibers during (fluctuations of) voluntary contractions ([53]).

S-MMGs have been used recently for numerous muscle related objectives, for example: 1) muscle fiber typing in sports medicine [57], 2) to investigate the effect of neuromuscular diseases on muscle [3], and 3) to investigate the effect of aging [26] on muscle. S-MMGs appear to be a good index for force and fatigue for muscles [55, 20]. The amplitude of S-MMGs was shown to be highly correlated with the maximum of the second derivative of the force output during the onset of muscle contraction. At the cellular level, the second derivative of the force output is related to the amount of calcium ions released by the muscle cells [54]. Therefore, the second derivative of the force output is considered to be a good indicator of the muscle activation level. Hence, S-MMGs depend on specific aspects of the electromechanical coupling efficiency in muscles. The natural muscle vibrations recorded by S-MMGs can therefore be used to non-invasively estimate the muscle state and activity level in-vivo.

The physiological origin and time-frequency characteristics of S-MMGs depend on muscle structure and mechanical state, as well as the electromechanical coupling efficiency in muscles [6, 58, 69]. Indeed, the S-MMGs result from the non-linear summation of the active muscle fiber contractions [56, 79]. S-MMGs are also modulated by the architecture of the muscle-tendon complex and the fat and skin layers.

Typically, for isometric contractions at increasing effort level, the spectrum of the S-MMG signal exhibits an increase of its temporal root-mean square value along with a spectral shift towards higher frequencies [10]. These S-MMG variations are associated with a recruitment of faster motor units and an increase in firing rates of motor units [53]. Hence, S-MMGs have typically been used to monitor the muscle's mechanical activity (since the mechanical activity influences the S-MMG amplitude and frequency content), thus providing complementary information to electromyograms (EMGs) which measure the muscle's electrical activity instead. But S-MMGs have rarely been used to estimate the mechanical properties (e.g. viscoelasticity) of skeletal muscles [45, 59]. However, since the S-MMGs correspond physically to propagating vibrations along the muscle, they appear as a potential tool for non-invasive study of skeletal muscle viscoelastic properties [63].

Despite the large body of literature on S-MMGs, the spatial variations of S-MMG over a single muscle remain unclear because most studies have used only a single sensor, and the influence of the sensor location over the muscle of interest was investigated in only a few recent studies [15, 18, 46, 59]. Those studies, using a two-dimensional array of accelerometers [18, 27, 45], have shown that the S-MMG amplitude and frequency content is indeed strongly influenced by the S-MMG sensor location over the studied muscles. The propagation directionality (e.g. transverse vs. longitudinal) and spatial origin (e.g. from motor points or from muscle extremities) of the S-MMG over the muscle is likely to vary depending on the type of tested muscle contractions (e.g. sustained voluntary contractions vs. direct electrical stimulation of motor twitch), and on the frequency band which is analyzed. Hence, the physiological origin of S-MMG generation mechanism (e.g. force tremor vs. muscle fiber contractions) should be frequency-dependent [54]. When analyzing S-MMG of skeletal muscle, the frequency band selected could dramatically affect the results and give false information, depending on what exactly is being studied. For example, if the

goal of a study is to analyze the muscle fiber activity, a frequency band of 5 - 20 Hz would not be selected, as that band is mostly dominated by whole limb motion and muscle tremor, not muscle fiber activity. Existing studies only partially address these issues, in particular the frequency-dependency of the S-MMG spatial variations and S-MMG propagation directionality in the muscle [18, 17, 27, 59].

1.1.3 Current Elastography Techniques

Figure 4: Manual muscle palpation (adapted from [50]).

Palpation is used as part of a physical examination by medical doctors or physical therapist to assess the texture of a patients tissue. Traditional palpation techniques, such as the modified Ashworth scale, rely on the clinician or physician to perform a manual palpation as seen in Figure 4. This can only provide a subjective (qualitative) assessment of muscle stiffness (or muscle tone) since the diagnosis often depends on the experience and subjectivity of each examiner [47]. On the other hand, elastography techniques have been developed to provide objective measurements (quantitative) of the viscoelastic properties of skeletal muscles by mapping how these properties influence the physical characteristics (e.g., amplitude or velocity) of low-frequency mechanical vibrations [34] propagating along the tested muscles. These techniques

can be broken into two parts, first the shear wave excitation techniques (see Figure 5) and then the shear speed measurement techniques (see Figure 5).

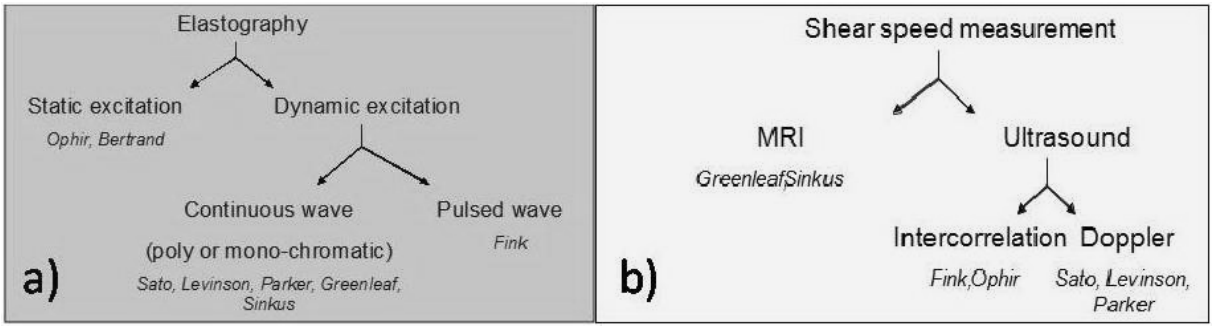

Figure 5: Current elastography techniques displaying methods (a) to excite shear waves in the muscle and (b) to measure the speed at which those waves travel through the muscle. The names of the researchers who developed these methods are indicated.

Currently, all standard elastography techniques are active since they rely on an external mechanical or radiation excitation source to generate these propagating vibrations into skeletal muscles [34]. They use either static excitation or dynamic excitation to generate shear waves in the muscle. Different methods have been developed to measure the speed at which the shear waves travel, with two such methods to be discussed here.

Magnetic resonance elastography (MRE) is one such technique that uses magnetic resonance imaging (MRI) in conjunction with the application of mechanical shear waves to determine muscle properties. The machine is large, immobile and incapable of certain exercises while taking measurements (see Figure 6(a)). This process has three basic steps: 1) inducing shear waves in the muscle (active), 2) imaging the propagating waves with MRI (expensive), and 3) analyzing the data to generate images with stiffness [43]. MRE uses low frequency (10 Hz to 1.1 kHz), harmonic, transverse acoustic waves as the source of the external mechanical stress applied to the medium. As the acoustic waves propagate through the medium, they cause small cyclic displacements that are typically on the order of tenths of microns. The

displacement map gives a snapshot of the wave propagating through the muscle, and by measuring the wavelength (see Figure 6(b)), the stiffness of the medium can be determined [51]. The MRE method is ideal for imaging tissues that can not be sensed at the surface (such as the brain).

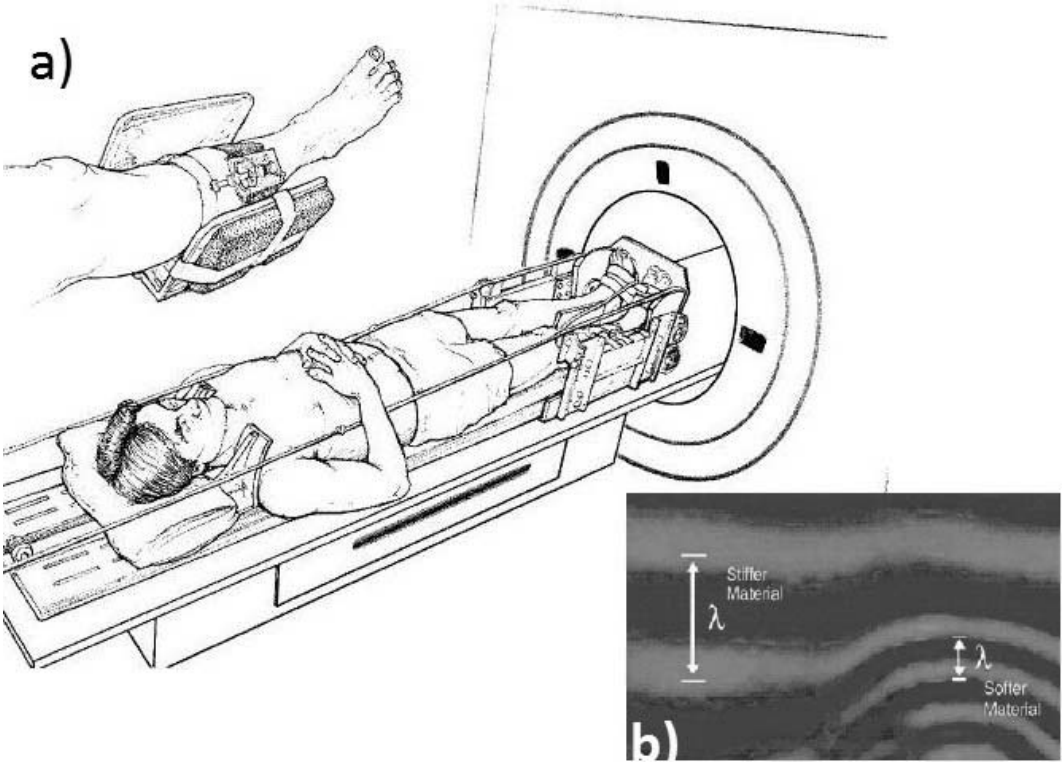

Figure 6: (a) MRE experimental setup for subject before being placed in the MRI bore and (b) resulting image of MRE with the colors red and blue being the peak and trough of the wave (from peak to peak shows one wavelength). It can be seen that there is a longer wavelength (stiffer material) and shorter wavelength (softer material). (adapted from [7])

However, if measuring skeletal muscles, there are more inexpensive and simpler methods that can provide comparable results. Another current elastography technique that has developed recently is ultrafast ultrasound elastography imaging (see Fig. 7). This method, instead of using a shaker at the surface like previous elastography technique, uses an ultrasound probe to create a radiation push in the muscle.

After the radiation push is created, this method uses the ultrafast echnographic imaging approach of transient elastography. A major benefit is that it uses the ultrasound probe to create the acoustic radiation force and uses the same probe to measure the shear wave speed in real time. This technique has been recently used to show its feasibility in measuring the stiffness of skeletal muscle during resting and contracting muscles [71]. This device has some benefits over the MRE, as it is portable, does not require a separate excitation and measurement device and takes seconds instead of minutes of visualization time. Some limitations of this technique are that it is active, expensive, and can only measure the stiffness of a small portion of the tissue at a time and not the whole limb (see Figure 7(b)). Consequently, implementing a near-real-time tomographic elastography system (i.e. similar to a CT scan) for imaging the spatial variation of the local viscoelastic properties along a whole muscle can potentially be challenging with active elastography techniques since multiple excitations would be needed at various locations over the muscle of interest. This could be achieved using several excitation sources simultaneously or alternatively moving a single source along the muscle and assuming that the muscle condition is not changing between measurements. Overall, such an experimental set-up would likely increase the complexity, duration and thus costs of future clinical protocols as well as potentially create discomfort for the patients.

1.2 Thesis Motivation

Mechanical properties of skeletal muscles (e.g. viscoelasticity) are essential parameters used to predict muscle functional properties and to assess the evolution of, and recovery from, musculo-skeletal and neuromuscular disorders (MND), as the muscle stiffness often differs between a healthy and a diseased muscle. Physicians and clinicians sometimes use manual palpation at the muscle surface to monitor the muscle

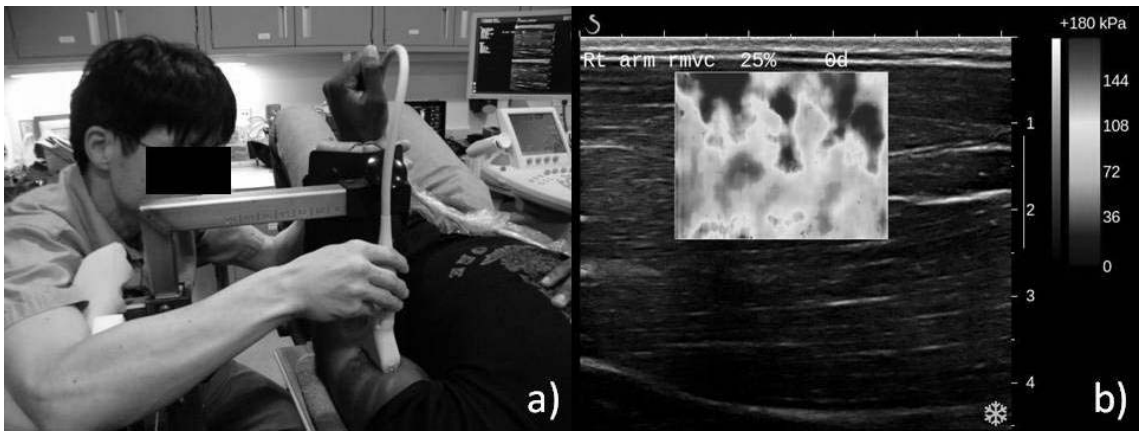

Figure 7: (a) Experimental setup for ultrafast ultrasound measurement and (b) resulting image of ultrafast ultrasound, with the color bar showing the different stiffness.

state but manual palpation can only provide a subjective assessment of muscle viscoelasticity. Little is known about how muscle viscoelastic properties vary quantitatively during contraction (even for healthy individuals) or during physical rehabilitation treatments for patients with MNDs, mainly because noninvasive and quantifiable techniques are not widely used.

Noninvasive viscoelasticity imaging, or dynamic elastography, methods have recently been developed to objectively quantify the local viscoelastic properties of soft tissues by measuring the local propagation velocity of mechanical shear vibrations (e.g. faster velocity indicates stiffer material). But the existing elastography technologies require a potentially uncomfortable external mechanical stimulation (e.g. vibrating probe) to induce muscle vibrations and sophisticated and expensive imaging equipments (such as MRI and ultrafast ultrasound elastography), involving complex signal processing, to record and analyze these muscle vibrations.

It has been demonstrated that coherent vibrations between sensor pairs, extracted from diffuse random wave fields or ambient noise measurements, can be used to estimate passively the local impulse response (or Green's function) of the propagating

medium between these sensors. The recent investigations in ultrasonics [77], seismology [64, 66], underwater acoustics [64] and structural health monitoring [41, 63] demonstrate this theory. Based on this approach, there is potential to develop a passive elastography technique which relies on extracting the fraction of coherent vibrations propagating between a pair of skin-mounted sensors, in order to directly measure the local properties of the contracted skeletal muscle [63]. When using an array of skin-mounted sensors, this passive elastography technique would allow for simultaneous elastography measurements between multiple sensor pairs since each S-MMG sensor potentially acts as a virtual in-vivo vibration source radiating along the muscle.

The overall objective of this work is to characterize the surface mechanomyogram measured on the biceps brachii muscle in order to develop a technique to analyze the coherence between sensors that can track the changes in the muscle during isometric voluntary contractions. The frequency, origin, directionality and sensitivity of the natural muscle vibrations is investigated using skin-mounted accelerometer arrays in order to determine their suitability for passive elastography. This project also advances the fundamental knowledge of mechanical properties and mechanical activity of skeletal muscles with respect to neurological stimulations, by providing information on muscle fiber contractile properties during isometric contractions. As a step towards developing a low cost, passive, non-invasive elastography method, this thesis shows that the coherence length of S-MMG along the biceps brachii is strongly correlated with the isometric contraction level.

1.3 Research Aims

Aim 1: Investigate 3-dimensional components of Surface Mechanomyogram

Approach: Determine which of the 3-dimensional components of vibration would best be used to measure the propagating S-MMG waves during isometric voluntary

contractions. This is done by analyzing the mean power frequency, cut-off frequency, power spectral density and the azimuthal and elevation angles of power from a line array of 3-dimensional accelerometers placed on the longitudinal axis (proximal to distal) on the skin above the biceps brachii.

Hypothesis: The component of the 3D vibrations of the biceps brachii that has the most power in the frequency range of interest is the axis orthogonal (z-component) to the skin's surface. This is due to the dimensional changes of the muscle fibers in the axes perpendicular to the long axis of the muscle fiber and the amplification of the power due to a rigid boundary below the muscle.

Aim 2: Directionality analysis of S-MMG propagation

Approach: Using the results from Aim 1, the component with the most vibration power in the frequency range of interest is measured in order to determine the propagation direction and frequency band of interest that best represents the propagating portion of the S-MMGs. This is done by analyzing the spatial coherence and cross correlation of sensors arranged in a 3×5, 2-dimensional grid on the skin surface of the biceps brachii muscle.

Hypothesis: The longitudinal direction (proximal to distal) and the frequency band of approximately 30 Hz $\pm$ 2 Hz are the direction and frequency band that is the best representative of the propagating portion of the S-MMG waves.

Aim 3: Using spatial coherence of the S-MMG along the biceps axis to track the muscle's contraction level

Approach: The results from Aim 1 and 2 give the details on how to measure the propagating S-MMG waves associated with muscle fiber activity. Aim 3 is focused on parameterization of the spatial coherence to extract a repeatable and reliable parameter that can track muscle contraction level of S-MMG.

Hypothesis: The coherence length of S-MMG can be used as a marker of the muscle's contraction level.

Aim 1 the 3-dimensional analysis, and Aim 2 the directional analysis, together focus on classifying the S-MMG vibrations measured by the accelerometers. These first two aims are independent of each other and the data was collected from two different experiments. The first two aims help determine which vibration axis to measure and in what direction to orient a line array of sensors to measure the propagating waves. Aim 3 builds on the knowledge learned from the first two aims and it develops the passive elastography approach, with the determination of a quantifiable parameter (S-MMG coherence length) that tracks the changes in the muscle. Aims 1 and 2 also lead to a greater physiological understanding of the biceps brachii muscle during isometric voluntary contractions by providing new information on the muscle-tendon complex. Aim 3 is the culmination of this doctoral work, which is applying wave propagation principles to the body to develop a metric that can track the changes in muscle conditions as the contraction level changes. This result sets the foundation for the development of a low cost, in-vivo, passive elastography technique.

1.4 Dissertation Organization

Chapter 2 focusing on Aim 1, shows the study that uses a line array of 3-dimensional accelerometers that investigate the three components of the acceleration at the skin's surface. This study also investigates which components of the vibration have more spatial variation, depending on the location of the sensor. Chapter 3 focuses on Aim 2, as it discusses the study that obtained results to determine the directionality of propagating S-MMG waves using a 3×5 grid of 1-dimensional accelerometers. This study was important to understand which direction should be focused on in order to

obtain the best data that represents the physiological phenomena of muscle contractions. Chapter 4 focuses on Aim 3 and uses the results from the previous two chapters to develop a model to determine a quantifiable characteristic that tracks the change in muscle properties during an isometric voluntary contraction. Chapter 5 summarizes and concludes the dissertation, as well as gives recommendations for future work. The appendix follows Chapter 5, which includes any code used, intermediary studies and less significant findings.

CHAPTER II

THREE-DIMENSIONAL ANALYSIS OF S-MMGS

2.1 Introduction

The measurement of muscle noise from naturally occurring vibrations during voluntary contractions is termed surface mechanomyogram (S-MMG). These vibrations are caused by dimensional changes in the muscle fiber and muscle-tendon geometry [53, 10]. Typically, S-MMGs have been used to monitor the mechanical activity of a contracting muscle. S-MMGs have been used recently for numerous muscle related objectives, for example: 1) muscle fiber typing in sports medicine [57]; 2) to investigate the effect of neuromuscular diseases on the muscle [3]; and 3) to investigate the effect of aging on the muscle [26]. S-MMGs are suggested to be a good index for force and fatigue for muscles [55, 20]. When measuring S-MMG with accelerometers, most studies use one-dimensional sensors and focus on one component of measured vibration. The vibration also consists of two orthogonal components that are normally neglected. Despite the large body of literature on S-MMGs, there were few studies found in the literature that investigated more than one axis of vibration. In a study found, the authors used laser displacement sensors to examine the cross correlation of S-MMG from one location on the rectus femoris and found that there is a high level of association between the signals of the two axes measured [9]. This study concluded that there is a high correlation coefficient for the normal axis and an axis 45 degrees from the normal, and suggested that further work be done to investigate the sensor location effect on the multiple axis S-MMG amplitude and frequency content versus force.

Recent advancements in technology have allowed for development of 3-dimensional

accelerometers that have a mass of 5.4 grams, which is well below the 30 grams estimated level before mass loading artifacts affect the measurement of S-MMG [16, 76]. It is known that the muscle activity during voluntary contractions is dynamic and 3-dimensional, and there is limited knowledge to suggest that only one dimension of vibration provides significant physiological information. Using these 3-dimensional accelerometers allows for measurements unattainable by most other measurement techniques, mainly the relation between in-plane and out of plane vibration, which can provide physiological information on the muscle activity that is currently not investigated. The main aim of this chapter was to determine the dominant vibration direction and its frequency dependency of the biceps brachii muscle during submaximal isometric voluntary contractions using a 5 sensor line array of 3-dimensional accelerometers. It is hypothesized that due to bulk motion and muscle tremor in the low frequency (f <20 Hz) regime, the vibration power direction is more in-plane, but as the frequency increases and the vibration is the result of local muscle fiber activity (40 Hz> f >20 Hz), the vibration power direction is more vertical (out of plane).

2.2 Methods

2.2.1 Subjects

Fifteen male subjects (age: 27.2 ± 3.5 years, height: 179.9 ± 7.3 cm, weight: 77.1 ± 7.1 kg), with no previous history of skeletal muscles diseases participated in this study and signed an informed consent form. This study was conducted according to the protocol approved by the Institutional Review Board of the Georgia Institute of Technology.

2.2.2 Experimental Setup

Five three-dimensional accelerometers (356A32, mass = 5.4 g, base length 11.4 mm, measurement range = $\pm$ 491 m/s^2 pk (50 g pk), sensitivity = 100 mV/g; PCB Piezotronics, Depew, NY) with flexible cables (<2 mm diameter) were used to record

S-MMG along the center line of the biceps brachii muscle (Fig. 8). The accelerometers were skin mounted over the biceps brachii using double sided medical tape to provide good contact while minimizing mounting artifacts and allowing the muscle to move freely without additional pressure interference.

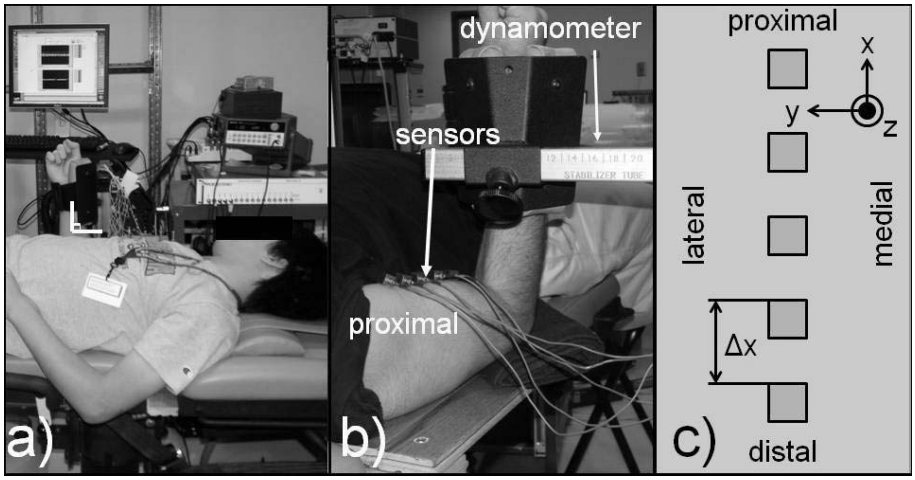

Figure 8: Experimental setup showing the (a) subject's physiological position (b) position of the arm along with sensors and (c) layout of sensors with coordinate system.

The accelerometers were arranged in a line array (Fig. 8(c)). The biceps brachii length was determined based on anatomical landmarks for each subject as extending from the origin of the tendon of insertion (distally) to the coracoid process of the scapula (proximally) [33]. This longitudinal axis corresponds to the muscle fiber orientation since the biceps muscle has a simple fusiform architecture [60]. The longitudinal spacing distance between the accelerometers (Δx) was determined as 8% of the estimated length of the biceps brachii long head muscle, following a previous approach [62, 60].

2.2.3 Experimental Protocol

The S-MMGs were recorded during 10 s long voluntary isometric contractions with elbow flexors. A dynamometer (HUMAC, CSMi Medical Solutions, Stoughton, MA)

was used as a platform for muscle contraction. Each subject was situated laying on his back with the right arm attached to the dynamometer at the wrist. The elbow was flexed at 90 degrees, and the wrist was oriented in the neutral position. The right upper arm was placed horizontally with its posterior part not touching the bed surface. The rotation axis of the elbow joint was visually aligned with the rotation axis of the dynamometer. The force output of the biceps was recorded independently by a force transducer attached to the horizontal bar connected to the subject's wrist by a velcro strap. The maximum voluntary contraction (MVC) force for each subject was determined based on the maximum force output measured over 3 maximal voluntary contractions. Thereafter, subjects performed sub-maximal isometric contractions, in which they were asked to produce and maintain 20%, 40%, and 60% of MVC force for 10 s while facing a video monitor displaying force output as visual feedback. Subjects were encouraged to rest and relax for 3 min between each contraction in order to minimize artifacts due to muscular fatigue. A total of three trials were performed, where one trial consisted of a randomized order of contractions levels (20%, 40%, and 60%).

All 16 channels (5 sensors $\times$ 3 axis + force transducer) for the recording of S-MMGs were time synchronized with a sampling frequency of 1 kHz (Compact DAQ system, National Instruments®, Austin, TX) and were amplified with a gain of 200. Data were filtered in the frequency band ($f_1 = 5$ Hz and $f_2 = 250$ Hz), using a second order Butterworth bandpass filter. The lower frequency bound f_1 was selected in order to remove the lowest frequency oscillations in order to reduce the eventual bias resulting from motion artifacts (*i.e.* due to large movements of the whole limb [11, 32]. The upper frequency bound f_2 was set to 250 Hz, the frequency at which no significant S-MMG signal was recorded above the noise floor. The mean power frequency (f_{MP}) of the recorded signal was defined as:

$$f_{MP} = \frac{\int_{f_1}^{f_2} f G_{mm}(f)}{\int_{f_1}^{f_2} G_{mm}(f)} \tag{1}$$

where $G_{mm}(f)$ is the power spectral of the signal $m(t)$ [40].

2.2.4 Theory

2.2.4.1 Angle of Vibration

Two angles, θ (azimuthal angle) and ϕ (elevation angle), for the S-MMG power were defined as corresponding to the angles in Figure 9 and given by Eqs. 2 & 3.

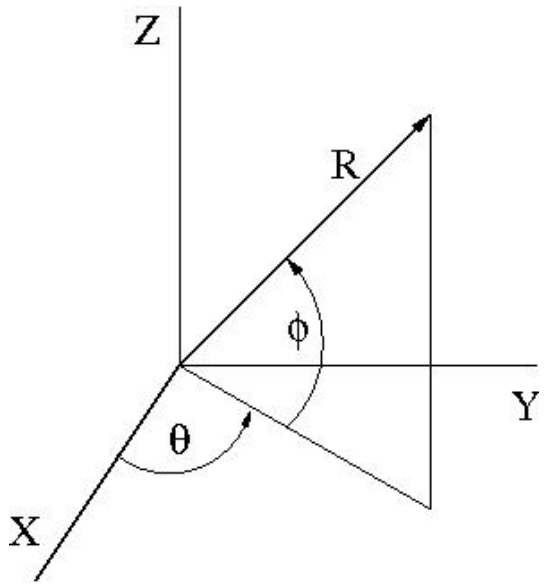

Figure 9: Coordinate system used for θ and ϕ calculation.

$$\theta(f) = atan\left(\frac{|Y(f)|}{|X(f)|}\right) \tag{2}$$

$$\phi(f) = atan\left(\frac{|Z(f)|}{\sqrt{X(f)^2 + Y(f)^2}}\right) \tag{3}$$

where $X(f)$, $Y(f)$ and $Z(f)$ correspond to the power spectral of $x(t)$, $y(t)$ and $z(t)$ respectively.

These angles correspond to the 3-dimensional representation in spherical coordinates of the total power. The angle θ represents the angle from the longitudinal direction to the lateral direction. The angle ϕ represents the angle from the horizontal plane to the vertical upward direction. The angles were calculated by breaking up the collected data segment into 17 segments of 550 points length (*i.e.* 550 ms), taking the absolute value of the fast Fourier transform (FFT) of the individual component axes X, Y and Z, and calculating the respective angles at a given frequency. The angles $\theta(f)$ and $\phi(f)$ were calculated using Equations 2 & 3, and then averaged over the 17 segments. This procedure resulted in a quantifiable way to analyze the angles of vibration power versus frequency. For example, when $\theta = 45°$, it corresponds to an equal amount of power on the X and Y axes (*i.e.* proximal and lateral directions (see Fig. **??**). When $\theta = 0°$ (resp. $\theta = 90°$) all of the in-plane power is along the X axis (resp. Y axis) (*i.e.* proximal direction (resp. lateral direction), see Fig. **??**). Note θ depends on the power of the X and Y components only (which are positive quantities), thus $0° \leq \theta \leq 90°$ in this study. For the angle ϕ (dependent on all three components), a value of 90° means that all the power is along the vertical Z axis, while a value of 0° means that there is no power along the vertical Z axis.

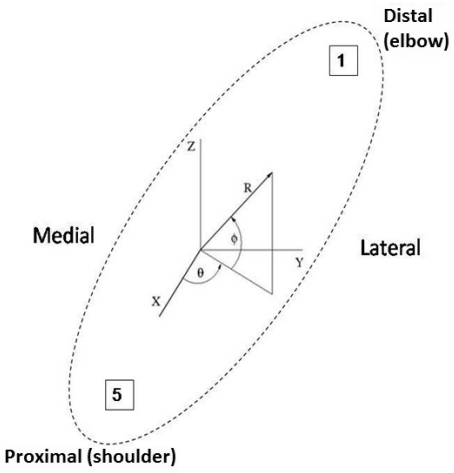

Figure 10: Three dimensional axes oriented on a schematic of the biceps brachii, indicating sensor placement and anatomical orientation.

Fig. 16 displays the evolution of the angles θ and ϕ for increasing frequency. The angles values were averaged across trials, subjects, contraction intensities, and sensors. With visual inspection, the maximum angles were in the 10-30 Hz and 30-60 Hz ranges for θ and ϕ, respectively. Using the angle-frequency relation in each sensor and subject, the maximum angles for $\theta(f)$ in the 10-30 Hz range and $\phi(f)$ in the 30-60 Hz range were determined in each trial. Additionally, the frequency at which the maximal angles appeared was also determined. These values were averaged across 3 trials at each contraction level. In addition to the frequency-dependent maximal angles, frequency-independent mean angles $\hat{\theta}$ and $\hat{\phi}$ were calculated by averaging the absolute value of the data in the time domain, and given by equations 4 and 5.

$$\hat{\theta} = atan\left(\frac{< |y(t)| >}{< |x(t)| >}\right) \tag{4}$$

$$\hat{\phi} = atan\left(\frac{< |z(t)| >}{\sqrt{< |x(t)| >^2 + < |y(t)| >^2}}\right) \tag{5}$$

2.2.5 Statistical Analysis

The major dependent variables investigated are power, $\hat{\theta}$ and $\hat{\phi}$ (frequency independent), maximal values of $\theta(f)$ and $\phi(f)$, frequencies at which maximal values of $\theta(f)$ and $\phi(f)$ appeared, and mean power frequency. The independent variables are contraction level (20%-60% MVC), sensor location (#1-#5), and directional component (X, Y, Z). To test the effect of contraction level and sensor location on $\hat{\theta}$ and $\hat{\phi}$ and maximal values of $\theta(f)$ and $\phi(f)$, a two factor (3×5) ANOVA with repeated measures was performed. To test the effect of contraction level, sensor location and directional component on the power and mean power frequency, a three factor ($3 \times 5 \times 3$) ANOVA with repeated measures was performed. Post hoc analysis was performed using Tukey for pair-wise comparisons when appropriate. An alpha-level of 0.05 was chosen for all statistical comparisons. $P < 0.05$ or $P < 0.01$ was additionally

noted where appropriate. All statistical analyses were performed using Statistica 9.0 software (StatSoft, Tulsa, OK). Unless stated otherwise, the data are presented as means ± standard deviation in the text and means ± standard error in the figures.

2.3 Results

Representative recordings of the filtered S-MMG for each axial component can be found in Figure 11 for (a) sensor #3 and (b) sensor #5.

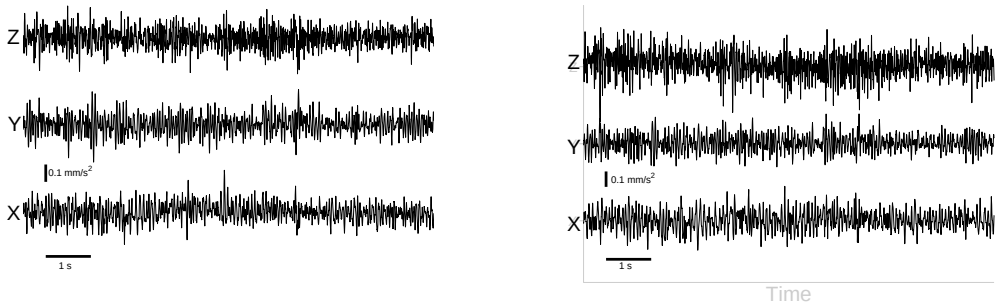

(a) (b)

Figure 11: Representative recording of S-MMG for each directional component at 60% MVC at (a) sensor #3 and (b) sensor #5.

To assure that there was no frequency dependency bias due to the accelerometers themselves, a true baseline was performed. This true baseline differs from the experimental baseline in that, it is independent of the experiment. Five 3 dimensional accelerometers were arranged in a line array with similar sensor separation distances, on a regular counter top and vibration absorbing table, attached with the same double sided tape that is used for the experiment (see Fig. 12).

The results from this preliminary experiment show that the angles ϕ (Fig. 13(a)) and θ (Fig. 13(b)) calculated from the true baseline data collected, show that there is no frequency dependency of angles when there is no human vibration. Therefore, any results from this experiment that show a frequency dependency, even at 0% MVC (experimental baseline) have a phsyiological meaning.

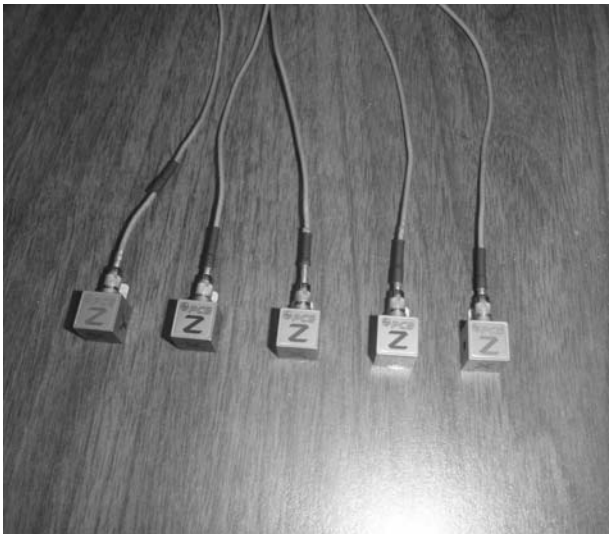

Figure 12: Three dimensional accelerometers on counter top for true baseline measurement.

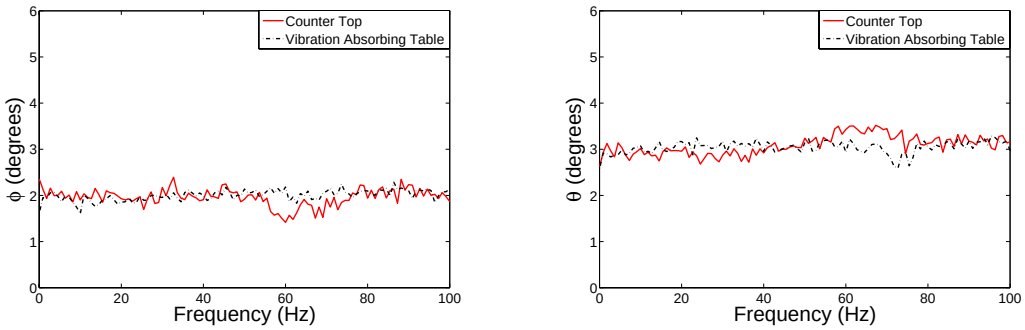

(a) (b)

Figure 13: True baseline measurement with 3-dimensional accelerometers angle (a) ϕ and (b) θ.

Power spectral density

To investigate the signal power in each component of the vibration and how that power changed with contraction level, the power spectral density was determined. The effect of contraction level and component axis on the power spectral density can be seen in Figure 14. The power spectral density was averaged across sensors, trials and subjects for the 3 different components (X, Y and Z). For a given frequency the

power spectral density of the signal increases as the contraction level increases. When comparing the power of the three different components with the contraction level being held constant, the power of the vertical (Z-axis) component is greater than the power in the in-plane (X and Y axis) components.

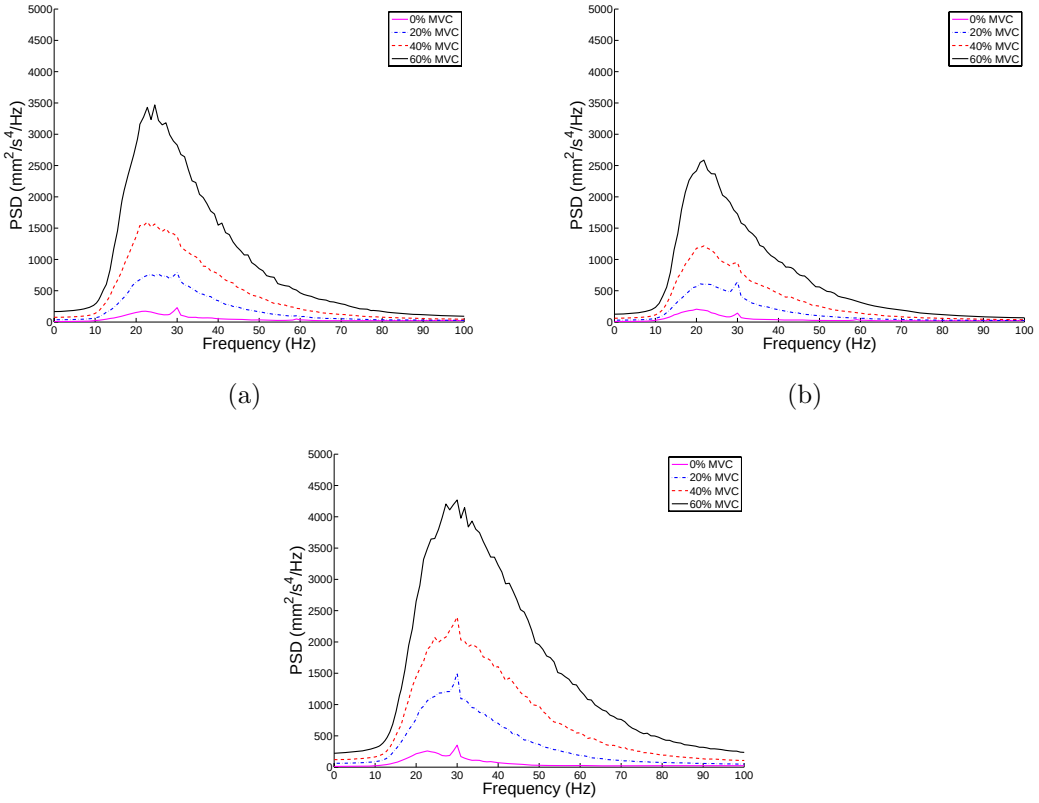

Figure 14: Power spectral density of S-MMG for increasing contraction level, averaged across sensors, trials and subjects for (a) X-component (b) Y-component and (c) Z-component.

Mean power frequency and Cut-off frequency

The power spectral density is a good indicator of total power, but in order to determine the frequency at which the average power is reached, the mean power frequency is investigated. The mean power frequency (see eq. 1) for each component (X, Y and

Z) was averaged across sensor location, trials and subjects to show the main effect of contraction level. Figure 15(a) shows the mean power frequency (see eq. 1) averaged across sensors, trials and subjects versus force contraction level. Figure 15(b) displays the cut-off frequency (frequency at which 90% of the power is below this level) averaged across sensors, trials and subjects versus force contraction level. The mean power frequency increases with increasing contraction level (P<0.05). The cut-off frequency has a statistically significant difference between components (P<0.01), there was no statistically siginificant difference with the main effect of contraction level. Investigating the mean power frequency it was found that there was a significant main effect of contraction level ($P < 0.01$). At 20% MVC, the mean power frequency in the Z direction (25.45 $\pm$ 3.88 Hz) was higher than the mean power frequency in the X (20.20 $\pm$ 2.59 Hz) and Y (20.85 $\pm$ 2.51 Hz) directions ($P < 0.01$). While at 40% MVC, the mean power frequency steadily increased when going from the X direction (20.40 $\pm$ 2.80 Hz) to the Y direction (21.31 $\pm$ 2.64 Hz) to the Z direction (27.86 $\pm$ 5.15 Hz) ($P < 0.01$). Considering the contraction level of 60% MVC, the mean power frequency again increased when going from the X direction (20.84 $\pm$ 3.16 Hz) to the Y direction (22.21 $\pm$ 3.51 Hz) to the Z direction (30.61 $\pm$ 6.46 Hz) ($P < 0.01$).

Effect of Frequency

The angles of vibration provide information on the direction of vibration. This direction of vibration is frequency dependent as θ and ϕ are shown versus frequency in Figure 16. The angles were averaged across subjects, sensor location and contraction levels (excluding the baseline @ 0% MVC) to show how these angles change with frequency. Figure 16(b) shows that the elevation angle of vibration ϕ increased from the low frequency region to the high frequency region (10 Hz> f >40 Hz). The angles of vibrations were averaged in 4.5 Hz frequency bands at increasing center frequencies

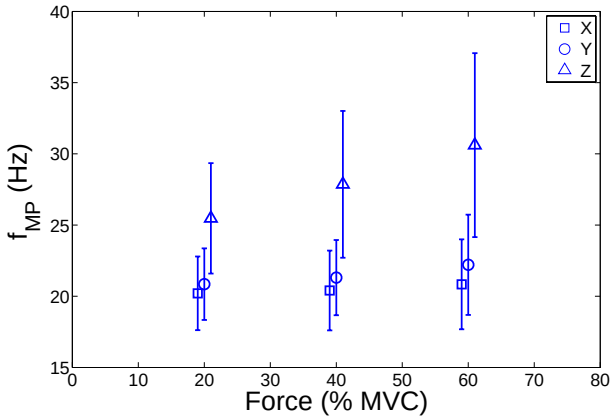

(a)

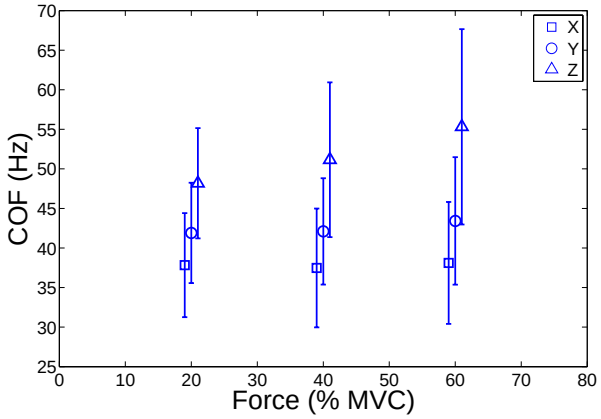

(b)

Figure 15: (a) Mean power frequency vs contraction level for all 3 dimensions (b) Cut-off frequency (frequency at which 90% of the power is below) vs. contraction level for all 3 dimensions. Error bars indicate one standard deviation of mean across subjects.

from 2.25 Hz to 93.2 Hz. The values can be seen as circles in the figures, with the error bars indicating one standard deviation of the data. For the angle $\phi(f)$ there is a statistically significant increase for increasing frequency between 10 Hz and 40 Hz ($P < 0.01$). These three center frequencies (10 Hz, 25 HZ and 40 Hz) were used to investigate the difference in the elevation angle (ϕ) and the azimuthal angle (θ) due to different physiological muscle activity at low ($f < 20$ Hz), mid ($f \approx 25$ Hz) and high ($f > 30$ Hz) frequencies.

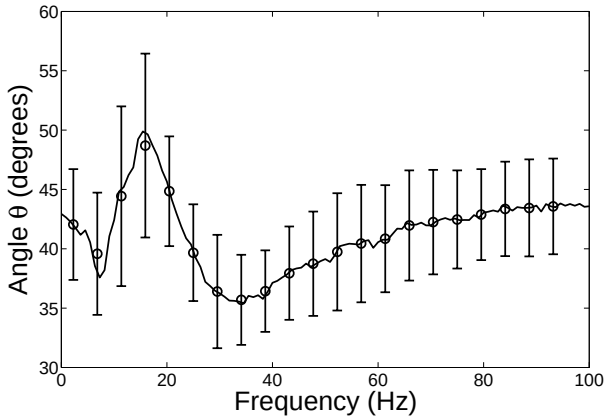

(a)

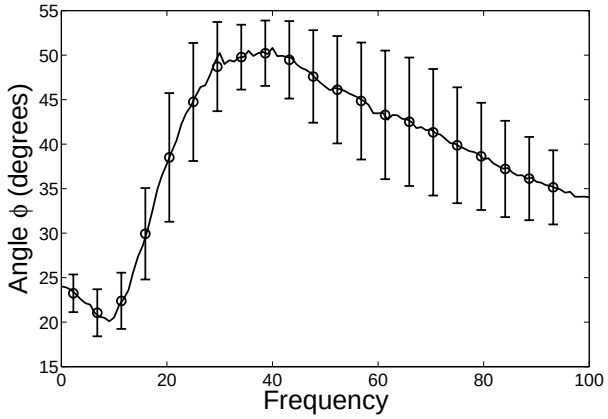

(b)

Figure 16: (a) Angle θ between longitudinal and transverse axes along with elevation angle ϕ between horizontal plane and vertical axis as a function of frequency with horizontal lines indicating the frequency bands low, mid and high. (b) Angles averaged in 4 Hz frequency bands versus frequency.

A 3-dimensional view of the power vectors can be seen in Figure 17 for different contraction levels (a) 20% MVC (b) 40% MVC and (c) 60% MVC. As the contraction level increased, the magnitude of the vectors increased as well. It can be seen that in a given contraction level, the power vector at 25 Hz is larger than the power vector at 10 Hz and 40 Hz. Also, within a given contraction level, as the frequency band increases from 10 Hz to 25 Hz to 40 Hz, the power vector becomes more vertical, having a higher value on the z-axis.

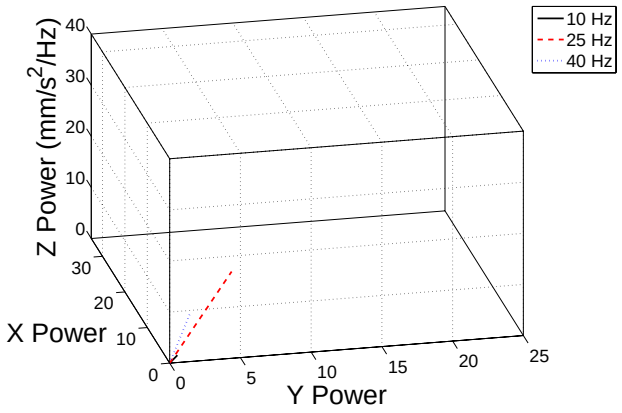

(a)

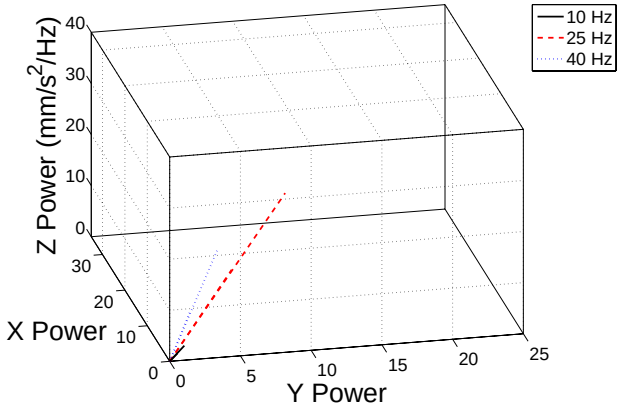

(b)

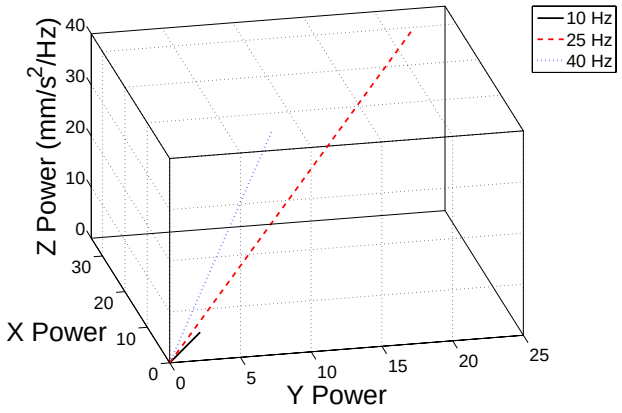

(c)

Figure 17: A three dimensional view of the power vectors for the three 4 Hz frequency bands centered at 10 Hz, 25 Hz and 40 Hz for (a) 20% MVC, (b) 40% MVC and (c) 60% MVC.

2.3.1 Directional Power

There was a significant main effect of contraction level ($P < 0.01$), a significant interaction of contraction level and directional component ($P < 0.05$), and a significant interaction of directional component and sensor location ($P < 0.01$) on the power. As a main effect of contraction level, the power in each direction increased with increased contraction level ($P < 0.01$, Fig. 18(a)). As the interaction of contraction level and directional component, at 40% MVC the power in the Z direction (11,958 $\pm$ 593.6 $mm^2/s^4/Hz$) was higher than the power in Y direction (9,167 $\pm$ 364.6 $mm^2/s^4/Hz$, P < 0.01), while at 60% MVC the power in both the X (22,917 $\pm$ 1423.5 $mm^2/s^4/Hz$, P < 0.01) and Z (22,893 $\pm$ 1254. $mm^2/s^4/Hz$, P < 0.01) directions were higher than the power in the Y (18,519 $\pm$ 1014.7 $mm^2/s^4/Hz$) direction. The increase from 20% MVC to 60% MVC in the Y direction (34.4 $\pm$ 23.5 $mm^2/s^4/Hz$) was significantly lower compared with that in X (43.1 $\pm$ 31.6 $mm^2/s^4/Hz/\%MVC$, P < 0.05) and Z directions (41.6 $\pm$ 28.2 $mm^2/s^4/Hz/\%MVC$, P < 0.05). The increase from 20% MVC to 40% MVC was less than the one from 40% MVC to 60% MVC in all directions ($P < 0.01$). The relative increase from 40% MVC to 60% MVC was greater in X direction (62.1 $\pm$ 48.9 5 $mm^2/s^4/Hz$) compared with the Y direction (46.8 $\pm$ 38.95 $mm^2/s^4/Hz/\%MVC$, P < 0.01). The significant interaction of directional component and sensor location indicated that the power in each directional component was differentially influenced by sensor location (Fig. 18(b)). On average, the X-component power in the most distal sensor (sensor #1) was the lowest among sensor locations, and it was significantly lower compared with a couple of other sensors (vs. #2, P < 0.01; vs. #4, P < 0.01). The Y-component power in the most distal sensor (sensor #1) was highest, on average, and was significantly higher compared with the most proximal sensor (sensor #5) ($P < 0.05$). The Z-component power in the most distal sensor (sensor #1) was lowest, on average, and was significantly lower compared with the middle sensor (sensor #3) ($P < 0.01$).

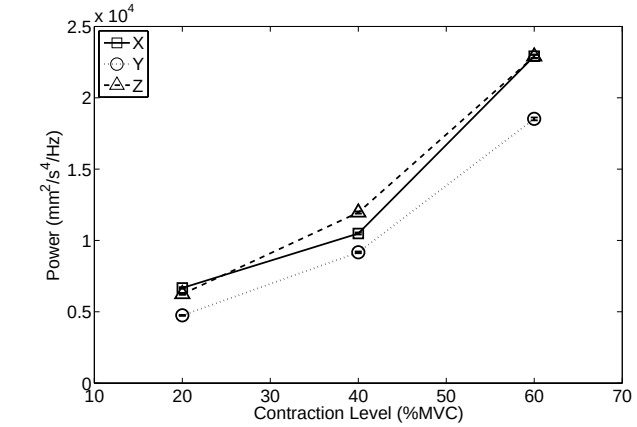

(a)

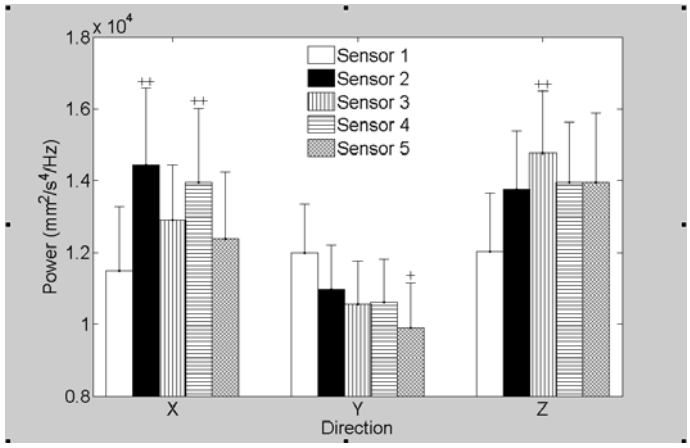

(b)

Figure 18: (a) S-MMG power of each directional component as a function of contraction level. Data is averaged across sensor locations. (b) S-MMG power of each sensor as a function of directional component. Data is averaged across contraction levels. , $P < 0.05$; , $P < 0.01$ vs. sensor #1.

2.3.2 Maximum and Mean Values

This section investigates the maximum value of the angle θ and ϕ in the frequency domain, as well as the mean angle by averaging in the time domain.

Effect on θ

Calculated in the time domain, $\hat{\theta}$ (see Eq. 4), was ≈40 deg across contraction levels (Fig. 19(a)). There was no significant difference in the $\hat{\theta}$ with respect to

changes in contraction level. The sensor location significantly influenced $\hat{\theta}$ ($P < 0.01$, Fig. 19(b)). $\hat{\theta}$ at the most distal sensor (sensor #1) was significantly greater compared with all other sensors by $\approx 5°$($P < 0.01$ for all comparisons).

In contrast to the consistent $\hat{\theta}$, the maximal value of $\theta(f)$ decreased significantly ($P < 0.05$) with increases in the contraction level (Fig. 19(a)). The maximal value of $\theta(f)$ was ≈60 deg at 20% MVC and was decreased by ≈2 deg at 40% MVC ($P < 0.05$) and 60% MVC ($P < 0.01$). The effect of sensor location on the maximal value of $\theta(f)$ was similar to the one in $\hat{\theta}$ (Fig. 19(b)). Due to the significant main effect of sensor location ($P < 0.01$), the maximal value of $\theta(f)$ at the most distal sensor (sensor #1) was significantly greater compared with all other sensors by ≈10 deg ($P < 0.01$ for all comparisons). The frequency at which maximal value of $\theta(f)$ appeared was not significantly influenced by contraction level or sensor location. It was 17.6 ± 3.5 Hz when averaged over all contraction levels and sensor locations.

Effects on ϕ

$\hat{\phi}$ was significantly influenced by both contraction level ($P < 0.05$, Fig. 20(a)) and sensor location ($P < 0.05$, Fig. 20(b)). The $\hat{\phi}$ was ≈30 deg at 20% MVC, and it decreased with increased contraction level. As a result, the $\hat{\phi}$ at 60% MVC was significantly smaller by ≈2 deg compared with 20% MVC ($P < 0.05$). For the effect of sensor location, the $\hat{\phi}$ at the most distal sensor (sensor #1) was the lowest among the sensors. The significant difference was found compared with the middle sensor (sensor #3, P < 0.05) and the most proximal sensor (sensor #5, P < 0.01).

The maximal value of $\phi(f)$ was significantly influenced by contraction level ($P < 0.05$, Fig. 20(a)), but not sensor location (Fig. 20(b)). The maximal value of $\phi(f)$ was ≈57 deg at 20% MVC, and it decreased with increased contraction level. The decrease from 20% MVC reached significance at 60% MVC ($P < 0.05$).

Frequency at which maximum angle is found

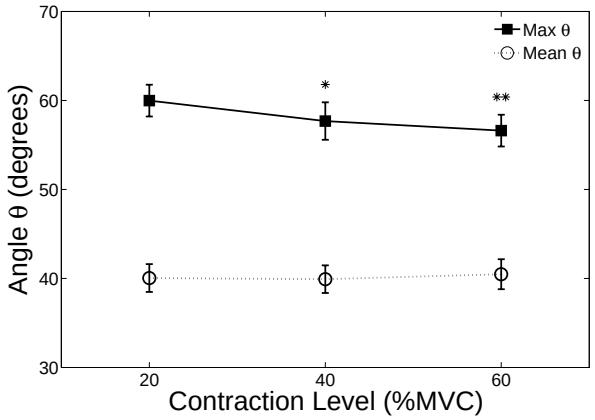

(a)

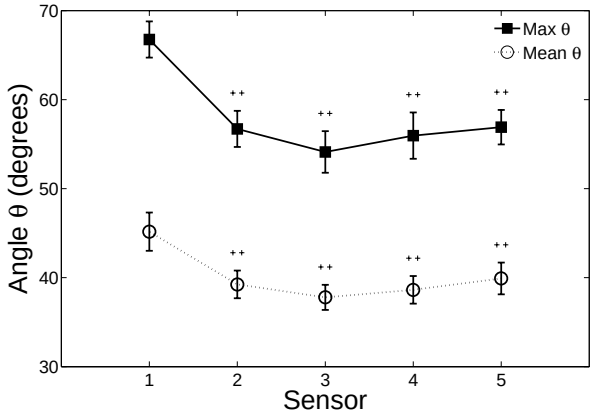

(b)

Figure 19: (a) $\hat{\theta}$ (see Eq. 4) and the maximal value of $\theta(f)$ (see Eq. 2) in the frequency domain as a function of contraction level (b) and sensor location. *, P $<$ 0.05 vs. 20% MVC; **, P $<$ 0.01 vs. 20% MVC; , P $<$ 0.01 vs. sensor #1.

In contrast to the case in maximal value of $\theta(f)$, the frequency at which the maximal value of $\phi(f)$ appeared was significantly influenced by both contraction level ($P < 0.05$, Fig 21(a)) and sensor location ($P < 0.05$, Fig. 21(b)). On average, the frequency for the maximal value of $\phi(f)$ ($\approx$40 Hz) was lowest at 20% MVC. It increased with contraction level, reaching a significantly higher value ($\approx$43 Hz) at 60% MVC compared with 20% MVC ($P < 0.05$). For the effect of sensor location, the frequency for the maximal value of $\phi(f)$ was lowest, on average, in the most

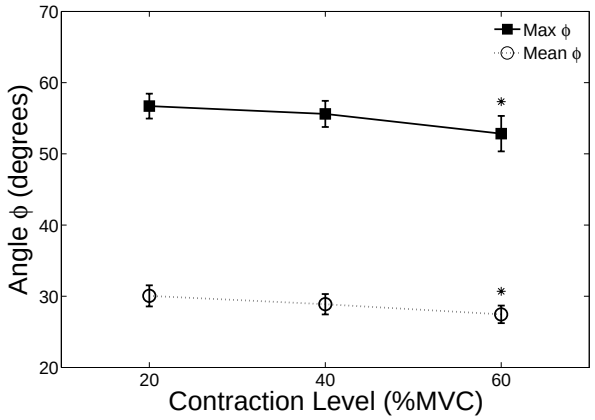

(a)

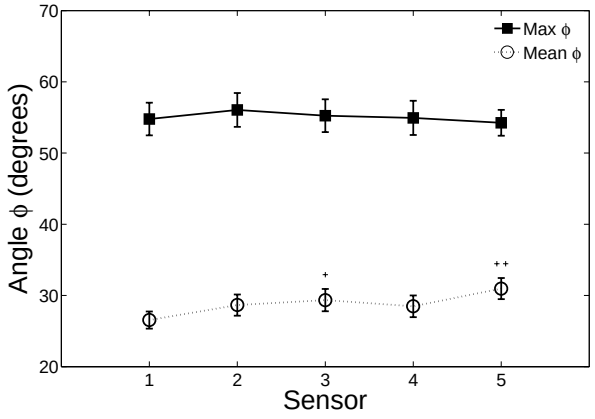

(b)

Figure 20: (a) The $\hat{\phi}$ in the time domain and maximal value of $\phi(f)$ in the frequency domain as a function of contraction level (b) and sensor location. *, P $<$ 0.05 vs. 20% MVC; , P $<$ 0.05 vs. sensor #1; , P $<$ 0.01 vs. sensor #1.

distal sensor (sensor #1), while it was similar in all other sensors. The values at the middle (sensor #3, P $<$ 0.05) and most proximal (sensor #5, P $<$ 0.05) sensors were significantly higher compared with the most distal sensor (sensor #1).

2.3.3 Selected Frequency Band (10 Hz, 25 Hz and 40 Hz)

This section investigates how the angles θ and ϕ in selected frequency bands change with respect to contraction level and sensor location. The 4 Hz frequency bands centered at 10 Hz, 25 Hz and 40 Hz were chosen in order to represent the frequency

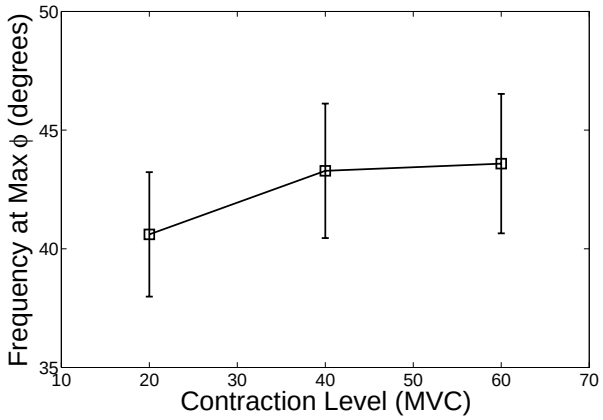

(a)

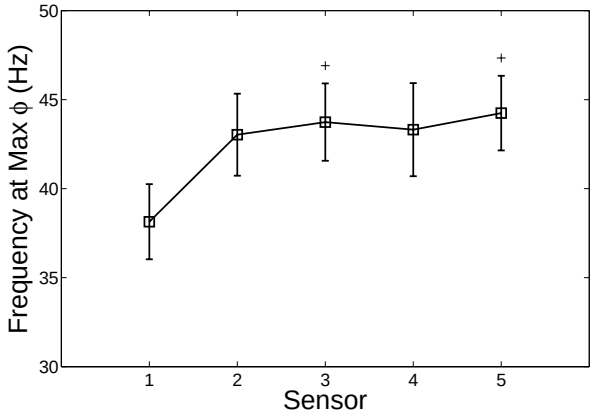

(b)

Figure 21: The frequency at which the maximum ϕ was found for (a) contraction level as the main effect and (b) sensor location as the main effect. *, $P < 0.05$ vs. 20% MVC; , $P < 0.05$ vs. sensor #1.

ranges that are dominated by different muscular phenomena. At low frequencies ≈10 Hz, the muscle activity is dominated by whole limb motion and muscle tremor, while at high frequencies, ≈40 Hz the muscle activity is dominated my local muscle fiber activation during contractions.

Effect of Contraction Level

The angles of vibration have shown to be influenced by frequency, and it was also

shown that the mean power frequency of the Z component increased as the contraction level increased. Now the effect of contraction level on the angles of vibration is investigated. Figure 22 shows the angles of vibration ϕ, the elevation angle Figure 22(a) and θ, the azimuthal angle Figure 22(b) with contraction level as the main effect. The angles were averaged across trials, subjects and sensor location. For a given contraction level (excluding 0% MVC) the elevation angle ϕ increased with increasing frequency (P <0.01). Also, at high frequency (40 Hz) the elevation angle ϕ increased as the contraction level increases (P <0.01). The contraction level had no statistically significant effect on the azimuthal angle θ.

Effect of Sensor Location

The sensors were placed along the longitudinal axis of the biceps brachii, with sensor #1 being most proximal and sensor #5 being most distal (see Fig. 1(b,c)). Along the longitudinal axis of the muscle, the effect of sensor location on the angles of vibration is investigated. The angles of vibration ϕ and θ were averaged across trials, contraction level (excluding 0% MVC) and subjects in the selected frequency bands to give sensor location as the main effect. The sensor location does not have an effect on the elevation angle ϕ or the azimuthal angle θ, as seen in Figure 23(a) and 23(b), as there is no statistically significant difference in the measured values.

Power at select frequency bands

The power was determined by calculating the area underneath the power spectral density curve for 4 Hz frequency bands. The three selected frequency bands for analysis were selected to represent different physiological phenomena, since different muscle activities dominate at select frequencies.

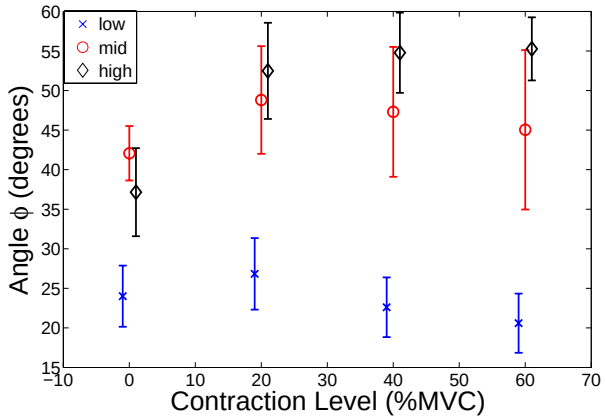

(a)

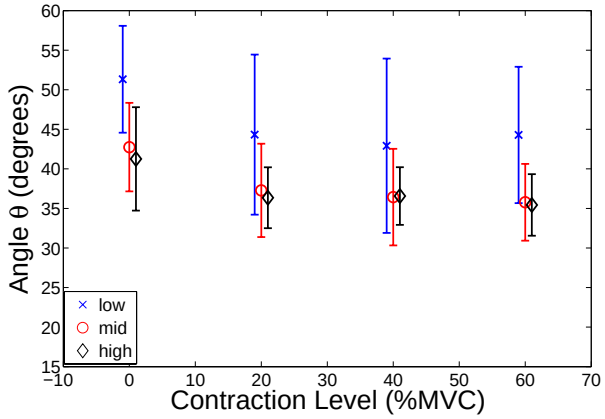

(b)

Figure 22: Vibration angles vs contraction level for low (10 Hz), mid (25 Hz) and high (40 Hz) frequency for (a) ϕ (elevation angle) and (b) θ (azimuthal angle).

For all of the power instances total, low, mid and high, there is a statistically significant difference with contraction level with the main effect ($P<0.01$). For the total power, there was a statistically significant difference between the components ($P<0.01$). It is hypothesized that the significant difference in the power due of the components is caused mostly by the muscle fiber activity at the higher frequency. Hence, at the low and mid frequency levels, there is not a statistically significant difference with the components as the main effect (see Fig. 24(a),24(b)). While at the high frequency range, there is a statistically significant difference between the components ($P<0.01$, see Fig. 24(c)).

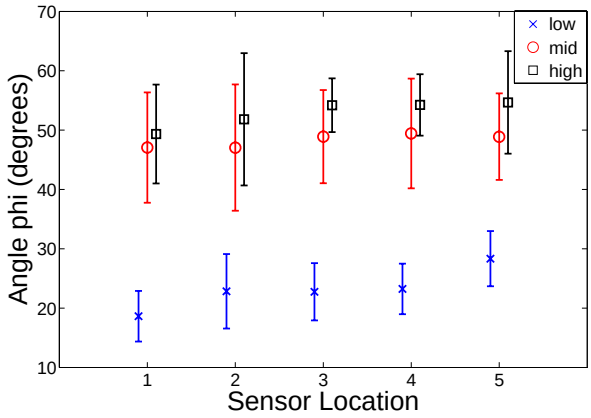

(a)

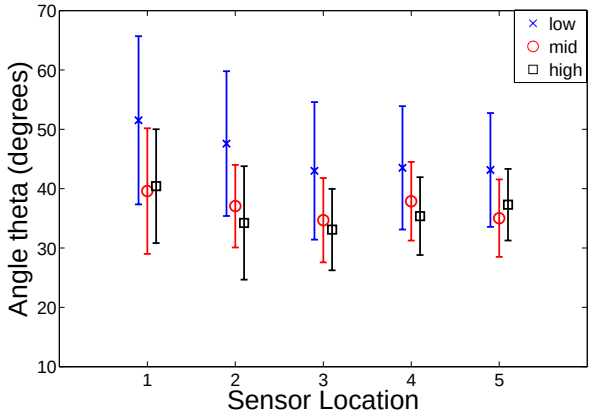

(b)

Figure 23: Vibration angle vs sensor location for low (10 Hz), mid (25 Hz) and high (40 Hz) frequency for (a) ϕ (elevation angle) and (b) θ (horizontal angle).

2.4 Discussion

The three dimensional angular orientation of the S-MMG power (as measured for angles θ and ϕ) was shown to vary with frequency, sensor location and contraction level. The power spectral density of the S-MMGs were analyzed to find that the intensity of the vertical component (Z-axis) of the signal increased as the contraction level increased, which is in agreement with previous studies [5, 39, 54]. Though these previous studies only focused on one axis (vertical Z-component), the present study

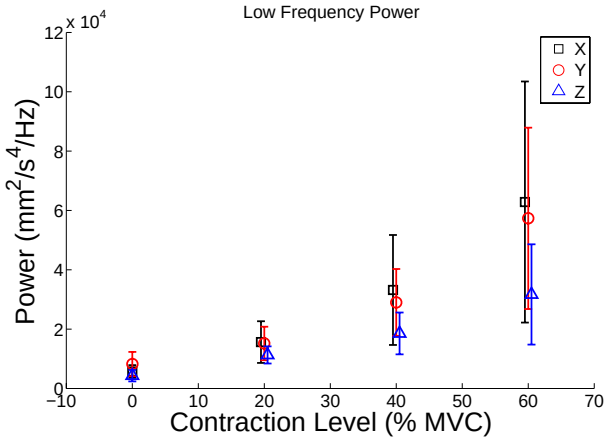

(a)

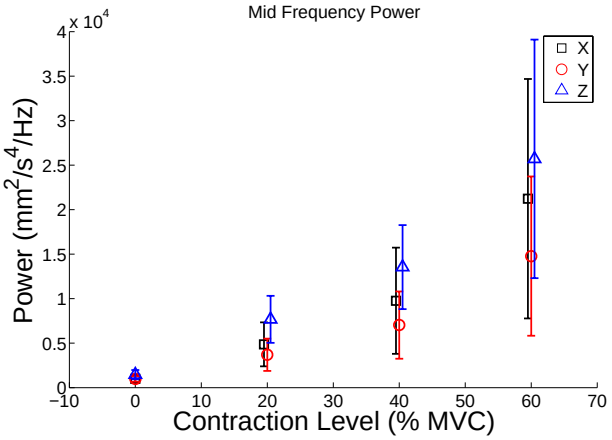

(b)

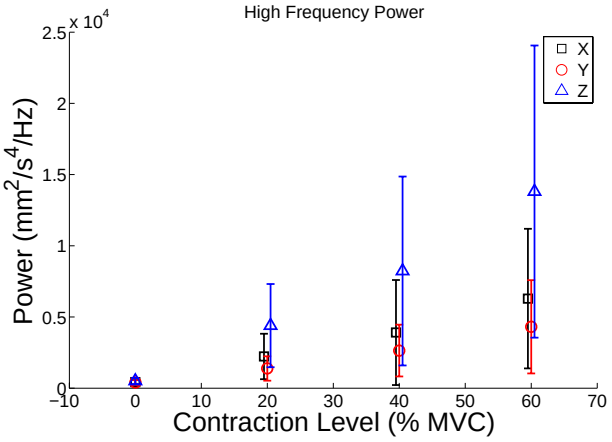

(c)

Figure 24: Power spectral density of S-MMG for increasing contraction level averaged across sensors, trials and subjects for (b) 10 ± 2 Hz (c) 25 ± 2 Hz (d) 40 ± 2 Hz.

found that similar trends were found in the other two components (X and Y axes) (see Fig. 14). The main finding of this study is that as the frequency increased from low to high, the mean of the power spectral density angle becomes more vertical, (meaning that the elevation angle increases). An additional finding was obtained in the current study. The S-MMG vibration power depends on the axis measured and the location on the muscle. Though the power increased for increased contraction level for all three components of vibration, the different components increased at different rates, which resulted in the azimuthal and elevation angles changing as the contraction level increased, because these angles depend on the ratio of the power. The changes in the vibration power result in specific changes in the mean and maximal angles that are reflected with a change in contraction level and sensor location.

The physiological origin of the S-MMG and the muscle-bone architecture can explain the main finding of the increase of ϕ as frequency increases. The azimuthal angle θ, measures the in-plane component of the vibration while the elevation angle ϕ, measures the out of plane vibration. Low frequency vibrations can be mostly attributed to synchronous muscle activity such as muscle tremor [11, 32] and whole limb motion, which can have the result of more in-plane motion of the muscle. The results show that at low frequencies, the elevation angle is not as prevalent as compared to high frequencies. Meaning there is a shift in vibration power direction from in-plane vibration to out of plane vibration as you move from low frequency ($\approx$10 Hz) to high frequency ($\approx$40 Hz) bands.

When considering the effect of contraction level on the azimuthal and elevation angles, it was shown to decrease the maximal value of $\theta(f)$, maximal value of $\phi(f)$ and $\hat{\theta}$, while having no effect on $\hat{\phi}$. Since θ depends only on the X and Y components (given by Eq. 2,4), the change in the power of the X and Y components can be compared to explain the change in maximal value of $\theta(f)$ and $\hat{\theta}$ for increased contraction level. As contraction level is increased, the vibration power of the X component increased

more than the Y component. The muscle fibers of the biceps brachii are aligned with the longitudinal axis of the muscle (X axis) for the middle and proximal portion. The contractile elements of the muscle fibers act along this axis and can be responsible for the greater power of the X component as the muscle becomes stiffer longitudinally during increased contraction due to cross bridging. The muscle also becomes shorter with increased contraction intensity [38] which could result in less vibration along the transverse Y component. Since ϕ depends on the vibration power of the X, Y and Z components (given by Eq. (3,4)), they can be compared to explain the decrease in ϕ as the contraction level increased. Both the X and Z components of the vibration power increases with contraction intensity more than the Y component does. Though, the vibration power of the X and Z component both increase at an approximately equivalent rate, the addition of the squares of the X and Y components caused the denominator of Equation 3 to increase more as the contraction level increased, which in turn caused the maximal value of $\phi(f)$ to decrease. Though both the Y and Z axis are along the radial direction, which would cause an equal expansion when the muscle fibers contract, the vibration power of the Z component may have increased more than the Y component probably due to the presence of a hard boundary (humerus bone) below (along the Z axis) the biceps brachii muscle, which may amplify the transverse vibrations along the Z axis.

Both the maximal value of $\theta(f)$ and $\hat{\theta}$ both had a significant difference between the sensor #1 and the other sensors. The sensor #1 was placed on the most distal sensor location, which is closest to the tendon as well as above the bicipital aponeurosis. The bicipital aponeurosis causes the distal portion of the long head of the biceps brachii to be angled more towards the transverse axis (Y axis) [33]. As the muscle contracts, there would be more power of the Y component at the most distal sensor due to this angling of the muscle fibers, which are more longitudinal more proximally along the biceps brachii. Also, as the biceps brachii muscle contracts there is a slight

rotational twist in the most distal portion of the muscle, which could explain why the maximal value of $\theta(f)$ and $\hat{\theta}$ were higher at the sensor #1. The $\hat{\phi}$ for the sensor #1 was significantly lower than the sensor #3 and #5. Between the most distal sensor (sensor #1) and the most proximal sensor (sensor #5), there is a significant decrease in the power in the Y direction, due to muscle fibers being more aligned longitudinally at the proximal end.

The mean power frequency of the Z component of the vibration power increased with increased contraction level, but the X and Y component saw no significant change with increased contraction level. For an increased contraction level, there is an increase in the discharge rate due to the recruitment of more fast-twitch muscle fibers. This change is observed more of the Z component of the vibration power may be due to the rigid boundary of the humerus bone that amplifies the transverse vibration along the Z axis. The frequency at which the maximal value of $\phi(f)$ was measured increased as the contraction level increased between 20% MVC and 60% MVC. Since the angle ϕ is directly proportional to the Z component (see Eq. 2), the significant increase of the mean power frequency of the Z component is reflected in the increase of the frequency at which the maximum ϕ is found with respect to contraction level. At the location of sensor #1, the frequency at which the maximal value of $\phi(f)$ was found is significantly lower than at location of sensor #3 and sensor #5. This change could be caused by the same factor that influenced the difference in the maximal value of $\theta(f)$ between those positions. The higher vibration power of the Y component at sensor #1, would cause a drop in the overall frequency at which the maximal value of $\phi(f)$ was found. In summary, the power measured on each axial component may be affected by the architecture of the musculo tendineous complex of the biceps birachii, as it changes with contraction intensity and location on the biceps brachii.

In summary, the 3-dimensional components of vibration have a dominant nature

which depends on the frequency, contraction level and sensor location. The scientific knowledge gained from the results of this study showed that when measuring a single axis of S-MMG, it is important to select the frequency band and sensor location which best represents the physiological muscle activity of interest. A 3-dimensional measurement of S-MMG can be useful if the interest is in synchronous low frequency muscle activity, which can be best represented by in-plane vibration (X and Y axes). Since for most studies, S-MMG measurements are analyzed for local muscle fiber activity, it is suggested that a uni-axial measurement technique can be used with the axis of measurement being out of plane (Z-axis).

2.5 Conclusions

This study focused on the 3-dimensional aspect of vibrations measured by accelerometers on the skin surface above the biceps brachii. It was found that the angles, ϕ and θ were frequency dependent, seeing that the vibration power became more vertical as the frequency increased to the region where muscle fiber activity dominates. Since the goal of this work is to measure the vibrations created by the muscle fiber activity, it is sufficient to measure only the z-component of the vibration. In addition, with increased contraction level the S-MMG total power becomes more in-plane (decreased ϕ). Also, it was noted that at the most distal sensor location, the S-MMG power is more lateral than the other sensor locations.

2.6 Summary

Naturally occurring vibrations of the skeletal muscle during voluntary contractions are not 1-dimensional, though most current research measuring S-MMGs are done using uni-axial sensors. These studies fail to consider the other components of the vibration. In this chapter, a research study that investigated the 3-dimensional components of acceleration is discussed. The experimental setup consisted of a line array of five 3-dimensional accelerometers attached to the skin above the biceps brachii to measure

the S-MMGs on the biceps brachii muscle during isometric voluntary contractions. A method of measuring the angles of the power of the vibration was developed and used to analyze the change of the angles versus frequency. The angles used to describe the power coincide with a spherical coordinate system that uses θ as the azimuthal angle , ϕ as the elevation angle, and r to describe a vector. It is hypothesized that when analyzing the power of each directional component of the acceleration, the power vector will become more vertical (as defined by an increase in the azimuthal angle ϕ) as the frequency increases from a band that represents muscle tremor and whole limb motion (f <20 Hz), to a frequency band that represents local muscle fiber activity (40 Hz> f >20 Hz). With these results, it was determined that in order to accurately measure the muscles vibration resulting from local muscle fiber contraction, solely uni-axial sensors that measure the vibration in the vertical (out of plane) direction can be used.

CHAPTER III

PROPAGATION DIRECTION OF S-MMGS OVER THE BICEPS BRACHII SURFACE

3.1 Introduction

In chapter 2, it was found that measuring the vibration of the muscle contractile elements in the vertical (z-axis) direction, can provide suffient vibration power in the frequency range of interest. In order to correctly measure the propagation of a wave, the sensors need to be arranged in a way that captures the wave as it is propagating. It is indeed important to determine the wave propagation direction for the correct frequency band (the frequency band that reflects muscle fiber activity). A previous study that have used a 2-dimensional grid, have included the low vibration frequencies that reflect whole limb motion and muscle tremor artifacts, which has the potential to bias the results [45]. In some instances, it may not be ideal to use a 3×5 grid of 15 sensors to measure the propagation of the S-MMG waves. To obtain a quicker setup time, or a lower cost it may be ideal just to use a line array of sensors. In these cases, it is essential to know which direction to setup the line array of sensors in order to best measure the propagation of the S-MMG wave. In preliminary studies using a single subject, high-frequency S-MMGs (*i.e.* filtered > 25 Hz) of the biceps brachii and vastus lateralis muscles mainly propagated longitudinally along the muscle fiber orientation during sustained voluntary contractions [63, 62]. Indeed these high-frequency S-MMGs were likely generated by asynchronous muscle fiber activity for these superficial muscles and were likely not significantly influenced by synchronized tremor activity that occurs at lower frequencies. No studies are found in the existing literature that systematically investigated directionality of the coupling

of the measured S-MMG between low and high frequency bands.

For a given pair of vibration sensors (here skin-mounted accelerometers), the spatial coherence of the S-MMGs is a measure of the similarity of the S-MMGs measured at those two sensors [29]. For instance, the spatial coherence of mechanical vibrations increases when these vibrations propagate along a more homogeneous (or uniform) medium such that the relative phase of the propagating vibration signals remains relatively undisturbed. The main aim of this study was to systematically determine the directionality in different frequency bands of the spatial coherence of the S-MMGs from the biceps brachii muscle during sub-maximal isometric voluntary contractions using a two-dimensional array of skin-mounted accelerometers (see Fig. 26). Preliminary studies that investigated the directionality of natural muscle vibrations in one subject did not study the influence of the selected frequency band of the S-MMG [63, 62]. The spatial variation of S-MMG coherence across all sensor pairs at low (f <25 Hz) and high (f >25 Hz) frequency bands can then be used to infer how the S-MMG coherence varies with directionality (*i.e.* longitudinal vs. transverse) and sensor separation distance for various contraction levels.

In this work, the longitudinal direction corresponds to the main orientation of the biceps brachii muscle's fibers and is expected to be more homogeneous than the transverse directions [28]. The high frequency mechanical oscillations (f >25 Hz) are less influenced by synchronous tremor-like activity [54]. Therefore, the high frequency oscillations are more likely to propagate coherently along the muscle fiber orientation (*i.e.* longitudinal direction) similarly to elastic guided waves propagating along cable (or fiber) bundles [61]. Consequently, it was hypothesized that the spatial coherence of high frequency S-MMG (f >25 Hz) is overall higher in longitudinal directionality (*i.e.* along the muscle axis) than in transverse directionality (*i.e.* across muscle fibers).

3.2 Methods

3.2.1 Subjects

Ten healthy male subjects (age: 29 ± 5 years, height: 175 ± 9 cm, body mass: 71 ± 8 kg), with no overt sign of neuromuscular diseases, volunteered to participate in the present study and signed an informed consent form. All subjects were right handed. The thickness of the skin and fat layer overlaying the biceps brachii muscle at each longitudinal distance (0 - $4\Delta y$), ranged from 1.7 - 5.8mm when measured with ultrasound B-mode images (see Fig. 25 for examples). This study was conducted according to the protocol approved by the Institutional Review Board of the Georgia Institute of Technology.

3.2.2 Experimental Setup

All fifteen accelerometers were arranged on a 3×5 grid (see Fig. 26). The main biceps axis was determined based on anatomical landmarks for each subject as extending from the origin of the tendon of insertion (distally) to the coracoid process of the scapula (proximally) [33]. For each subject, the sensor grid axis (and thus imaging plane) was approximately aligned with the longitudinal axis of the biceps brachii, which corresponds to the muscle fiber orientation since the biceps has a simple fusiform architecture, at least in its lower section [60]. The transverse sensor spacing (i.e. along the medial-lateral direction) was set to $\Delta x = 2$ cm which was the smallest achievable separation distance given the sensor diameter ($\sim$1 cm). Since the tested biceps brachii muscles differed in length for each subject, the longitudinal spacing distance Δy (i.e. along the proximal-distal direction) between adjacent accelerometers was determined as 8% of the estimated length (L_m, with $26cm < L_m < 34cm$) of the biceps brachii long head muscle, following a previous approach [60, 62]. In this study, Δy varied from 2.1 cm to 2.7 cm for the tested muscles, to ensure that the accelerometers were placed in anatomically comparable positions on each subject's

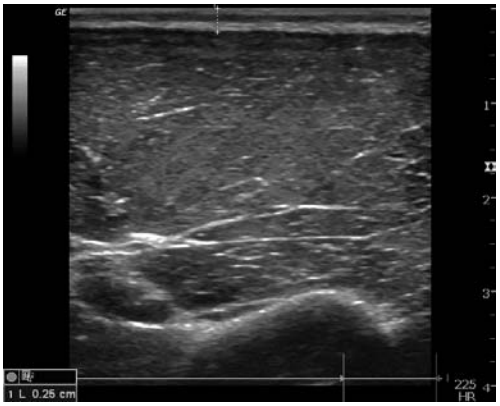

(a)

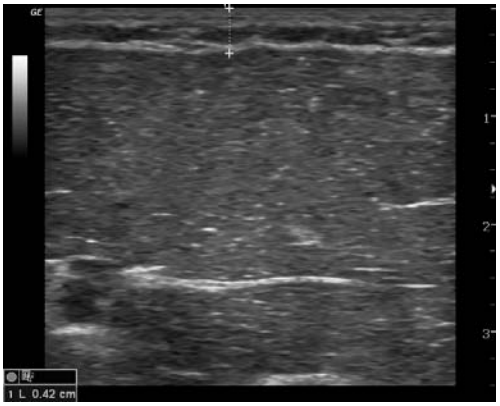

(b)

Figure 25: Example of skin and fat layer measurement with B-mode ultrasound images, where the vertical dashed line connecting the two crosses at the top center of each image measure the thickness of the skin and fat layer of a) 0.25 cm b) 0.42 cm.

biceps brachii muscle. Consequently in all cases, the 3x5 sensor grid covered the region between 18% and 50% of L_m, where the coordinate origin was set at the distal end (0% of L_m) [60].

Fifteen miniature single-axis accelerometers (PCB® A352C65, mass=2 g, base diameter=9.5 mm, sensitivity=100 mV/g) were used with thin flexible cables to reduce drag (<1 mm diameter) to record S-MMG over the biceps muscle (as seen on Fig. 26). The accelerometers were skin-mounted over the biceps brachii using double-sided medical tape to provide good contact while minimizing mounting artifacts and allowing for the muscle to move freely without any addition pressure interference, thus

yielding reliable S-MMG signals as shown in previous studies [63]. Skin-mounted accelerometers allow for very sensitive measurements of local muscle vibrations (accelerations here) with the advantage of automatically tracking any muscle motion since they are attached to it, but with the potential disadvantage of causing mass loading artifacts.

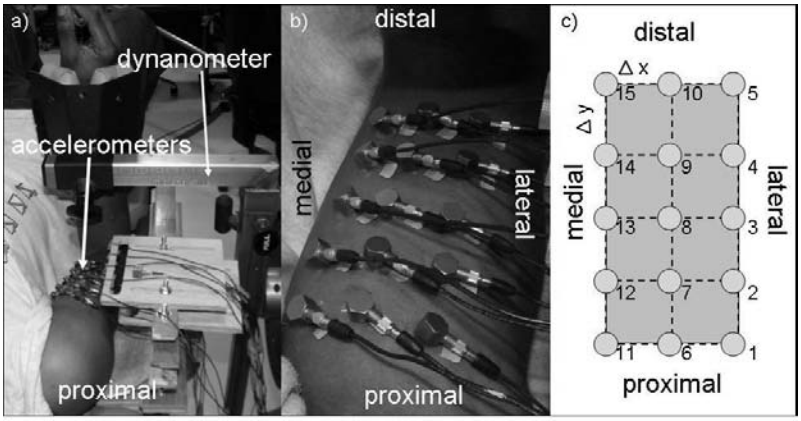

Figure 26: a) Experimental set-up for isometric elbow flexion tests (without sensor). b) Top view with skin-mounted accelerometers. c) Schematic of the 15 accelerometers locations.

3.2.3 Experimental Protocol

All 15 channels were perfectly time synchronized with a sampling frequency of 1 kHz on a Compact DAQ system (National Instrument®, Austin, TX, same as device used in Aim 1).

For each subject, S-MMGs were recorded over the biceps brachii muscle during short ($t = 10\ s$) voluntary isometric contractions (elbow flexion) which allows for a constant muscle torque output and relatively static experimental conditions. The computer-controlled dynamometer HUMAC (CSMi Medical Solutions, Stoughton, MA) was used as a platform. Each subject was situated laying on their back with their right arm attached to the dynamometer at the wrist (see Fig. 1(a)). The elbow

joint was flexed at 90 degrees and the wrist was oriented in the neutral position. The right arm was immobilized horizontally using a supporting stand to minimize motion artifacts. The rotation axis of the elbow joint was visually aligned with the rotation axis of the HUMAC dynamometer. The force output of the biceps was recorded independently by a force transducer attached to a bar at the subject's wrist. As seen in Fig. 1(a), the accelerometer cables were attached to a board that was extended from a vertical platform. The board was extended so that it minimizes the length of the cables extending from the accelerometer before the cables where attached to a stable structure, which minimized the drag of the cable on the accelerometers. A preliminary study has confirmed that this configuration isolated the accelerometers from the vibration caused by the subject's contraction by comparing the amplitude of vibration of the board to the amplitude of vibration being measured on the muscle and on the dynamometer. See Figure 27 for equipment and signal flow of experimental setup.

For each subject, the maximum voluntary contraction (MVC) force was determined based on the maximum force output measured over 3 brief maximal contractions. Thereafter, subjects performed sub-maximal isometric contractions, in which they were asked to produce and maintain 20%, 40%, 60% (see Fig. 28) of maximal voluntary contraction (MVC) force for 10 s while facing a video monitor displaying torque output as visual feedback. Subjects were encouraged to rest and relax for 3 min between each contraction to minimize artifacts due to muscular fatigue. A total of three trials were performed by selecting a randomized order of contraction levels.

3.2.3.1 Experimental Limitations

There were a few limitations encountered during the experimental setup and experimental protocol design. One limitation found was that the accelerometers have

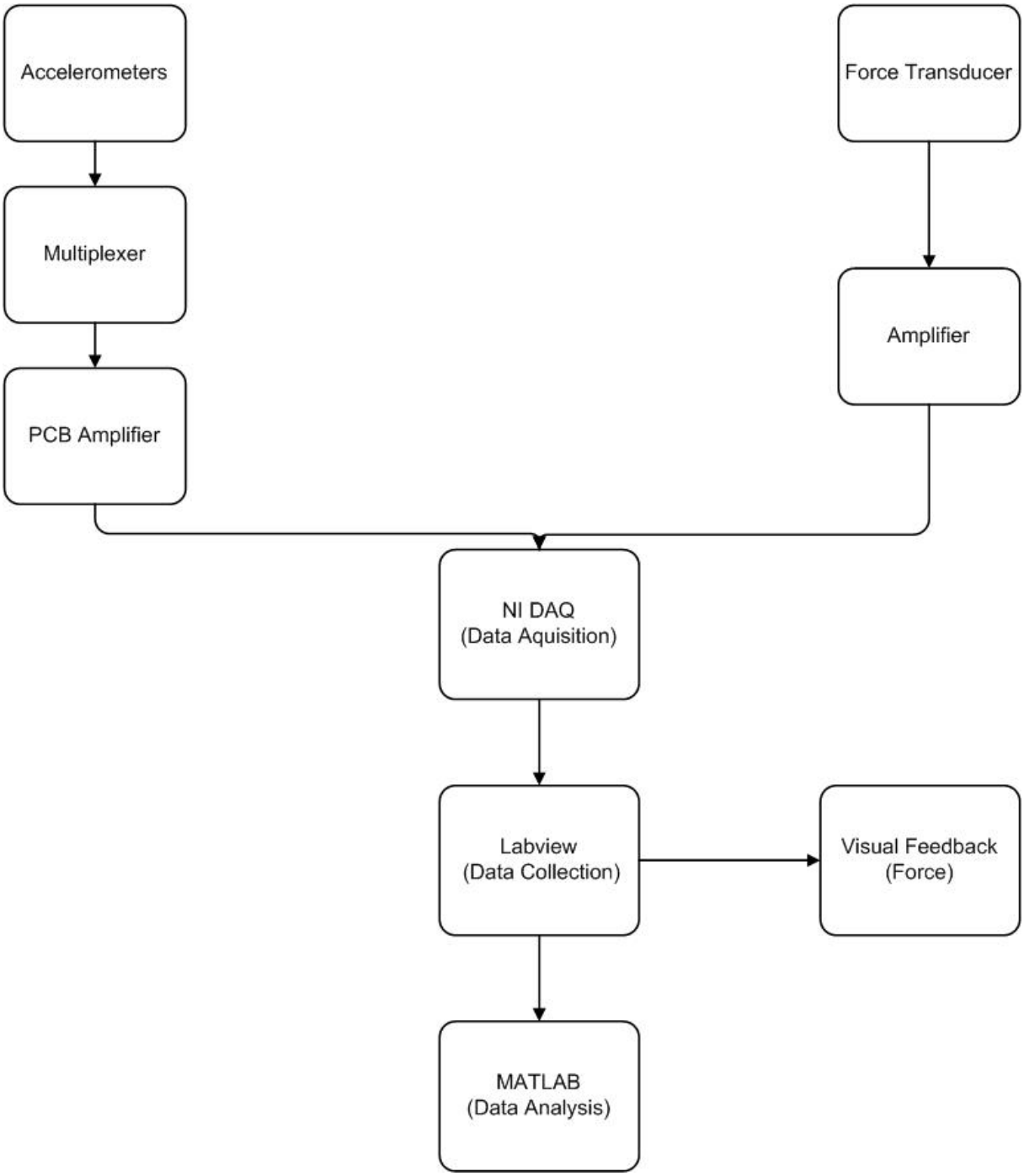

Figure 27: a) Flow chart depicting equipment flow of the experimental setup used for this study (see snapshot of the sensor placement in Figure 26).

two drawbacks when being used in under these conditions; 1) the cables that are attached to the accelerometers may have caused some drag on the accelerometers

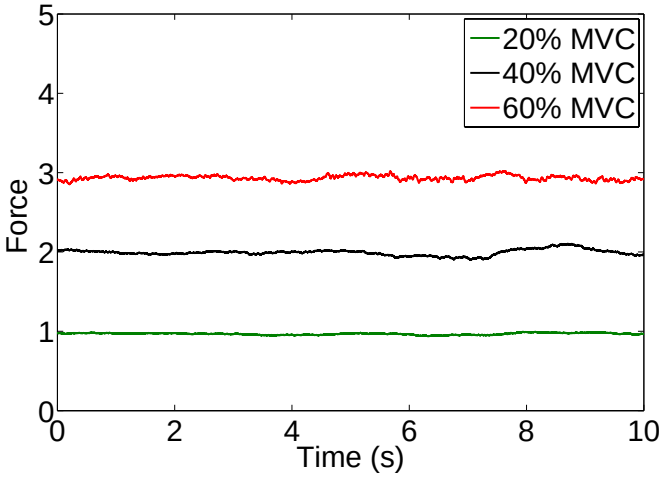

Figure 28: Example of force recording from Subject 9 Trial 1.

and 2) the weight of the accelerometers may be interfering with the measurements of the S-MMGs. Using a laser vibrometer could potentially solve these limitations, but it would also introduce new limitations that the accelerometers can overcome. The accelerometers have the advantage of being attached to the skin, therefore they have a better change of measuring signal from the same point on the muscle even if the muscle moves. With non-contact methods, such as the laser vibrometer, the measurements would be from a completely different point if the subject moves.

3.2.4 Data Pre-processing

Data was bandpass filtered in the frequency band (5 Hz - 100 Hz) and amplified with a gain of 200. Figure 29(a) shows the raw S-MMG collection before any data processing. The contraction level of 40% MVC (red) is plotted with the baseline of 0% MVC (black) to show the difference in acceleration amplitude during an isometric voluntary contraction. Notice the low frequency oscillations in both recorded S-MMG signals. During the signal processing a 2nd order Butterworth filter was used to filter out data outside of a 5 Hz to 100 Hz freqency range. The zero mean of the signal in Fig. 29(b) shows that this process filtered out the low frequency signal that arose

from whole limb motion. The fact that the two signals are 'zero mean signals' is critical in determining the coherence between two signals.

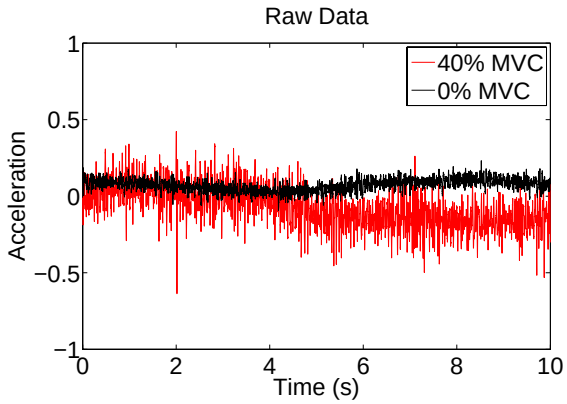

(a)

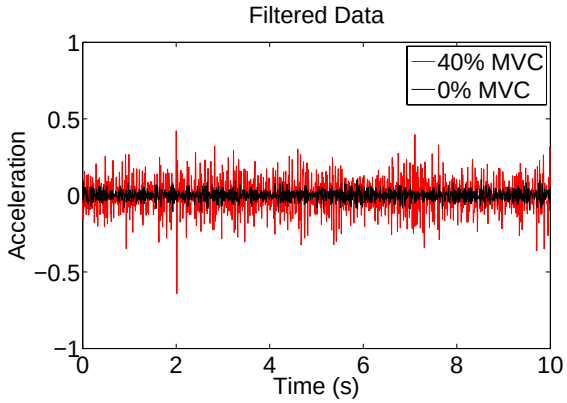

(b)

Figure 29: S-MMG data vs. time for sensor #8 at 0% MVC (baseline) and 40% MVC) for a) raw (non filtered) and b) filtered between 5 Hz and 250 Hz for Subject 10 trial #1 .

The mean power frequency (f_{MP}) of the recorded signal is defined by Kwatny et al. [40] as

$$f_{MP} = \frac{\int_{f_1}^{f_2} f G_{xx}(f)}{\int_{f_1}^{f_2} G_{xx}(f)} \tag{6}$$

where $G_{xx}(f)$ is the power spectrum of the signal $x(t)$, f is the frequency, f_1 =5 Hz and f_2 =250 Hz. The f_{MP} of each of the 15 sensors was calculated according to Equation 6 for each trial and contraction level.

These values were then averaged over the 15 sensors and 3 trials which gave a value corresponding to one subject for each contraction level. The mean power frequency averaged across sensors, trials and subjects for 20%, 40% and 60% MVC are 27.4 ± 3.0 Hz, 30.9 ± 3.2 Hz and 33.7 ± 3.5 Hz, respectively. Figure 30 shows this value averaged across all 10 subjects with the error bars indicating one standard deviation. The results show that as contraction intensity increases, f_{MP} also increases, which is consistent with a previous study done using accelerometers to measure S-MMGs over the biceps brachii muscle during isometric contractions [39].

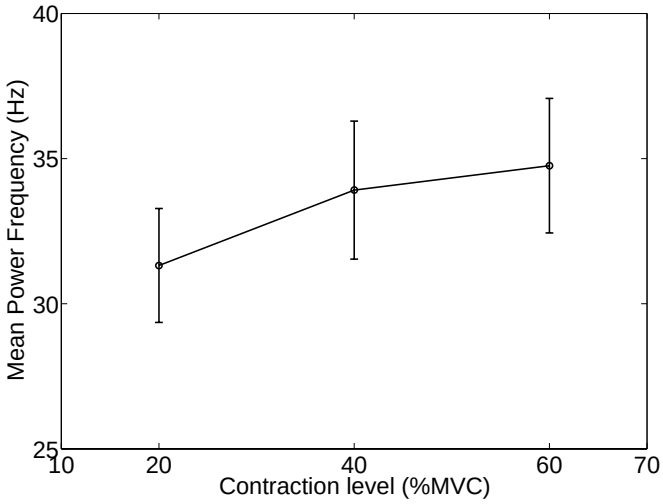

Figure 30: Average mean power frequency (f_{MP}) of S-MMG across 10 subjects for 3 different contraction levels (20%, 40% and 60% MVC).

As an illustration, Fig. 31 shows the FFT (of sensor #8 for subject 5 and trial 2) across frequency for increasing contraction level. Compared with the noise in the resting muscle (0 %MVC), the power increased as contraction level increased.

The signal to noise ratio was defined as the power ratio between the meaningful S-MMG (measured signal at a contraction level greater than 0% MVC) and noise (measured signal at rest). The power was averaged between 5 Hz - 250 Hz for each signal. The S-MMG measured at each sensor was averaged over the 15 sensors for a single trial. This value was then averaged over the three trials, in order to obtain

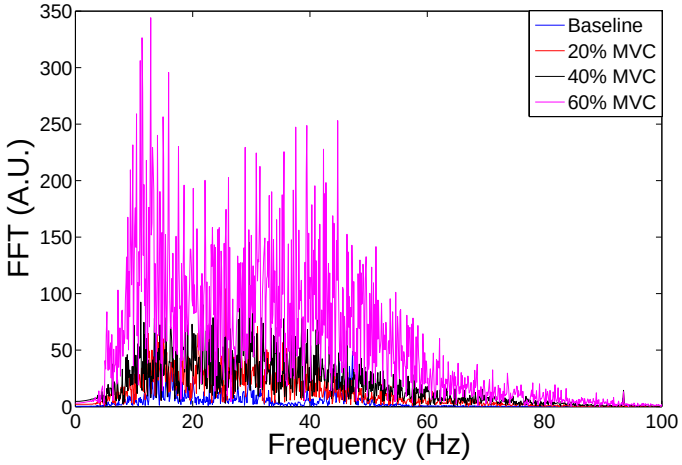

Figure 31: Frequency spectrum for subject 5 measured on sensor # 8 for trail #2 for varying %MVC.

a value for each subject at each contraction level. These values were then averaged across the 10 subjects to obtain the mean and standard deviation for each contraction level. The signals obtained from the S-MMGs were found to have a high signal to noise ratio (see Fig. 3.2.4). Compared with the noise in the resting muscle (0 %MVC), the signal to noise ratio increased as contraction level increased ($P < 0.01$).

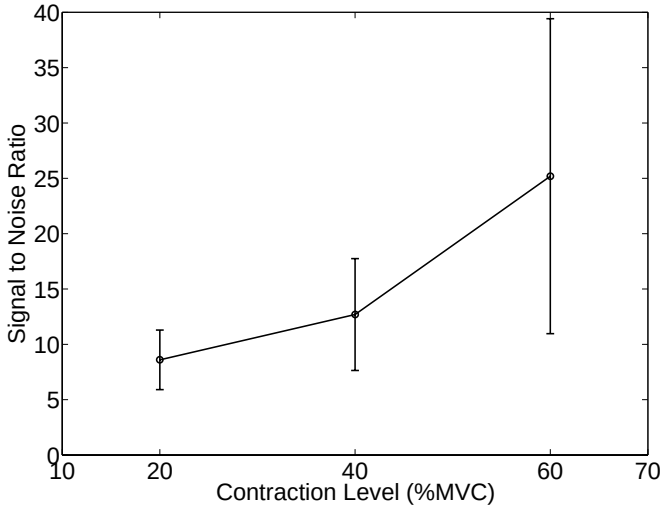

Figure 32: Signal to noise ratio across all recorded signal varied by contraction level (error bar is one standard deviation)

3.2.5 Theory - Signal Processing Techniques

The spatial coherence of two S-MMG signals can be determined from two different methods, this section explores the background on the different methods. First, the similarity in the frequency domain between two S-MMG signals $x(t)$ and $y(t)$ recorded at different locations along the longitudinal axis of the muscle, can be estimated from the square of the magnitude of their coherence $\mid C_{xy}(f) \mid^2$, defined as [19]

$$\mid C_{xy}(f) \mid^2 = \frac{\mid G_{xy}(f) \mid^2}{G_{xx}(f)G_{yy}(f)} \tag{7}$$

where f is the frequency of interest, $G_{xx}(f)$ (resp. $G_{yy}(f)$) is the power spectrum of the signal $x(t)$ (resp. $y(t)$), and $G_{xy}(f)$ is the cross power spectrum of those two signals. The cross-power spectrum is defined as the Fourier transform of the cross correlation function of the two signals $x(t)$ and $y(t)$ [19]. The squared magnitude coherence between the two sensors was estimated using the "mscohere" Matlab® function [1], and results in a value between 0 and 1, with 1 meaning perfectly similar and 0 meaning no similarity. In the remainder of this chapter the quantity $\mid C_{xy}(f) \mid^2$ is referred to as the magnitude squared coherence.

For each test, the first and last .25 s were clipped from the signal, meaning the total signal time of 9.5 s was used to calculate the coherence between pairs of S-MMG signals(see Eq. (7)). The power spectrum and cross-spectrum of the recorded S-MMG were estimated by segmenting the S-MMG time series in overlapping windows ($N = 1100$ points long with 50% overlap) and the number of samples for the fast fourier transform operation was selected as 256. Confidence intervals of the coherence function can be estimated to achieve a desired level of significance, based on an analytical expression of the variance of the coherence [14, 12]. The confidence level

cl of the coherence function, at the α quantile is given by [36]

$$cl = 1 - (1 - \alpha)^{\frac{1}{L-1}} \tag{8}$$

where L is the signal duration multiplied by the sampling frequency of the recording ($Fe = 1000\ Hz$) divided by the window length ($N = 1100$ points). Such that

$$L = \frac{(T)(Fe)}{N} = \frac{(9.5\ s)(1000\ Hz)}{1100} = 8.6364 \tag{9}$$

In this study the confidence level was set to $cl \approx 0.32$ using Eq. (8), based on the selected parameters $\alpha = 0.95$, $L = 8.6364$.

At each contraction level (%MVC) the frequency-averaged coherence $\mid C_{xy}(f_c) \mid^2$, for varying center frequency f_c was defined as:

$$\mid C_{xy}(f_c) \mid^2 \simeq \int_{f_c-\Delta f}^{f_c+\Delta f} \mid C_{xy}(f) \mid^2 \mathrm{d}f \tag{10}$$

where Δf=2 Hz.

Another method to calculate the similarity between two S-MMG signals $x(t)$ and $y(t)$ recorded at different locations is by using the time-domain cross-correlation function. The cross-correlation function is approximately equal to the frequency averaged coherence of two signals, as the frequency band of interest approaches 0 [29]. With continuous time signals the normalized cross correlation function between two S-MMG signals $x(t)$ and $y(t)$ is defined by

$$R_{xy}(\tau) = \frac{\int_{-T/2}^{T/2} x(t)y(t+\tau)\mathrm{d}t}{\sqrt{\int_{-T/2}^{T/2} x^2(t)\mathrm{d}t \int_{-T/2}^{T/2} y^2(t)\mathrm{d}t}} \tag{11}$$

where the signals $x(t)$ and $y(t)$ both filtered with a bandpass filter with a frequency band of $f_c \pm \Delta f$ with Δf=2 Hz. The function is normalized between +1 and 0, where +1 indicates a perfect similarity between the two signals and 0 indicates no similarity.

The cross correlation peak X_{xy} is then defined as

$$X_{xy}(f_c) = max(R_{xy}(\tau)) \tag{12}$$

The two signal processing techniques described above can be used to determine the spatial coherence. Fig. 33 gives a flow chart that details the steps taken on the two different routes to determine the spatial coherence.

3.2.5.1 Spatial Coherence Technique to Determine Directionality

Recall from Section 3.2.5 that there are two separate processes used to determine the spatial coherence of two S-MMG signals. Using the fact that the spatial coherence values vary between 0 and 1, (with 0 meaning no similarity and 1 being completely similar) the directionality of S-MMG propagation can be determined by comparing spatial coherence on longitudinal pairs versus transverse pairs. Before this was accomplished the understanding of the main effect of several factors that influence the S-MMG spatial coherence was investigated. A 15 $\times$ 15 color coded matrix of spatial coherence values is used to analyze the directionality. In this matrix, the 5 $\times$ 5 square boxes located on the diagonal from the lower left to the upper right denotes sensor pairs on the same longitudinal line. The main effect of the factor alone averaged across the levels of the other factors, was investigated. The factors investigated were frequency, sensor separation distance (2,4,6 and 8 cm longitudinal direction and 2 and 4 cm transverse direction), contraction level (20% MVC, 40% MVC and 60% MVC) and sensor orientation (longitudinal vs transverse). With the frequency as the main effect all other factors were averaged, but the sensor orientation was kept separate. For the remaining factors the frequency was averaged in a 4 Hz frequency band centered about f_{MP} while the other factors were averaged across all levels.

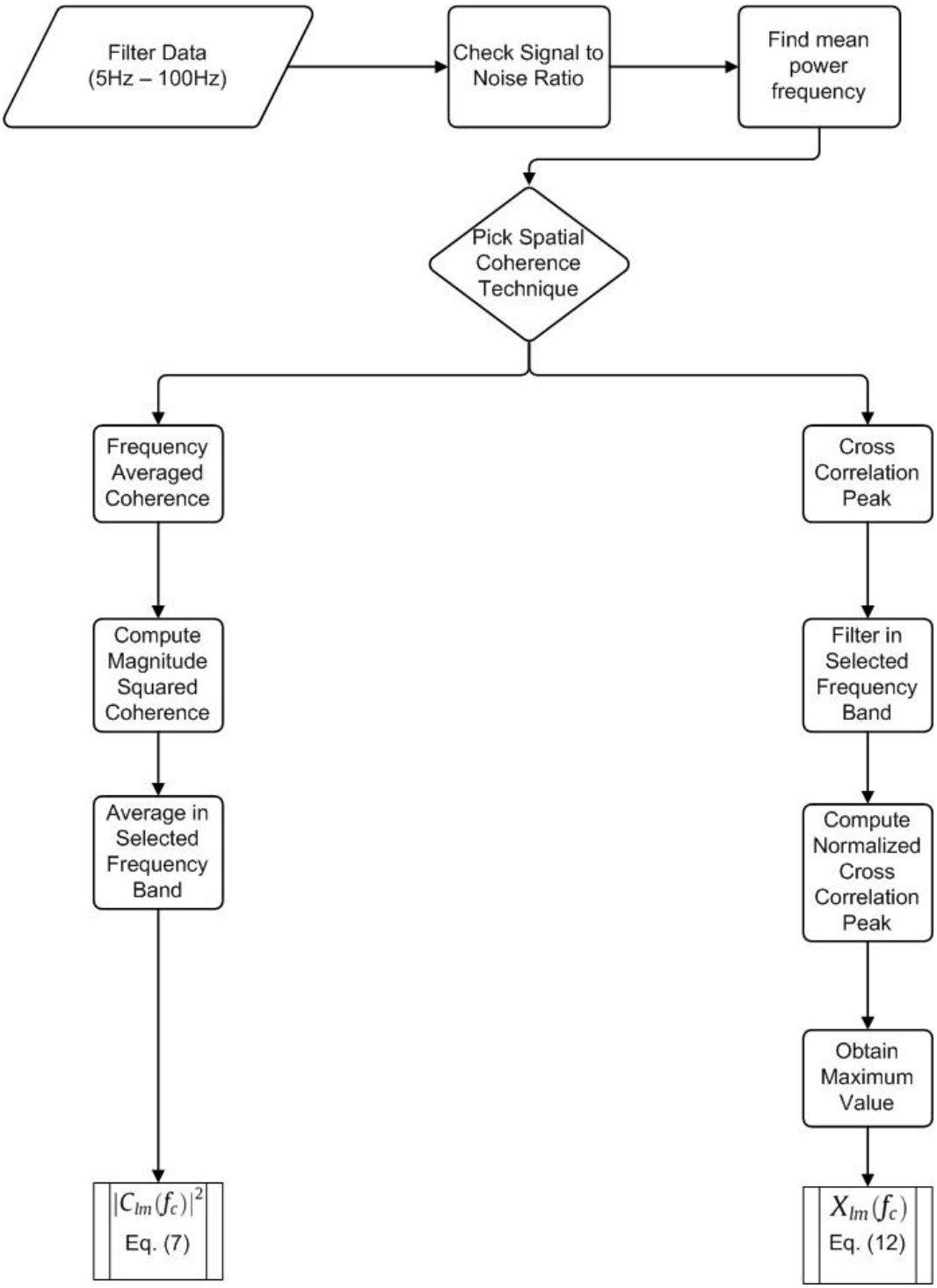

Figure 33: Flow chart depicting the two processes used in order to determine the magnitude squared coherence and the cross correlation peak.

3.2.6 Statistical Analysis

Statistical analysis was performed to determine if there was statistical significance to the values of f_{MP}, which showed to increase as contraction level increased. The f_{MP} was found for each sensor and averaged across all 15 sensors for each trial. The 3 trials were then averaged to give a single f_{MP} for each subject at each contraction level. These values were then averaged and plotted with the error bars indicating one standard deviation. A one way analysis of variance (ANOVA) was used to determine statistical significance with the dependent variable being spatial coherence and the independent variable being contraction level. Three separate one-way ANOVA tests were performed in order to asses the influence on spatial coherence of 3 different factors; frequency, sensor separation distance and contraction level. For the frequency analysis longitudinal and transverse sensor pairs were kept separate, while they were averaged across trials, subjects, sensor separation distance and contraction intensities. The coherence value at 10 Hz intervals was used to determine statistical significance. Determining the main effect of the sensor separation distance was done by averaging the spatial coherence across trials, subjects and contraction level. To determine the effect of contraction level on the spatial coherence, the spatial coherence values were averaged across, trials, subjects and sensor separation distances. An alpha level of 0.05 was used for all statistical comparisons, where appropriate $P < 0.05$ and $P < 0.01$ was noted. Unless otherwise stated the error bars in the figures represent one standard deviation.

3.3 Results

The Fast Fourier Transform (FFT) of the S-MMG data gives the frequency content of the recorded signal. This information revealed the importance of the frequency content of the data, which showed that there was no significant signal past approximately 80 Hz when compared to the baseline. Figure 34 shows the frequency content

of sensor #8 at 40% MVC and at 0% MVC (baseline). It can be seen that there is a high amount of activity (even in the baseline measurement) below about 12 Hz which may be attributed to muscle tremor. After about 12 Hz there is activity that can be attributed to the muscle "noise" generated during a voluntary isometric contraction.

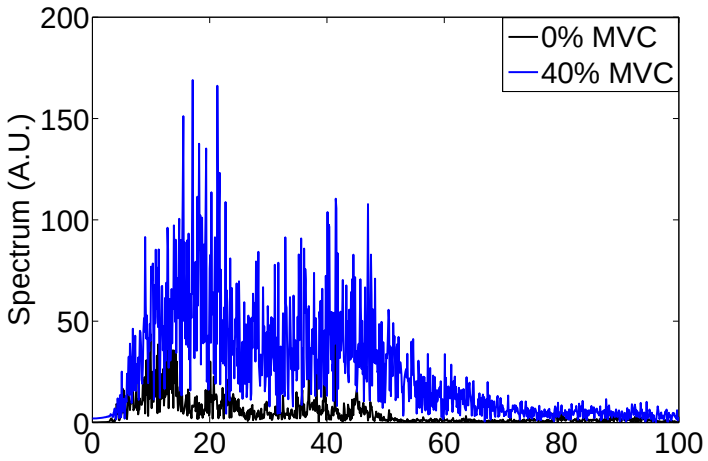

Figure 34: FFT of the filtered time domain S-MMG data for subject 10, trial 1, sensor #8 (at 0% MVC (baseline) and 40% MVC)

Fig. 35 illustrates the influence of various parameters such as contraction level, sensor separation distance and sensor pair orientation (e.g. longitudinal vs. transverse) on the frequency-dependency of the computed S-MMG coherence for all subjects. Figures 35(a) and 35(c) contrast the effects of sensor pair orientation and distance on the S-MMG coherence function. Figure 35(a) shows the coherence function between the reference sensor #6 and the four other sensors $\#7 - \#10$ aligned along the same vertical grid line (i.e. longitudinal direction) and Fig. 35(c) displays the coherence function between the reference sensor #3 and the two other sensors $\#8 - \#13$ aligned along the same horizontal grid line (i.e. transverse direction) (see Fig. 26(c)) at 40% MVC. Fig. 35(a) shows that the coherence values decrease for increasing frequencies and increasing sensor separation distance, as expected from theoretical predictions. The coherence values remain significant (i.e. > 0.32, see

Eq. (8)) over a wider frequency range for sensor pairs oriented in the longitudinal direction, i.e. along the muscle fiber direction (Fig. 36(a), 62.38 ± 4.54 Hz), when compared to sensor pairs oriented in the transverse direction (Fig. 36(b) 31.70 ± 3.88 Hz), i.e. across the muscle fiber direction. Fig. 35(b) and Fig. 35(d) illustrate how S-MMG spatial coherence vary for increasing contraction level for two sensor pairs aligned either along the longitudinal (pair #7 − #9, 4.2cm< $2\Delta y$ <5.4cm) or transverse (pair #3 − #13, $2\Delta x$ =4cm) direction but having a similar separation distance. The frequency value at which the coherence drops belows the significant value (0.32 denoted by dashed horizontal line) increased as contraction level increased in the longitudinal direction (Fig. 35(b)) although not in the transverse direction (Fig. 35(d)). Overall, Fig. 35 shows that the spatial coherence of S-MMGs can vary significantly with the contraction level and sensor pairs orientation, especially at higher frequencies ($f > 20$ Hz). Hence, the dependency of the spatial coherence S-MMG on each of the various aforementioned parameters are investigated systematically in the subsequent figures.

Figure 36 shows the coherence with frequency as the main effect for the longitudinal direction (Fig. 36(a)) and the transverse direction (Fig 36(b)). For sensor pairs oriented in the longitudinal direction coherence was found to decrease with increasing frequency ($P < 0.01$). The coherence in the transverse direction was also found to decrease as frequency increased ($P < 0.05$). The frequency at which the coherence drops below the significant coherence threshold of 0.32 (cut-off frequency, denoted by horizontal dashed line) for all longitudinal pairs was 62.38 ± 4.54 Hz, which was significantly different from all transverse pairs at 31.70 ± 3.88 Hz ($P < 0.01$). The cut-off frequency was averaged across all contraction levels, sensor separation distances and subjects.

Figure 37 displays a matrix in a checkerboard format, showing the typical variations of the frequency averaged coherence function (Figs. 37(b) and 37(a)) and the

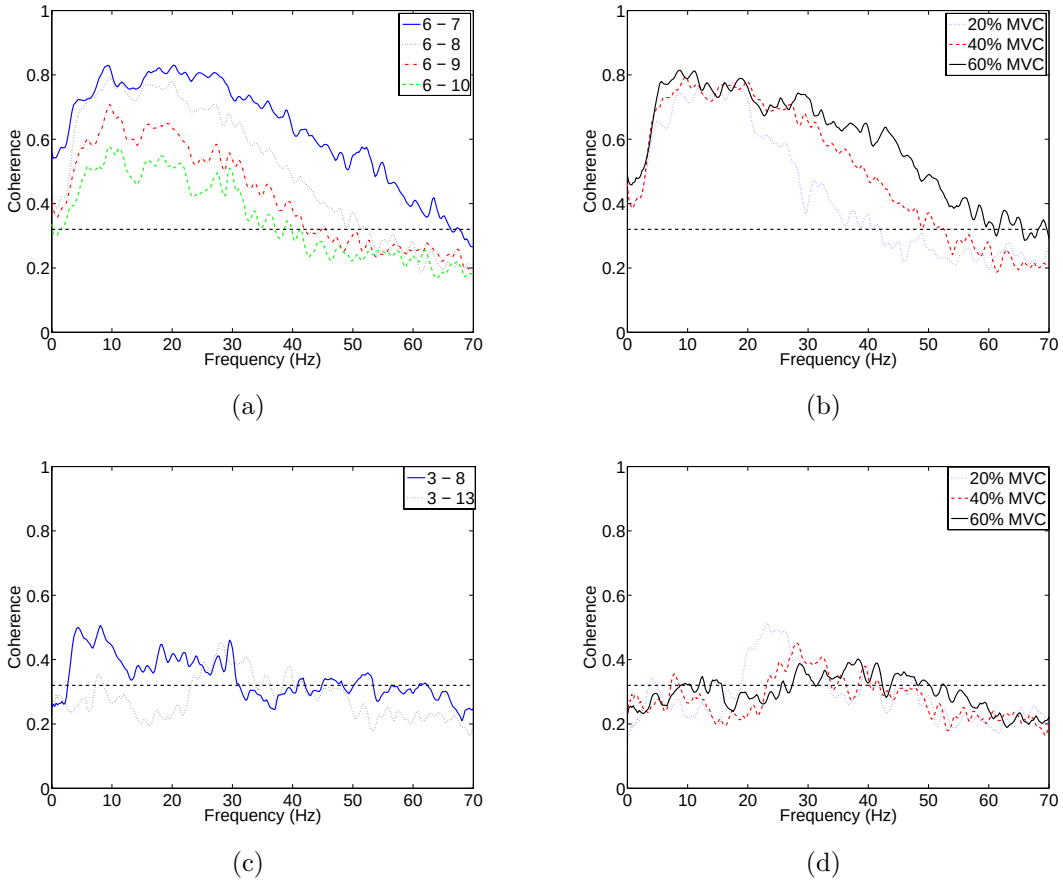

Figure 35: S-MMG coherence averaged over the 10 subjects at the same contraction level (40 % MVC) for increasing separation distance between pairs of skin mounted accelerometers located on the (a) central longitudinal sensor line (b) central transverse sensor line (see Fig. 1(c)). S-MMG coherence at a fixed distance r, for increasing % MVC between a pair of skin mounted accelerometers located on the center (c) longitudinal sensor line (sensor pair $\#7 - \#9$) (d) transverse sensor line (sensor pair $\#3 - \#13$, $r = 4$ cm).

peak value of the normalized cross correlation (Figs. 37(d) and 37(c)) of S-MMGs between all sensor pairs (see Eq.(7) and Eq.(11)). For each sensor pair the frequency averaged coherence values were averaged in 4 Hz frequency bands (see Eq.(10)) and the cross correlation was filtered in a 4 Hz frequency band, centered respectively at one third of the mean power frequency (low) and at the mean power frequency (high). For each checkerboard matrix, the spatial coherence values were averaged across all 10 subjects and across 3 trials. It can be seen that at both low frequency ($\frac{1}{3}f_{MP}$, Figs.

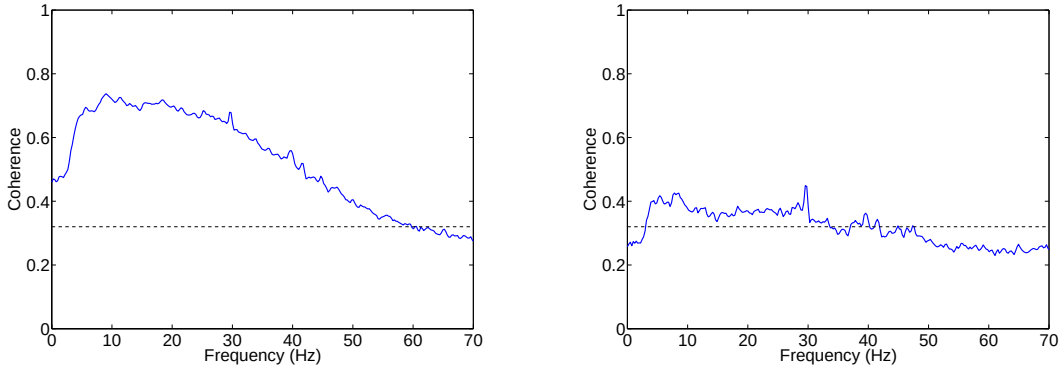

(a) (b)

Figure 36: S-MMG coherence averaged across all 3 contraction intensities, all 10 subjects and (a) all sensor pairs oriented in the longitudinal direction (b) all sensor pairs oriented in the transverse direction.

37(b) and 37(d)) and high frequency (f_{MP}, Figs. 37(a) and 37(c)) the checkerboard has higher values concentrated along a 5×5 diagonal. These correspond to 5 sensors located on the same vertical grid line (medial, central or lateral, see Fig. 1(c)).

An analysis was performed that compared the frequency averaged coherence $\mid C_{xy}(f_c) \mid^2$ and the cross correlation peak $X_{xy}(f_c)$ between pairs of sensors with the same inter sensor separation distance along an individual longitudinal line (medial, central or lateral). The spatial coherence values computed for all 3 longitudinal lines were very comparable, within 4% of each other. Hence, it was concluded that the values for the three longitudinal lines were not statistically different, therefore for Fig. 38 the values along the three lines were averaged together. At a given center frequency $f_c = \frac{1}{3} f_{MP}$ (Figs. 38(a) and 38(c)) or $f_c = f_{MP}$ Figs. 38(b) and 38(d)) and contraction level, Fig. 39 displays the mean and standard deviation values obtained after averaging all computed longitudinal coherence values (along medial, central and lateral lines) using Eq. (10) and Eq. (11) for all analyzed 9.5 s long S-MMG epochs (see section 3.2.3) and all subjects. Figure 39 display the mean variation of the frequency-averaged coherence values (at 40% MVC) for increasing sensor separation distance, for the same low and high frequency bands centered respectively at $\frac{1}{3} f_{MP}$

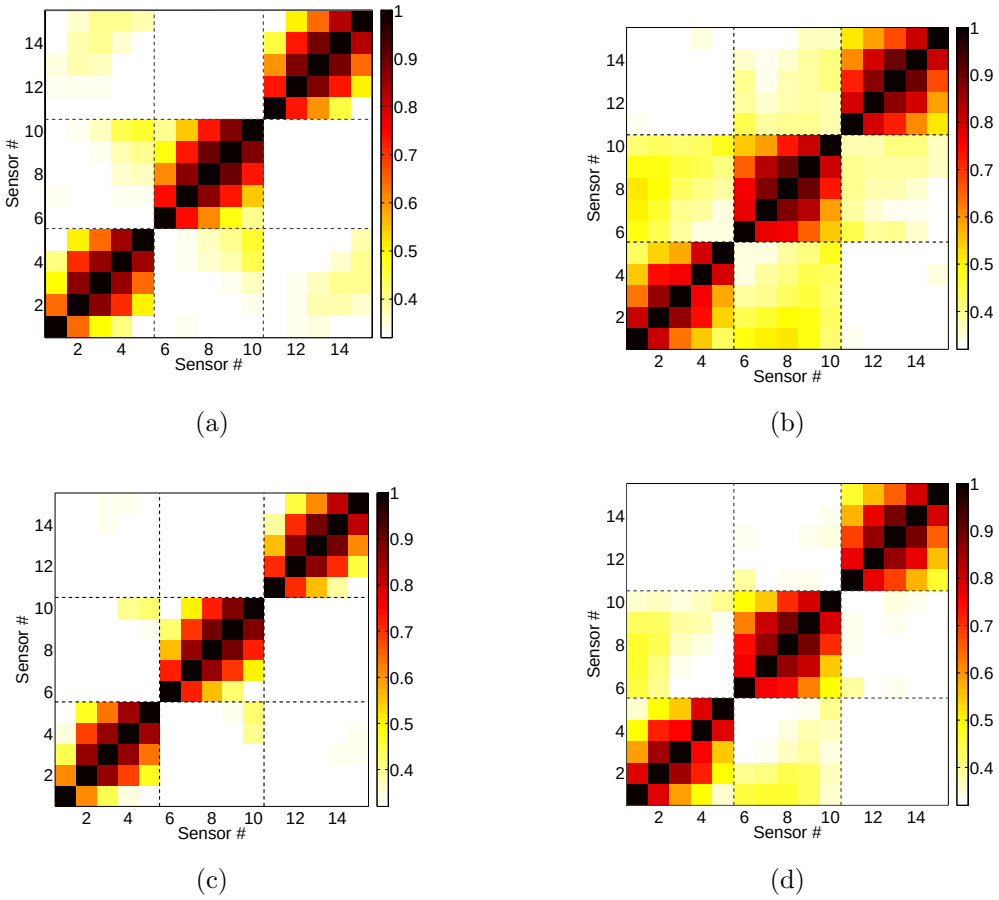

Figure 37: Magnitude squared coherence values $\mid C_{lm}(f_c) \mid^2$ (10) between all sensor pairs centered at (a) f_{MP} and (b) $\frac{1}{3}f_{MP}$. Normalized cross correlation peak values $X_{lm}(f_c)$ (12) between all sensor pairs centered at (c) f_{MP} and (d) $\frac{1}{3}f_{MP}$. Data were averaged across trials, contraction levels, and subjects.

and at the f_{MP} as in Fig. 37. These computed values were averaged both over all 10 subjects with 3 trials and over all equidistant longitudinal sensor pairs for increasing normalized separation distance from Δy to $4\Delta y$ ($2.1\ cm \leq \Delta y \leq 2.7\ cm$ (see Section 3.2.3)). Figure 39 confirms that the frequency-averaged coherence value and the cross correlation peak (in a 4 Hz frequency band) centered both at $\frac{1}{3}f_{MP}$ and at the f_{MP}, decreased as the sensor separation distance increases, as previously observed (see Fig. 35).

An analysis was performed to show the main affect of sensor separation distance on spatial coherence, measuring the spatial coherence for all equidistant sensor pairs

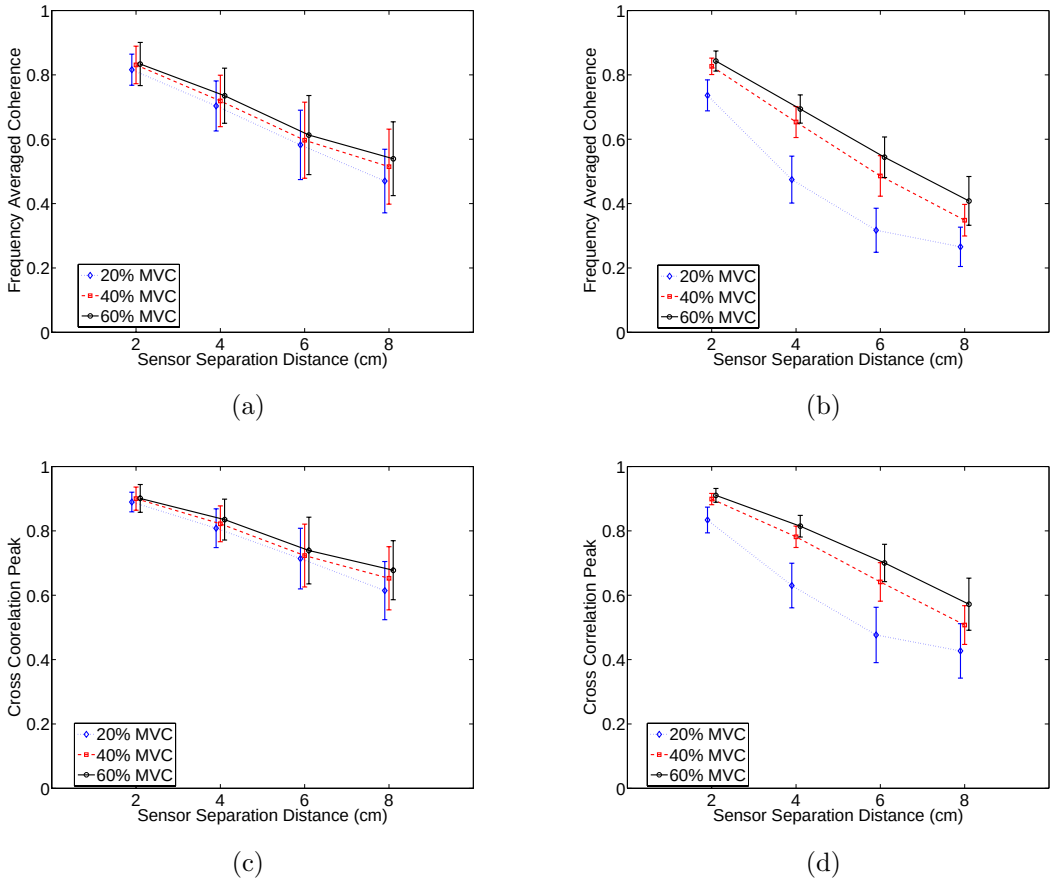

Figure 38: Coherence value averaged in 4 Hz frequency band at different contraction levels (% MVC) for increasing sensor separation distance at (a) $\frac{1}{3}f_{MP}$ and (b) f_{MP}. Cross correlation peak value filtered in 4 Hz frequency band at different contraction levels (% MVC) for increasing sensor separation distance at (c) $\frac{1}{3}f_{MP}$ and (d) f_{MP}. Error bars indicate one standard deviation over all 10 subjects and sensor separation distance combinations.

from Δy to $4\Delta y$ ($2.1\ cm \leq \Delta y \leq 2.7\ cm$) and from Δx to $2\Delta x$ ($\Delta x = 2.0\ cm$) (see Section 3.2.3)). The spatial coherence values were averaged across trials, subjects and contraction level. The sensor separation distances were averaged for all sensors with a common separation distance, along the same line. The S-MMG coherence decreased with increasing distance ($P < 0.01$) along the longitudinal direction for both frequency bands (Figure 39(a)). When collapsed across sensor separation distances along the longitudinal direction, the S-MMG coherence centered at $\frac{1}{3}f_{MP}$ were higher ($P < 0.01$) compared with the one at f_{MP}. The pair-wise difference was significant ($P <$

0.01) at all sensor separation distances greater than Δy. In the transverse direction, the S-MMG coherence at $\frac{1}{3}f_{MP}$ were higher ($P < 0.05$) than the one centered at f_{MP} at Δx =2 cm (Figure 39(b)).

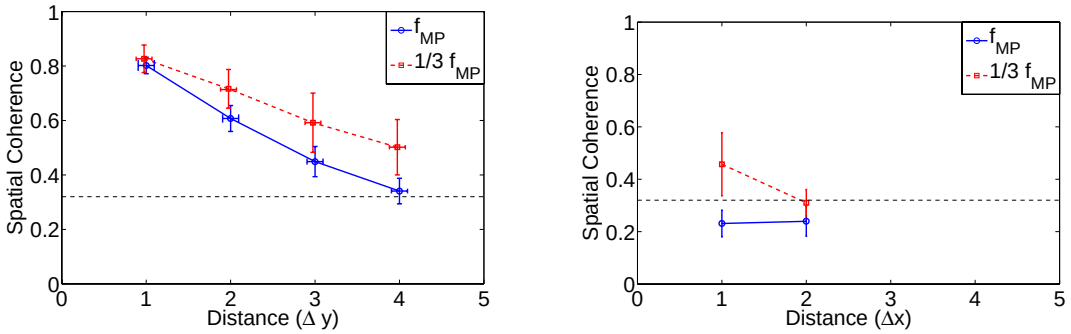

(a) (b)

Figure 39: Spatial coherence for 2 frequency bands in the (a) longitudinal and (b) transverse directions as a function of sensor distance. The spatial coherence values in a 4 Hz frequency band centered at f_{MP} and at $\frac{1}{3}f_{MP}$ were averaged for all longitudinal sensor pairs spaced apart by Δy to $4\Delta y$ (2.1 cm $\leq \Delta y \leq$ 2.7 cm) and all transverse sensor pairs spaced apart by Δx to $2\Delta x$ (Δx = 2.0 cm) across trials, contraction levels, and subjects. The sensor separation distance was averaged across sensors with a common separation distance along the (a) longitudinal and (b) transverse directions.

The spatial coherence is also dependent on contraction level. Figure 40 explores the main affect of contraction level on the spatial coherence values for both longitudinal (Fig. 40(a)) and transverse (Fig. 40(b)) sensor orientation direction. The coherence values were averaged across trials, subjects and sensor separation distances for sensors pairs along the same line. In the longitudinal direction, the S-MMG coherence increased as contraction level increased ($P < 0.01$) only for f_c=f_{MP} (Fig. 40(a)). There was no effect of contraction level in the transverse direction (Fig. 40(b)). Figure 40 shows the main effect of contraction level on S-MMG coherence for longitudinal (Fig. 40(a)) and transverse (Fig. 40(b)) sensor orientation direction.

Figure 41 compares the overall spatial coherence value across all trials, subjects,

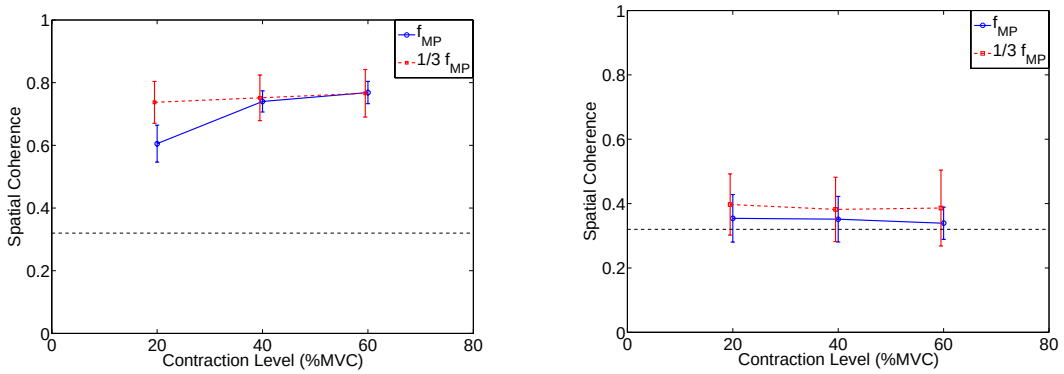

Figure 40: The S-MMG coherence values $\mid C_{lm}(f_c) \mid^2$ for 2 frequency bands in the (a) longitudinal and (b) transverse directions as a function of contraction level. Data in 4 Hz frequency band atf_{MP} or at $\frac{1}{3}f_{MP}$ were averaged for all comparable sensor separation distances of Δy to $2\Delta y$ and Δx to $2\Delta x$ along the (a) longitudinal direction or (b) transverse direction across trials and subjects at each contraction level.

sensor separation distances and contraction level for longitudinal and transverse directions. When focusing on the main effect of sensor pair orientation, the S-MMG coherence was greater in the longitudinal direction than in the transverse direction ($P < 0.01$) (Figure 41(a)). Using the mathematically similar metric of the normalized cross correlation peak (12), the results were the same (Figure 41(b)). The values were significantly greater ($P < 0.01$) in the frequency band centered at $\frac{1}{3}f_{MP}$ compared with the frequency band centered at f_{MP} for both metrics used.

3.4 Discussion

To begin the discussion of this chapter, the quality of the measurement taken is briefly discussed, mainly the f_{MP} and signal to noise ratio. The initial analysis of the S-MMG data collected for this study confirmed that both the S-MMG mean power frequency (f_{MP}) and S-MMG signal's intensity increased with the contraction level of the biceps (see Fig. 30), in agreement with previous studies [53, 54, 39]. In addition, the signal to noise ratio increased as contraction intensity increased, which shows that

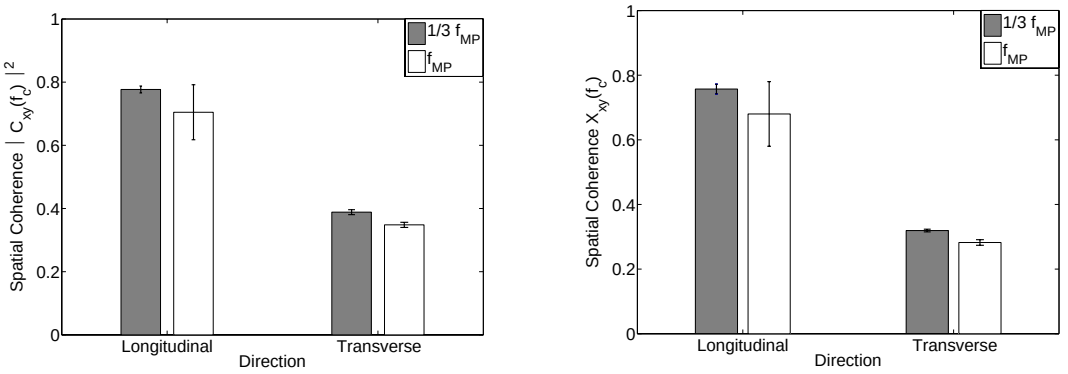

(a) (b)

Figure 41: Collapsed spatial coherence values across sensor separation distances and contraction levels in 2 frequency bands in each sensor pair orientation. (a) The magnitude square coherence $\mid C_{lm}(f_c) \mid^2$ (10) and (b) the maximum normalized ross correlations $X_{lm}(f_c)$ (12) are shown. The data were averaged for the 4 Hz frequency bands centered at $\frac{1}{3}f_{MP}$ and f_{MP}.

the experimental setup and protocol enabled good S-MMG signal measurements.

The main finding of this study is that the spatial coherence values of high frequency (i.e. close to the mean power frequency f_{MP}) S-MMG propagating between sensor pairs aligned along the biceps main axis (*i.e.* the longitudinal direction) was significantly higher than the spatial coherence values for sensor pairs oriented perpendicular to the muscle fibers (*i.e.* along the transverse direction) between the proximal and distal ends of the biceps (*i.e.* the longitudinal direction). In addition, the spatial coherence values at the lower frequency ($\frac{1}{3}f_{MP}$) are on average higher than the values at the higher (f_{MP}) frequency. These main findings supported our hypotheses.

In the current study, three additional findings were obtained. First, the cut-off frequency of the S-MMG spatial coherence (*i.e.* the frequency beyond which the spatial coherence values dropped below the confidence level) significantly increased with contraction level, when considering longitudinal sensor pairs but not transverse sensor pairs. Second, the spatial coherence values of S-MMGs along the longitudinal

direction decreased with increasing frequency and increasing sensor separation distance for both studied frequencies (f_{MP} and $\frac{1}{3}f_{MP}$). Finally, the spatial coherence values between longitudinal sensor pairs increased with contraction level, but only for the frequency band centered at f_{MP}.

These findings can be related to the physiological origin of S-MMG. The local activation of the muscle fibers typically dominates the S-MMG generation mechanism in the higher frequency band (*i.e.* $f > 25$ Hz) [53]. Furthermore, the fast twitch fibers are more superficially located than slow twitch fibers in the biceps brachii muscle [21]. Hence, in the biceps brachii, the high frequency content of S-MMG, measured with skin-mounted sensors at the biceps brachii surface, is highly influenced by the physical characteristics and orientation of fast twitch fibers, especially at high contraction level [54]. The main finding of the current study demonstrated high coherence values of high frequencies S-MMG recorded along the biceps longitudinal axis. These high coherence values indicate that a significant fraction of the muscles natural vibrations was recorded on all the selected longitudinal sensor locations. This finding is consistent with a previous preliminary study using the propagation velocity of coherent S-MMG along the biceps axis to infer muscle stiffness [62]. This likely results from the fusiform architectural organization of the biceps brachii muscle fibers [78]: the longitudinal direction corresponds to the main orientation of the biceps brachii muscle's fibers and is thus likely more homogeneous than the transverse directions, thus favoring the propagation of natural muscle vibrations [28].

Based on the first additional finding, it appears that the increase in discharge rate (associated with the increase in contraction level), is only paralleled by an increase in spatial coherence values of longitudinal sensor pairs and not transverse sensor pairs. Consequently, measurements of the spatial coherence of high-frequency S-MMG (*i.e.* $f > 25$ Hz), which are mainly generated by the a-synchronized muscle fiber activity, are likely to reflect the physiological architecture of the tested skeletal muscle. On

the other hand, the spatial coherence values for low-frequency S-MMG (f <25 Hz) appear to be significant along both the transverse and longitudinal directions. This likely occurs because low-frequency S-MMG are mainly produced by the synchronized activity of muscle fibers as a result of muscle tremor activity [11, 32] or movements of the whole limb due to motion artifacts, especially at higher contraction level. This may explain why an earlier study on S-MMGs for isometric contractions of the biceps brachii focusing on more energetic lower frequency S-MMG components (*i.e.* $f < 25$ Hz), concluded the S-MMGs propagate transversely, related to a bending transverse modal resonances of the whole biceps [59].

Finally, the second and third additional findings may result from the influence of the muscle's mechanical properties and activation level on the propagation of the mechanical vibrations along the muscle. Two main factors are likely to influence the spatial coherence values of S-MMGs for this study. First, mechanical vibrations (*e.g.* as measured by S-MMGs) become rapidly attenuated when propagating in viscoelastic materials with high damping factors or viscosity (such as skeletal muscles) [28, 30]. Additionally, the influence of viscous effects on the propagation of mechanical vibrations increases with higher frequency and longer propagation distances. Thus, the propagation distance of such mechanical vibrations is limited by the viscous attenuation and decreases as the frequency content of the vibration increases. Consequently, the viscous attenuation of the muscle likely limits the sensor separation distance over which mechanical vibrations can propagate coherently between the skin-mounted accelerometers (as observed from the second additional finding), especially as S-MMG frequency increases. Hence, at the lower frequency band, the spatial coherence vs. distance, even in the transverse direction, shows a significant difference between the two sensor separation distances (Δx, $2\Delta x$ and Δy, $2\Delta y$). Second, a more homogeneous (or spatially uniform) propagation medium favors the

undisturbed propagation of mechanical vibrations: spatial heterogeneities in mechanical properties destroy the relative phase relationships, and thus the resulting spatial coherence level, of propagating vibrations between spatially separated sensors [29]. For instance, the longitudinal direction is more mechanically homogeneous than the transverse directions [28]. Additionally, the muscle's stiffness increases as the contraction level increases [28, 30] thus increasing in turn the mechanical coupling (and homogeneity) between longitudinal sensor pairs. Consequently, the latter two effects likely cause the apparent increase in the spatial coherence values between longitudinal sensor pairs for the tested contraction levels: High frequency S-MMGs (f >25 Hz), which are less influenced by synchronous muscle activity (muscle tremor or whole limb motion), likely propagates more coherently along the muscle fiber orientation (*i.e.* longitudinal direction) in a guided fashion as the biceps stiffens.

Overall the results of this study confirm that the multichannel skin-mounted sensor arrays measure spatial variations and coupling directionality of mechanical vibrations (as measured by S-MMG) over a contracting muscle in agreement with previous related studies [62, 18, 46, 27, 17]. However, the physical characteristics of these natural vibrations have very rarely been related to the actual mechanical properties of muscle soft tissues [22, 17]. In particular, further studies on the spatial coherence of S-MMGs across various skeletal muscles could lead to objective techniques to measure the mechanical properties of skeletal muscles, such as muscle stiffness [63, 62]. To this end, the influence of muscular fatigue occurring during voluntary contractions on the spatial coherence of S-MMG requires further quantification. This study investigates the possibility of using S-MMG to determine mechanical properties of skeletal muscle, in addition to this, joint measurement of S-MMG and EMG can be investigated to determine electromechanical coupling as well as determining the localization of the source of mechanical vibrations. The spatial coherence of S-MMGs in humans with movement disorders (*e.g.* spasticity due to spinal cord injury or stroke) would be an

important field of study for the quantification of muscle stiffness. Additionally, localization of the strength of coherence in S-MMGs between sensor pairs may provide further insights into the potential mechanical compartmentalization that may be due to either localized mechanical properties or localized muscle activity [65] and possible dependency/independency between adjacent muscles or partitions [25, 70, 72].

3.5 Conclusions

The variations of the spatial coherence of S-MMG waves across frequency appear to be closely linked to the S-MMG physiological generation mechanism as well as the local elastic properties of the studied muscle. Meaning, the frequency dependency of the coherent S-MMG waves was found to correlate to the physiological basis of muscle force generation. Hence, further studies of the spatial coherence of S-MMG across various muscles could lead to objective measurement techniques of the mechanical properties of skeletal muscles. For different muscles, the same approach can be taken with a few details changed, such as the sensor separation distance and the frequency of interest. Muscles with more slow twitch high endurance muscle fibers would have a lower frequency of interest, if the majority of the force generation is done by the recruitment of these muscle fibers. To this end, the influence of muscular fatigue occurring during voluntary contractions on the spatial coherence of S-MMG requires further quantification. In the study, for the 10 s of data collected there was no clear trend developed that showed the link between spatial coherence of the S-MMG waves and the length of time of the sub-maximal contraction. Additionally, localization of the strength of coherence in S-MMG between sensor pairs may provide further insights into the potential mechanical compartmentalization that may be due to either localized mechanical properties or localized muscle activity [65] and possible dependency/in-dependency between adjacent muscles or partitions [25, 70, 72]. Finally, S-MMG recorded on single sensor, have typically been used in physiological

studies to monitor the mechanical activity of skeletal muscles, in complement to standard surface electromyograms (EMG) which monitor the muscle's electrical activity. But the characteristics of low-frequency mechanical waves ($<$ 100 Hz here), such as velocity or attenuation, propagating in viscoelastic soft tissues (such as muscle) strongly depend on the local rheological properties of the soft tissues (e.g. compressibility, stiffness) [2]. For instance mechanical waves propagate faster in locally stiffer area [34, 24, 31]. Consequently, S-MMG, which correspond physically to propagating vibrations along the muscle, could allow for passive measurements of the skeletal muscle viscoelastic properties [45, 59, 63, 22] despite the random-looking appearance of the S-MMG time-series.

3.6 Summary

This work is expected to provide an innovative technique in determining the directionality (transverse or longitudinal) of S-MMGs propagation in skeletal muscle. It provides fundamental information that helps in determining sensor placement when S-MMG measurement is used to determine muscle in-vivo viscoelastic properties. This chapter focused on determining the directionality of the propagating S-MMG waves, also determined how these S-MMG waves vary with frequency, sensor separation distance as well as muscle contraction level. Using a 2 dimensional grid of single axis accelerometers placed on the skin above the biceps brachii muscle, these characteristics of S-MMG waves are explored.

Fifteen miniature accelerometers were used to measure S-MMGs on 10 healthy male subjects. A two dimensional 3 $\times$ 5 grid of accelerometers were placed on the subjects arm between 18% and 50% of the subjects L_m. Subjects completed three trials and contracted for 10 s at 20%, 40% and 60% of the maximum voluntary contraction (MVC).

The directionality of the S-MMG propagation are investigated by analyzing the

similarity between the recorded signal at different points on the 2-dimensional 3 $\times$ 5 grid. The spatial coherence is used to analyze the S-MMG's dependency on frequency, sensor separation distance, muscle contraction level and finally directionality. Similarity between sensor pairs located along the longitudinal axis of the muscle is compared to the similarity between sensor pairs located transversely across the long axis of the muscle. The study concluded that the frequency dependency of the coherent S-MMG waves was found to correlate to the physiological basis of muscle force generation. Meaning, at higher frequencies (closer to the mean power frequency) the spatial coherence of sensors along the longitudinal axis is higher than the spatial coherence across the transverse axis of the muscle.

CHAPTER IV

INFLUENCE OF THE ISOMETRIC CONTRACTION LEVEL ON THE SPATIAL COHERENCE OF S-MMG ALONG THE BICEPS LONGITUDINAL AXIS

4.1 Introduction

The two previous chapters have given much needed information on the characterization of S-MMG. Early in the development of measuring muscle activity by measuring S-MMGs, studies have mostly focused on measuring S-MMG with single sensors. Recently, an array of sensors have been used, but only to investigate the spatial distribution of the amplitude of the signal [46, 27, 17]. This is the first work that has been done to characterize the three dimensional components of S-MMG, as well as investigate the idea of wave propagation and to determine the direction of propagation. By characterizing these traveling waves, it lays the foundation work to study the traveling waves to determine a parameter that can effectively track the changes in the muscle's mechanical environment.

The work in this chapter utilizes the results from the previous chapters by using a linear array of one dimensional accelerometers aligned longitudinally along the biceps brachii muscle. Cross correlating signals received at different sensors that are a part of an array of sensors can potentially provide information about the medium in which the wave is traveling, mainly the speed at which the wave is traveling [75, 63, 62]. Different methods can be used to extract information from the cross correlation of the sensor array. One such method is to track from one reference sensor the decay over range of the cross correlation values at time t=0, which can lead to the fitting of an equation to determine the Green's function [52]. This method was investigated

but was found to not be a good fit for the experimental data. The results from this method can be found in Appendix B. Another method that can be implemented to investigate the properties of the medium is to find the maximum value of the cross correlation with one reference sensor for increasing range. The maximum value of the cross correlation along the longitudinal line of the biceps brachii has shown to increase with an increase in contraction level, according to a previous study [5]. Therefore, a function can be fit to the experimental data that can track the change in the coherence as the contraction level changes. The parameter of this function that changes may be related to the stiffness of the muscle and potentially lead to a non-invasive, passive elastography technique.

4.2 Methods

4.2.1 Subjects

Ten healthy and right-handed men (age: 29 ± 5 years, height: 175 ± 9 cm, body mass: 71 ± 8 kg), with no overt sign of neuromuscular diseases, volunteered to participate in the present study and signed an informed consent form. This study was conducted according to the protocol approved by the Institutional Review Board of the Georgia Institute of Technology.

4.2.2 Experimental Setup

The experimental setup and protocol for this study were the same as stated in Chapter 3. The data used here was the same data collected from the experiment in Chapter 3. Also, the results from Chapter 3 showed that the main propagation measured was longitudinal on the center sensor line, therefore only the center longitudinal sensor line was used in this study, which can be seen in Figure 42.

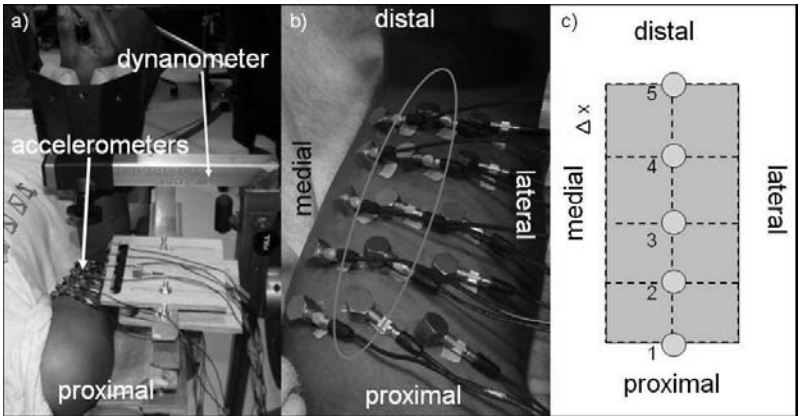

Figure 42: a) Experimental set-up for isometric elbow flexion tests (without sensor). b) Top view with skin-mounted accelerometers. c) Schematic of the 15 accelerometers locations. Only the center line of sensors (6-10) were used in this study (circled in (b) and (c)).

4.2.3 Data Preprocessing

All 5 channels for the recording of S-MMGs were time synchronized with a sampling frequency of 1 kHz (Compact DAQ system, National Instrument®, Austin, TX) and were amplified with a gain of 200. Data were filtered in the frequency band ($f_1 = f_{MP}$ and $f_2 = f_{MP}$+30 Hz) using a second order Butterworth bandpass filter. In addition, frequency whitening with a Hanning window was performed for this frequency range of interest. This frequency range was chosen to include the frequencies which represent local muscle fiber activity and not whole limb motion or muscle tremor, since the local muscle fiber activity causes the propagating component of the vibrations which leads to characterizing the muscle properties. In this study the frequency range of interest was subject dependent. It was selected as a 30 Hz frequency band with the lower limit being the mean power frequency.

4.2.4 Common metrics to track muscle activity

The root mean squared (RMS) of S-MMG has previously been used to track the increase in muscle activity during isometric voluntary contractions [35]. The RMS

value of a signal is defined below,

$$RMS = \sqrt{\frac{1}{N}\sum_{i=1}^{N} l_i^2} \tag{13}$$

where N is the total number of data points recorded in the signal and l_i is the acceleration recorded at a single sampling point, i. In this chapter there are two different RMS values considered, RMS 1 and RMS 2. RMS 2 is the above equation with the values filtered in the frequency band of interest, which is the mean power frequency (for each subject at 20% MVC) plus 30 Hz. This frequency range was selected to be large enough to include the range of local muscle fiber activity, but not too large that it includes a high level of noise. An analysis of the frequency band selection is showin the the Results section. RMS 1 is the equation above without filtering, which is what most studies report. In addition to the S-MMG RMS, the mean power frequency, as defined by Eq. (6), has shown to also be a good indicator of muscle activity.

4.2.5 Definition of the cross correlation for S-MMG

The cross correlation is a time domain measure of the similarity between two recorded signals. In this study, $l(t)$ and $m(t)$ are the S-MMGs recorded at two different sensor locations. The cross correlation of these two S-MMGs were taken as given by Eq. 14. The magnitude of the time-domain cross-correlation function was normalized between +1 and 0, where +1 indicates a perfect similarity between the two signals.

$$R_{lm}(\tau) = \frac{\int_{-T/2}^{T/2} l(t)m(t+\tau)\mathrm{d}t}{\sqrt{\int_{-T/2}^{T/2} l^2(t)\mathrm{d}t \int_{-T/2}^{T/2} m^2(t)\mathrm{d}t}} \tag{14}$$

To insure that only good quality data was used, there was a signal to noise ratio (SNR) threshold of 4 set in order to use the data from a pair of sensors. The SNR was determined by finding the maximum value of the envelope of the cross correlation

in the time window of 1 second centered at $t = 0$ (Δt_{signal}), and dividing it by one standard deviation of the cross correlation during a 4 second time window between 1-5 seconds (Δt_{noise}). Figure 43 shows an example of a cross correlation of sensor pair #6 & #7 (for subject 1, trial 1 and contraction level of 60% MVC), where the maximum value of the normalized cross correlation is well above the noise floor (dashed line). If the SNR did not meet this threshold, the data for those sensor pairs were not used in the calculation.

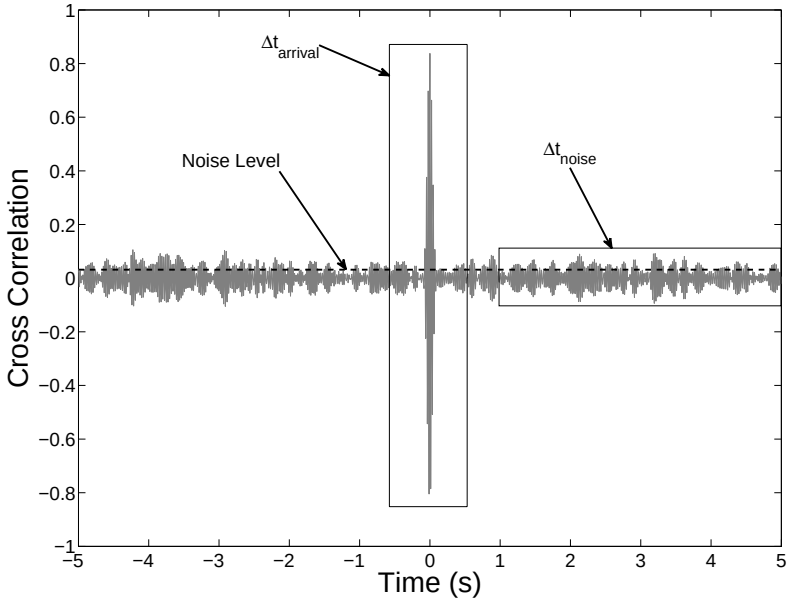

Figure 43: Example of the cross correlation of sensor #6 & #7 (for subject 1, trial 1 and contraction level of 60% MVC), showing the signal amplitude compared to the noise level.

After the coherence values were determined to be obtained from qood quality data, the values from the same sensor separation distance were averaged for an individual subject, trial and contraction level. For example, the coherence values between sensors #6 & #7, #7 & #8, #8 & #9 and #9 & #10 were averaged, as they all had a sensor separation distance of Δx. How these coherence values vary with sensor separation distance can provide information about the muscle. The coherence values were found

to decay with increasing distance Δx. A simple exponential decay, $e^{\frac{-x}{\xi}}$, was used as a fit to the experimental data, which has been used previously to describe the decay of correlations [81].

4.2.6 Statistical Analysis

Statistical analysis was performed to determine if there was statistical significance to the values of f_{MP} and RMS. The f_{MP} and RMS were found for each sensor and averaged across the 5 sensors for each trial. The 3 trials were then averaged to give a single f_{MP} and RMS value for each subject at each contraction level. These values were then averaged and plotted with the error bars indicating one standard deviation. In addition, statistical analysis was performed to determine if there was statistical significance to the coherence length, ξ. The coherence length was averaged for the three trials for each subject and contraction level. A one way analysis of variance (ANOVA) was used to determine statistical significance with the dependent variables being f_{MP}, RMS and ξ, and the independent variable being contraction level. To determine the main effect of contraction level on f_{MP}, RMS and ξ, these values were averaged across trials and subjects. An alpha level of 0.05 was used for all statistical comparisons, and where appropriate $P < 0.05$ and $P < 0.01$ was noted. Unless otherwise stated, the error bars in the figures represent one standard deviation.

4.3 Results

The coherence length, ξ, was found to increase with increasing contraction level. The coherence length is defined as the distance at which the coherence dropped by a factor of 1/e. An example of the coherence versus distance for multiple contraction levels is shown in Figure 44(a) (for subject 8, trial 1), with experimental data expressed as the data points and the lines represented as the exponential decay fit. Figure 44(b), shows the coherence averaged across trials and subjects for each contraction level. It can be seen that the main effect of sensor separation distance caused the coherence to

decrease when the sensor separation distance increased for 40% MVC and 60% MVC.

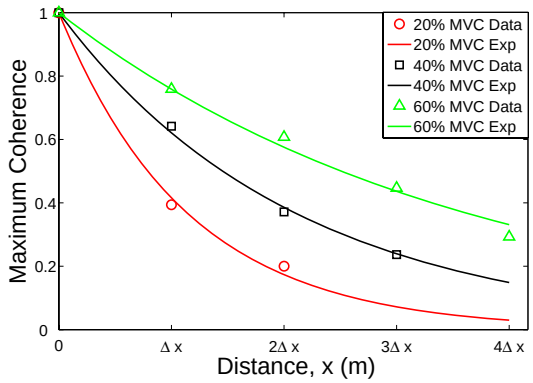

(a)

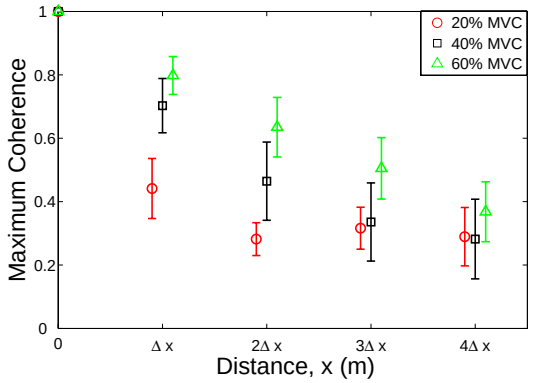

(b)

Figure 44: (a) Example of coherence versus distance plot for multiple contraction levels with experimental data (data points) and the exponential fit (lines) $e^{\frac{-x}{\xi}}$ (for subject 1 and trial 2), where x is the sensor separation distance and (b) the coherence averaged across trials and then subjects versus distance, this shows the main effect of sensor separation distance for the individual contraction levels.

Two parameters that were selected in examining the signals that may have an effect on the value of ξ were the frequency band and the SNR threshold selected. The effect of these parameters was investigated. Firstly, the SNR threshold used to select valid cross correlations did not have a significant effect on the results of the coherence length, ξ. Secondly, Figure 46(a) shows how the width of the frequency band affects ξ. In this analysis, the center frequency was held constant for each subject at $f_{MP}^{20\%}$ + 15 Hz, while the frequency bandwidth was increased from 5 Hz to 30 Hz. The mean

power frequency averaged across sensors, trials and subjects for 20%, 40% and 60% MVC are 27.4 ± 3.0 Hz, 30.9 ± 3.2 Hz and 33.7 ± 3.5 Hz, respectively. The center frequency selection was done in order to assure that when the frequency bandwidth is increased to 30 Hz, it doesn't include a-synchronous muscle activity at the lower frequencies ($f < 15$ Hz). Figure 47 shows an example of the the frequency analysis with the f_{MP} being 20 Hz, where the frequency ranges investigated are denoted by the horizontal yellow bar.

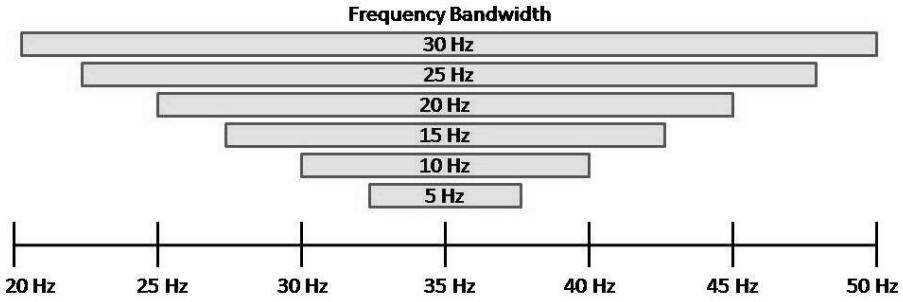

Figure 45: Example of frequency analysis for analyzing the effect of bandwidth size with the same center frequency.

The main effect of frequency bandwidth is shown here in Figure 46(a), meaning that the values of ξ were averaged across trials, contraction levels, and then subjects.

The value of ξ showed to decrease for an increased frequency bandwidth ($P < 0.05$). Post-hoc analysis revealed that there is a statistically significant difference between ξ with a 25 and 30 Hz frequency bandwidths with respect to ξ with a 5 Hz bandwidth ($P < 0.05$). There was no other statistically significant difference among the frequency bandwidths. There was also no statistically significant difference in the error vs frequency bandwidth.

Figure 47 explains the next frequency analysis method by showing an example of the analysis with the f_{MP} being 20 Hz, where the frequency ranges investigated are denoted by the horizontal yellow bar. The top portion of the diagram shows the analysis with the increasing frequency band with increasing frequencies, while

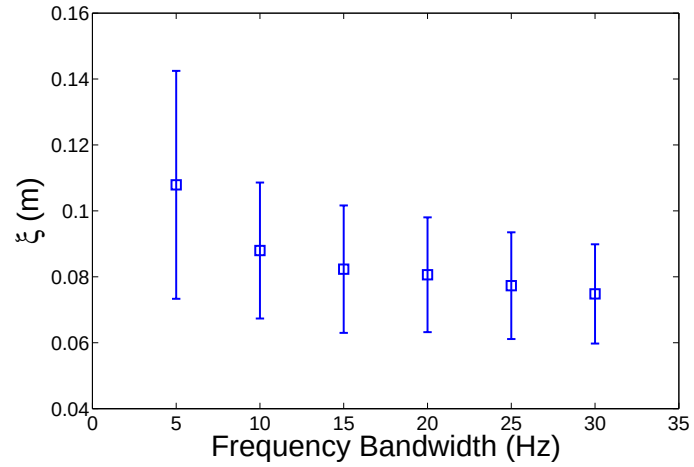

(a)

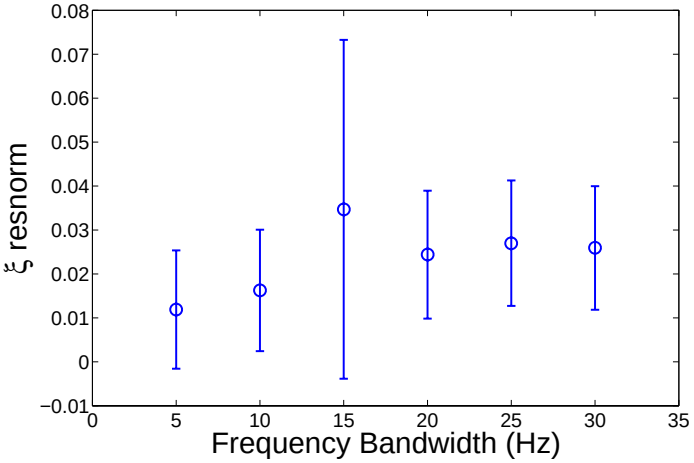

(b)

Figure 46: (a) The coherence length ξ versus increasing frequency bandwidth, with same center frequency of $f_{MP}^{20\%}$ + 15 Hz and (b) the error (resnorm) of the fit of ξ with increasing frequency bandwidth. Both values are averaged across all, trials, contraction levels and subjects.

the bottom portion of the diagram shows the analysis with the increasing frequency band, but decreasing frequencies. Figure 48(a) shows how the coherence length varies for an increasing frequency bandwidth both for increasing frequencies and decreasing frequencies. The frequency range is the same as the previous analysis with the lower bound being f_{MP} and the upper bound being f_{MP} + 30 Hz. At a specific frequency band the increasing frequencies have a higher ξ than the decreasing frequencies ($P <$

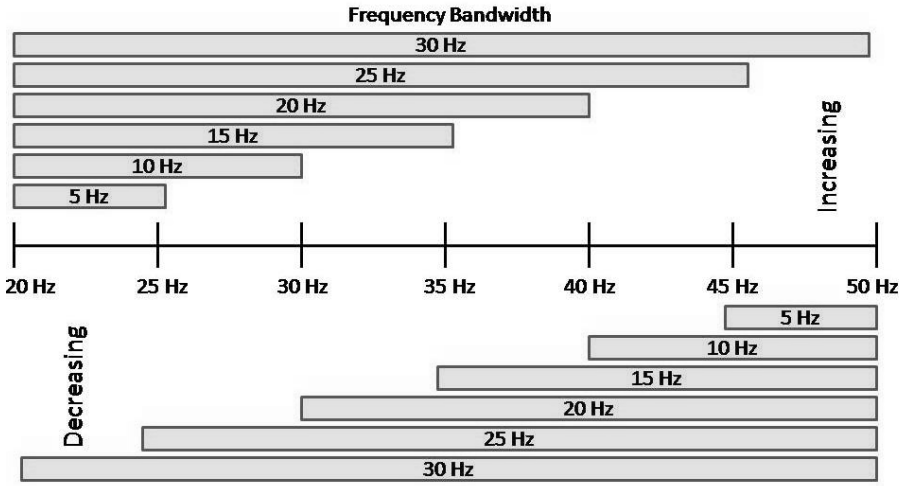

Figure 47: Example of frequency analysis for analyzing the effect increasing the frequency bandwidth. The frequency range here is analyzed for increasing the upper bound (for increasing) and decreasing the lower bound (for decreasing).

0.05). The decreasing frequencies always include higher frequency content information than the increasing frequencies, thus resulting in a lower ξ value. The fact that the frequency bandwidth is wider does not solely influence the coherence length. Which frequencies are included in the analysis is more important than the frequency bandwidth. For example, a 10 Hz frequency bandwidth with a center frequency at 45 Hz will have a lower ξ than a 10 Hz frequency bandwidth with a center frequency at 25 Hz.

It was also investigated how the center frequency affected the coherence length. Figure 49 shows how the coherence length and the error changes for increased center frequency for three different frequency bands (10 Hz, 20 Hz and 30 Hz). The actual band used is subject dependent, therefore in this figure the lower frequency bound is the mean power frequency (at 20% MVC) plus the x-axis value. For example, if the mean power frequency (at 20% MVC) for one subect is 25 Hz, then a value on the x-axis of 10 for a 10 Hz band corresponds to the frequency range of 35-45 Hz. With frequency as the main effect, there was a statistically significant decrease in ξ with an increase in frequency range ($P < 0.01$).

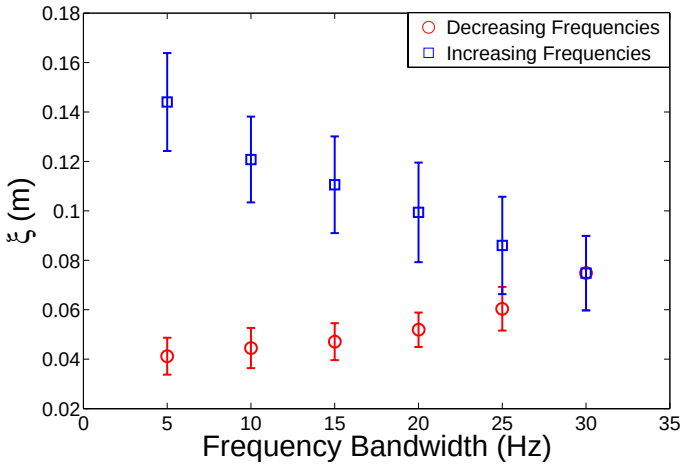

(a)

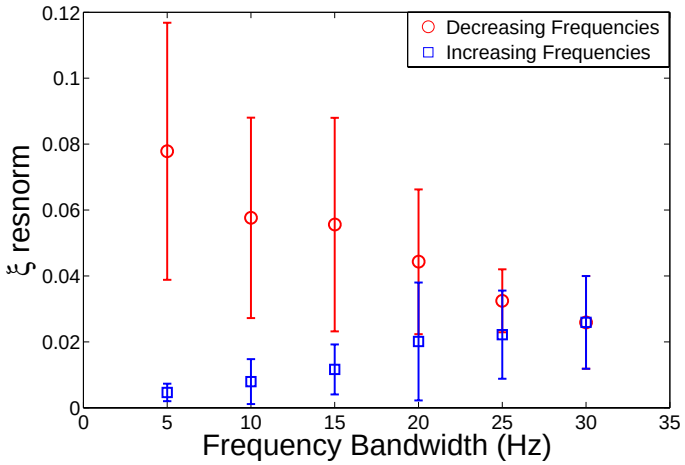

(b)

Figure 48: (a) The coherence length for increasing frequency bandwidth for both increasing and decreasing center frequencies and (b) the corresponding error (resnorm) of the fit for increasing frequency bandwidth for both increasing and decreasing center frequencies.

The findings revealed during the frequency analysis; 1) that the only statistically significant difference for increased frequency band is between ξ at 5 Hz and 25 and 30 Hz (meaning there is no difference between 10, 15, 20, 25 and 30 Hz when compared to each other), 2) the higher frequencies with the same frequency band have a lower coherence length than the lower frequencies and 3) for a constant frequency bandwidth, the coherence length decreased as the frequency range increased. In order

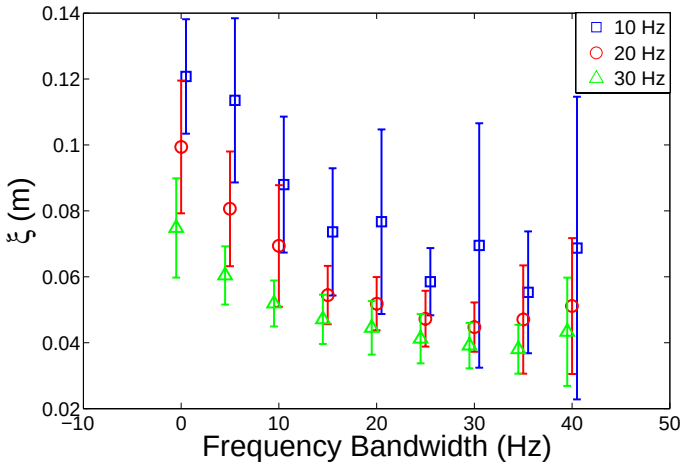

(a)

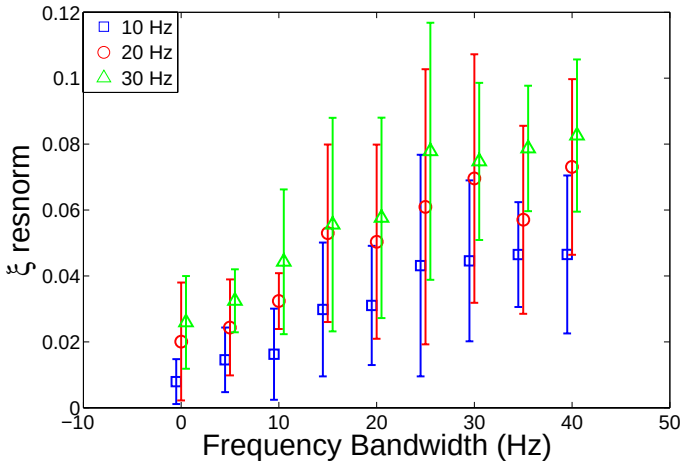

(b)

Figure 49: (a) The coherence length for increasing center frequency for three different frequency bandwidths (10 Hz, 20 Hz and 30 Hz) (b) the corresponding error (resnorm) of the fit for increasing center frequency for three different bandwidths (10 Hz, 20 Hz and 30 Hz).

to fully capture a wide range of muscle fiber activity, including slow and fast twitch fibers, for the remainder of this analysis the value of ξ was determined in a frequency bandwidth of 30 Hz, with the lower bound being f_{MP}. Doing this allows for the inclusion of the frequencies at which there is no synchronous muscle fiber activity, but does not allow for frequencies that are too high ($f > 70$ Hz) where there is not much signal.

The value of ξ reflects the changes in the muscle activity. Figure 50(a) shows an example for one subject on how the value of ξ changes with an increase in muscle contraction level for three different trials. As can be seen, there is nearly a linear increase, therefore a linear model was used and the slope of the linear model was recorded. This slope was then averaged across the three trials per subject. The results of the averaged slopes for each of the ten subjects are shown in Figure 50(b). It can be seen here that all of the slopes are on the same order of magnitude. This indicates that the slope of the coherence length versus contraction level fit is potentially stable across subjects.

The RMS value for each recording was calculated by equation 13 and averaged across sensors (sensors $\#6 - \#10$), trials and subjects, which showed how the RMS value changes with increased contraction intensity (see Fig. 51(a)). The mean power frequency was calculated by equation 6 and averaged across sensors (sensors $\#6 - \#10$), trials and subjects to show how the mean power frequency increased with increased contraction level ($P < 0.01$, see Fig 51(b)). Figure 51(c) shows the coherence length, ξ, increased as the contraction level increased when averaged across trials and subjects vs contraction intensity ($P < 0.01$).

The mean power frequency increased with increased contraction level from 27.43 $\pm$ 3.1 Hz at (20% MVC) to 30.98 $\pm$ 3.2 Hz (40% MVC) to 33.70 $\pm$ 3.5 Hz (60% MVC, $P < 0.01$), there was a statistically significant difference between the values at 20% and 60% MVC. For the RMS metric, both RMS 1 ($P < 0.05$) and RMS 2 ($P < 0.05$) were found to increase with increased contraction level. There was only a statistically significant difference between the value at 20% and 40% MVC with respect to 60% MVC. The calculated value of ξ was found to increase with increased contraction level from 4.41 $\pm$ 0.5 cm (20% MVC) to 7.05 $\pm$ 2.3 cm (40% MVC, $P < 0.05$) to 10.22 $\pm$ 3.30 cm (60% MVC, $P < 0.01$), with a statistically significant difference between each contraction level. These three metrics at some level seem to indicate a change

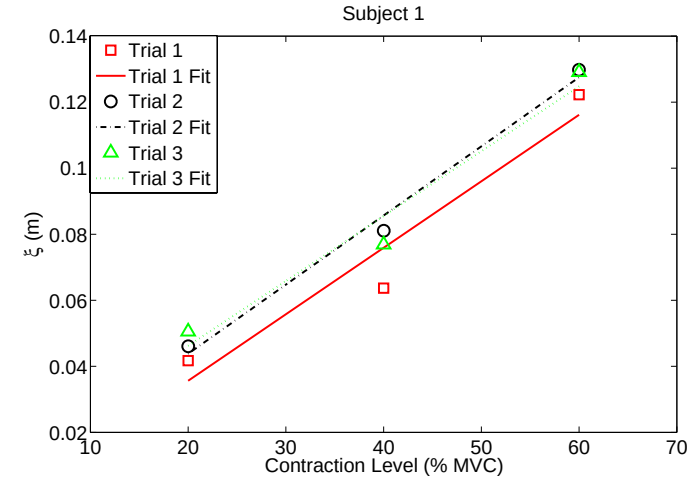

(a)

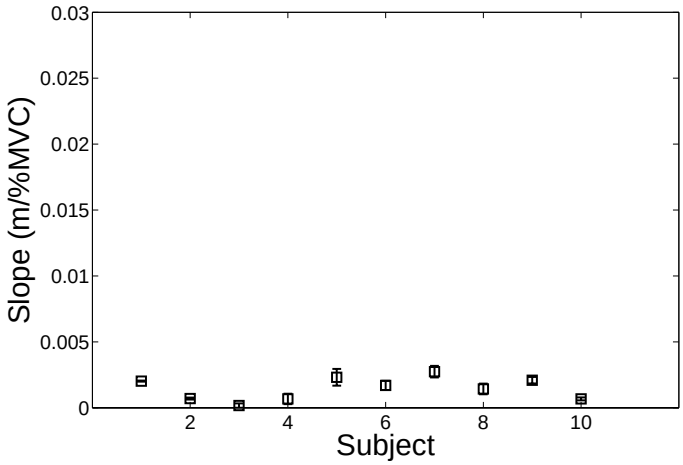

(b)

Figure 50: (a) Example of ξ vs contraction level for one subject, including linear fit (b) the slope of the linear fit for each subject, averaged across trials, with bandwidth of 30 Hz.

in muscle activity, since they change with contraction level. A direct comparison of these three metrics can be found in Figure 52. For each metric, the value at each contraction level was normalized by dividing it by the value of that metric at 60% MVC for each individual subject. Therefore, each metric has a maximum value of 1 at the corresponding 60% MVC contraction level for that metric. With the comparison of these metrics in this manner, looking at RMS 1, MPF and ξ, the coherence length ξ is the most sensitive metric to the change in contraction level. When the RMS

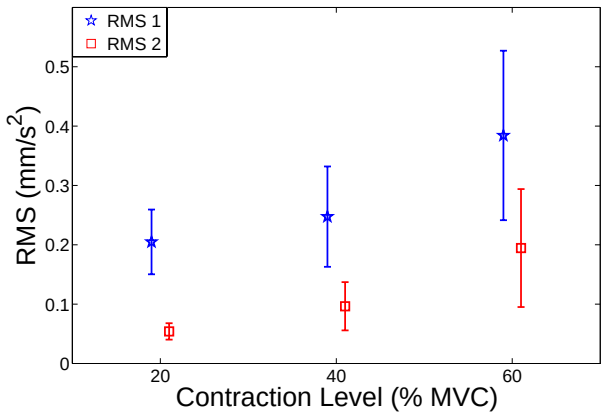

(a)

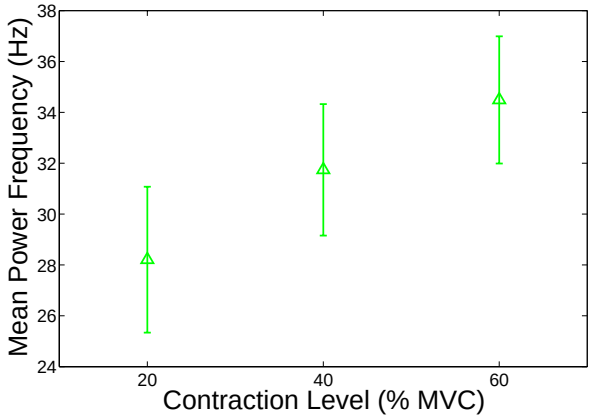

(b)

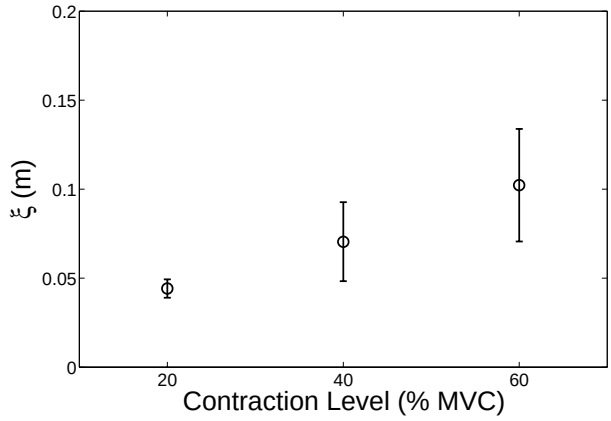

(c)

Figure 51: Effect of contraction level (% MVC) on (a) mean power frequency (b) root mean squared of filtered data (c) ξ from fitting coherence vs. distance curve. All values were averaged first across trial and then across subjects.

2 of the filtered data is included, it seems to be most sensitive to the changes in contraction level (indicated by the greater slope).

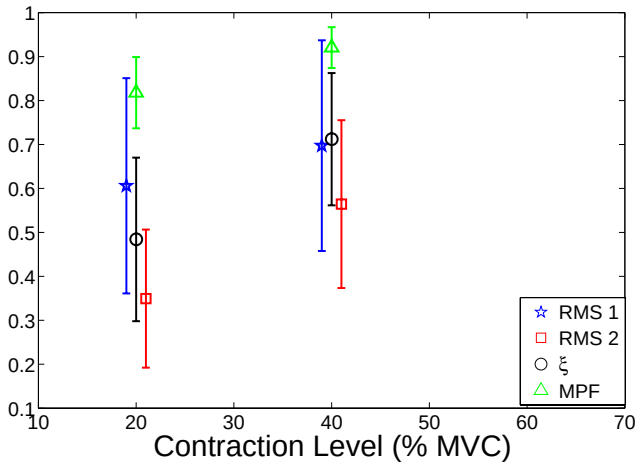

(a)

Figure 52: Tracking metrics RMS, f_{MP} and ξ for increasing contraction intensity, normalized to their respective 60% MVC values. The values were normalized to the 60% MVC value for each individual subject and then averaged across subjects. The error bars indicate one standard deviation.

4.4 Discussion

The change in skeletal muscle local activity directly reflects a change in the muscle's mechanical environment and condition. With sub-maximal isometric contractions, changes in the local muscle activity can be found when there is an increase in contraction level. The main finding of this chapter is that by using wave physics and cross correlation techniques, the coherence length, a metric to track the change in the muscle condition, was determined. The coherence length was found to significantly increase as the contraction level increased. A supplemental finding that supports the main finding is that two other metrics, the mean power frequency and the root mean square, both increase with increased contraction level. Two additional findings were also obtained in this study. Firstly, the signal to noise ratio threshold did not have a significant effect on the coherence length, ξ. Secondly, the coherence length, ξ, at

5 Hz was statistically different from ξ at 25 and 30 Hz only.

The main finding can be explained by wave physics and the physiological origin of the S-MMG. Previous studies have shown that the muscle stiffens as the contraction level increases during an isometric contraction [71]. This then explains why the coherence length increased with an increase in the contraction level, it is reflecting the change in the stiffness of the muscle. The RMS and mean power frequency have also been shown to track the changes in contraction level during isometric contractions. These two metrics are not as related to the overall stiffness of the muscle as is the coherence length, but are related to the local muscle fiber activity. They do however confirm that in this experiment, during increased contraction, the local muscle activity behaves how it is expected.

The first additional finding, that the SNR does not significantly effect the coherence length, may result from the very high signal to noise ratio for the smaller sensor separation distances. The sensor pairs with a sensor separation distance of $3\Delta x$ and $4\Delta x$ mainly have the lowest SNR. If a subject's data does not surpass the SNR threshold, it is not used. When a cross correlation peak of two sensors that are $4\Delta x$ apart is omitted because it did not pass the SNR threshold, it will not greatly affect the fitting of ξ in the exponential decay ($e^{\frac{-x}{\xi}}$).

Based on the second additional finding, it appears that the decrease in the coherence length with increasing frequency band between 25 and 30 Hz with respect to 5 Hz, can be attributed to the muscle fiber activity in certain frequency bands. High frequency S-MMGs are mostly dominated by a-synchronous muscle fiber activity that reflect the physiological architecture of the skeletal muscle. As the frequency increased to a region where there is less muscle fiber activity, the coherence decreased. A consistent decrease in the values of the cross correlation peak for increasing sensor separation distance will cause the exponential fit of the coherence length, ξ, to decrease. For a complete frequency analysis, the affect of the center frequency was

measured. It showed that, no matter the frequency band the coherence length decreased as the frequency range increased. This shows that the coherence length is indeed sensitive to the frequency selection. Selection of the frequency band should be done in a way that it encompasses the frequency ranges of the anticipated muscle fiber activity, or the muscle fiber activity of interest.

4.5 Conclusions

Overall the results of this study show that the propagation features of S-MMG vibrations reflect the architecture and contraction level of the biceps brachii muscle. The coherence length was found to significantly increase with increased contraction level for all ten of the subjects. While the mean power frequency and the RMS are two metrics that may successfully track the increase in muscle fiber activity, the coherence length can be related to the stiffness and homogeneity of the skeletal muscle during isometric contractions. Hence S-MMG could potentially be used for monitoring physiological changes of skeletal muscles.

4.6 Summary

This chapter used the results from the previous two chapters as the foundation for the developments presented. The setup used the S-MMG measurements from a linear array of five one-dimensional accelerometers oriented along the longitudinal axis of the biceps brachii muscle. There were 7 healthy male subjects that participated in this study. After the maximum voluntary contraction was obtained, the subjects contracted their biceps brachii muscle for three trials at 20%, 40% and 60% MVC for 10 s. These signals were then cross correlated and the peaks where plotted versus the sensor separation distance. It was found that there was a systematic decrease of the cross correlation peak as the sensor separation distance increased. Different functions were fitted to the data including a linear fit, sinusoidal fit, bessel fit and an exponential decaying fit. It was found that the exponential decaying fit best

represented the experimental data. From the exponential decaying fit of $e^{\frac{-x}{\xi}}$, the coherence length, ξ, was determined. This coherence length was found to increase when the contraction level was increased from 20% to 40% to 60% MVC. Being that the cross correlation detects a traveling wave, it may be that the coherence length is related to the properties of the medium that the wave is traveling in, such as the stiffness of the muscle. The coherence length was found to have a nearly linear increase as the contraction level increased. The coherence length, ξ, versus contraction level were fit with a linear fit, and the slopes for each trial was averaged for the individual subjects. These slopes varied from 0.02 to 0.10 (m/% MVC). Indeed these results are promising and may lead to a low cost, non-invasive, passive elastography technique.

CHAPTER V

CONCLUSION AND RECOMMENDATIONS FOR FUTURE WORK

5.1 Conclusions

The work in this dissertation lays the foundation for the development of a low cost, passive, non-invasive elastography by analyzing and processing S-MMGs measured with one dimensional accelerometers. The dissertation was separated into three different aims. Aim 1 focused on the 3-dimensional aspect of vibrations measured by accelerometers on the skin surface above the biceps brachii. It was found that the angles ϕ and θ were frequency dependent, seeing that the vibration power became more vertical as the frequency increased to the region where muscle fiber activity dominates. Since the goal of this work is to measure the vibrations created by the muscle fiber activity, it is sufficient to measure only the z-component of the biceps (normal to the skin). In addition, with increased contraction level, the S-MMG total power becomes more in-plane (decreased ϕ). It was also noted that at the most distal sensor location, the S-MMG power is more lateral than the other sensor locations. The first finding lead to the experimental setup of using one-dimensional accelerometers to accomplish Aim 2.

The second study in this work focused on using one-dimensional accelerometers to determine the propagation direction of the propagating S-MMG waves. The architecture of the biceps brachii can be used to interpret the main finding. Which was determined that the spatial coherence was greater for longitudinal sensor pairs than transverse sensor pairs. The observed longitudinal directionality of the propagating S-MMG along the muscle fiber direction, which is consistent with a previous study

[62], is likely determined by the fusiform architectural organization of muscle fibers of the biceps brachii muscle [78] as well as the mechanical properties and functionality of the muscle attachments and internal structure of the whole muscle. It should also be noted that the higher frequency content of S-MMG typically represents only a small fraction of the total energy of the raw S-MMG recorded during voluntary isometric contractions over skeletal muscles [54, 63]. For instance, previous studies of S-MMG recorded over the biceps brachii and further filtered in the band $2 - 80$ Hz, have showed that the mean power spectral frequency of those filtered S-MMG is typically lower than 30 Hz, even at high contraction level (up to 60% MVC) [15, 54]. Hence, this may explain why an earlier study of S-MMG coherence of the biceps brachii [59] concluded on a transverse wave propagation of S-MMG since it was focusing on more energetic lower frequency S-MMG components ($f < 30$ Hz) which were related to a bending transverse modal resonances of the biceps. Thus, the selected frequency bandwidth appears as an important parameter when investigating the specific directionality (e.g. longitudinal vs. transverse) and spatial origin (e.g. proximal vs. distal) of S-MMG recorded over skeletal muscles.

The conclusions from Aim 1 and Aim 2 characterized the dimensional component power as well as the propagation direction of the propagating S-MMG. Using this newly developed knowledge on S-MMG, a method to analyze the propagating wave and develop a metric that can track the changes in the muscle was developed, namely, the coherence length, ξ. The coherence length was found to significantly increase with increased contraction levels for all seven of the subjects. While the mean power frequency and the RMS are two metrics that may successfully track the increase in muscle fiber activity. Thus the coherence length could potentially be related to the stiffness of the skeletal muscle during isometric contractions. It is noteworthy to address that the values of the coherence length, ξ, were all on the same order of magnitude for the different subjects. Though currently there is not a direct link

between the coherence length and the stiffness of the muscle, it can be shown that these values are reasonable between subjects.

Potential Benefits Over Other Methods

- Completely passive
- Low cost, as it only required 1D accelerometers
- Accelerometers can by miniaturized (eq. using MEMS sensors)
- Can be used to measure more than one muscle simultaneously
- May be used during dynamic exercise

5.2 Recommendations for Future Work

Further studies of the spatial coherence of S-MMG across various muscles could lead to objective measurement techniques of the mechanical properties of skeletal muscles. For different muscles, the same approach can be taken with a few details changed, such as the sensor separation distance and the frequency of interest. Muscles with more slow twitch high endurance muscle fibers would have a lower frequency of interest if the majority of the force generation is done by the recruitment of these muscle fibers. To this end, the influence of muscular fatigue occurring during voluntary contractions on the spatial coherence of S-MMG requires further quantification.

This method of determining the coherence length to track the changes of muscle activity can be expanded to other muscles. Muscles that are superficial, so that the vibrations of the muscle can be measured from the surface of the skin through a skin and fat layer can be tested with this method. For example, the tibialis anterior, triceps and vastus lateralis can all be felt from the surface of the skin above the muscle, so they are good candidates for using this method. There are some skeletal muscles that do not have a large part of the muscle directly under a skin and fat layer, and may

be blocked by another muscle. Muscles such as the tibialis posterior, rotator cuff or the brachialis are not good candidates for using this method, because measuring the vibrations caused by these muscles alone would prove to be very difficult.

Another direction which would prove useful to further expand on the work done here would be to use non-contact methods to measure S-MMG. Though the accelerometers used were light weight (1 g), there was still a mass loading artifact due to the mass of the accelerometers that may have affected the signal received. Though care was taken to limit the affect of the cables, the cables may have provided some drag. A non-contact sensor such as a laser vibrometer could be used to measure S-MMG. This would provide a solution to the mass loading and drag artifacts, but would introduce a new challenge. Care must be taken to ensure that the muscle stays in the same position. Since the laser is not in physical contact with the arm, the point of measurement can be changed with a slight movement in the limb. With this taken into consideration, using a laser vibrometer could provide useful information with regard to determining viscoelastic properties of skeletal muscles.

APPENDIX A

EFFECT OF SKIN THICKNESS

There was an investigation onto whether or not the thickness of the skin and fat layer (skin thickness) between the biceps brachii and the accelerometers had a traceable affect on the measurements of the different directional components. The mean power frequency f_{MP} of each of the directional components at 20% MVC, 40% MVC and 60% MVC for the 15 subjects was plotted in Figure 53. As seen in the figure, there is no trend in the mean power frequency versus skin thickness.

Since there was no clear trend found in the mean power frequency at the different contraction levels, another analysis was done that compared the mean power frequency SNR versus skin thickness. The mean power frequency SNR in this case is defined as the mean power frequency of each of the three contraction levels (20% MVC, 40% MVC and 60% MVC) divided by the mean power frequency at the baseline (0% MVC) (see Eq. 15). Perhaps there was a change in the f_{MP} relative to the baseline.

$$f_{MP}^{SNR,20} = \frac{f_{MP}^{20\%MVC}}{f_{MP}^{0\%MVC}} \tag{15}$$

For the X and Y directional components, it can be seen from Figure 54(a) & 54(b) that there is no clear trend of the mean power frequency SNR to the skin thickness. For the Z directional component, it seems as if the lower skin thickness results in a high mean power frequency SNR. This was not verified with stastical analysis. A one way ANOVA (with $P < 0.05$ being significant) was conducted with skin thickness as the main effect, and there was no statistical significant difference versus skin thickness.

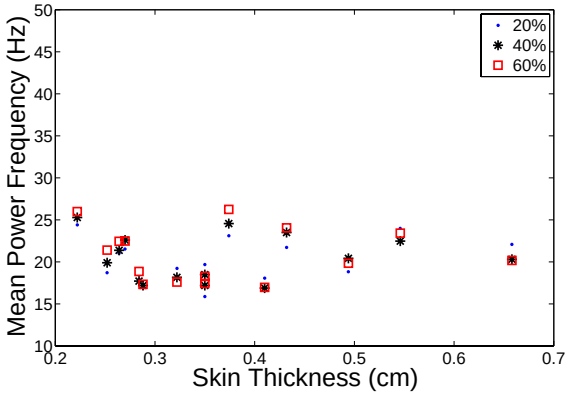

(a)

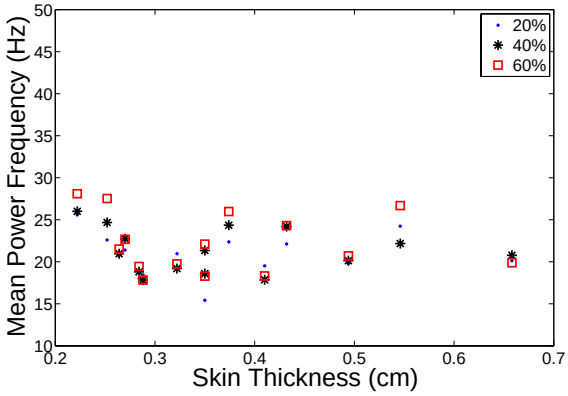

(b)

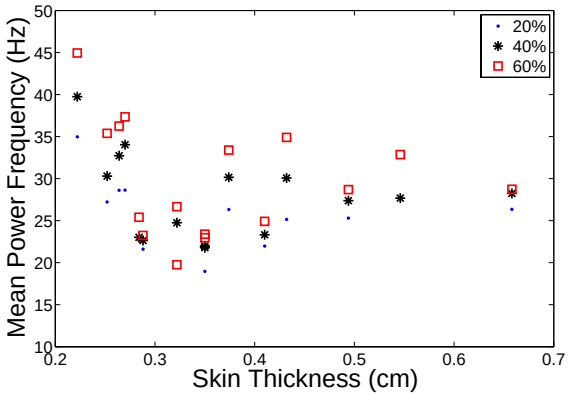

(c)

Figure 53: The mean power frequency versus the skin thickness for the (a) X directional component (b) Y directional component and (c) Z directional component

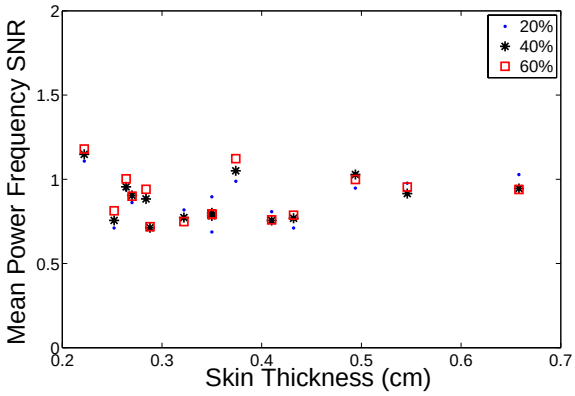

(a)

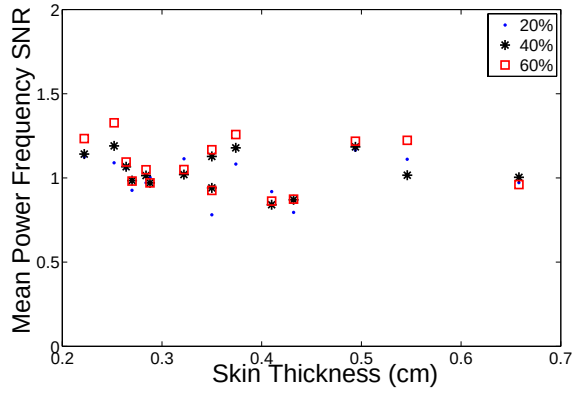

(b)

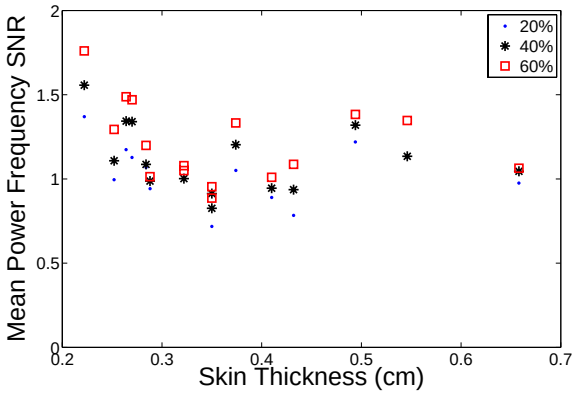

(c)

Figure 54: The mean power frequency SNR versus the skin thickness for the (a) X directional component (b) Y directional component and (c) Z directional component

APPENDIX B

PHYSICAL MODELS

The Green's function of the field between two sensors can be determined by cross correlating the measurement received at the two sensors, this has been showed experimentally in the fields of: ultrasonics ([44], and seismology ([13]). There also has been theoretical studies investigated using different developments [44, 73, 75]. The spatial correlation of ambient noise has been investigated theoretically in the frequency domain and offer expressions of the normalized cross correlation [4, 23, 74]. Using this method, Aki in 1957 developed a way to determine the phase velocity of micro-tremors in the field of seismology [4]. In determining some of the characteristics of the medium between the two receivers this suggest that the spatial coherence can be useful. A study shows that the Green's function of the wave equation can be determined from the normalized spatial correlation for isotropic incidence of waves in 1-D and 2-D. Also, for anisotropic incidence of waves, analytical expressions are presented for the retrieval of the Green's function [52].

B.1 Theory

This section discusses the theory behind analyzing the system as a one dimensional versus two dimensional distribution of sources.

B.1.1 1-D

For the 1-D case, consider two sinusoidal mutally uncorrelated plain waves incident from the positive and negative direction (see Fig.55) . It is assumed here that there is a constant wave velocity and no attenuation. With these paramaters the normalized

spatial coherence function of the wavefield can be seen as:

$$C_{12}(r,\omega) = Aexp\left(t\frac{\omega r}{c}\right) + Bexp\left(-t\frac{\omega r}{c}\right) \tag{16}$$

Where A and B are the power of the waves propagating in the positive and negative directions, respectively. The coefficients are normalized so that A + B = 1. If the energy is equal in the two waves, where A = B = $\frac{1}{2}$, then the normalized spatial coherence of the wavefield can be expressed as:

$$C_{12}(r,\omega) = \frac{1}{2}\left[exp\left(t\frac{\omega r}{c}\right) + exp\left(-t\frac{\omega r}{c}\right)\right] = cos\left(\frac{\omega r}{c}\right) \tag{17}$$

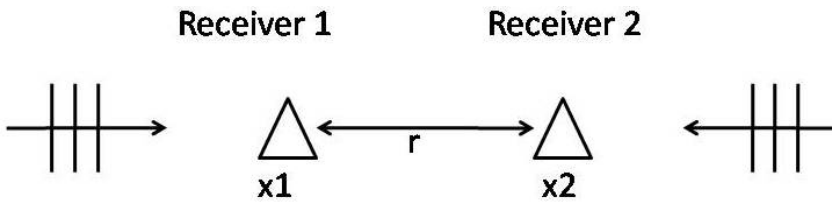

Figure 55: Two incident plane waves approaching two receivers from the opposite direction.

B.1.2 2-D

For the 2-D case (see Fig. 56), the normalized spatial coherence function of a wavefield can be expressed in the frequency domain as Eq. 18, [74, 23].

$$C_{12}(r,\omega) = \sum_{m=-\infty}^{\infty} i^m \gamma_m J_m\left(\frac{\omega r}{c}\right) e^{im\phi_{21}}, \tag{18}$$

where i is $\sqrt{-1}$, ϕ_{21} is the angle between the horizontal and the direction pointing from receiver 1 to receiver 2, $J_m(r)$ is the zeroth order Bessel function of the first kind and

$$\gamma_m \equiv \int_0^{2\pi} p(\phi) e^{-im\phi} d\phi, \tag{19}$$

where $p(\phi)$ is the probability density function for the power of the incident waves with respect to an azimuth of wave propagation direction (ϕ). $\gamma_{-m} = \gamma_m^*$, because $p(\phi)$ should be real. Therefore, Eq. 18 can be expressed as:

$$C_{12}(r,\omega) = \sum_{m=0}^{\infty} \varepsilon_m Re\left[\gamma_m e^{im\phi_{21}}\right] i^m J_m\left(\frac{\omega r}{c}\right) e^{im\phi_{21}}, \tag{20}$$

where ε_m is the Nuemann factor which is equal to 1 when m = 0. Assuming the equal partition of the power of the waves with various incident angles as $p(\phi) = \frac{1}{2\pi}$. For this case, $\gamma_m = \delta_{m0}$. Then,

$$C_{12}(r,\omega) = J_m\left(\frac{\omega r}{c}\right). \tag{21}$$

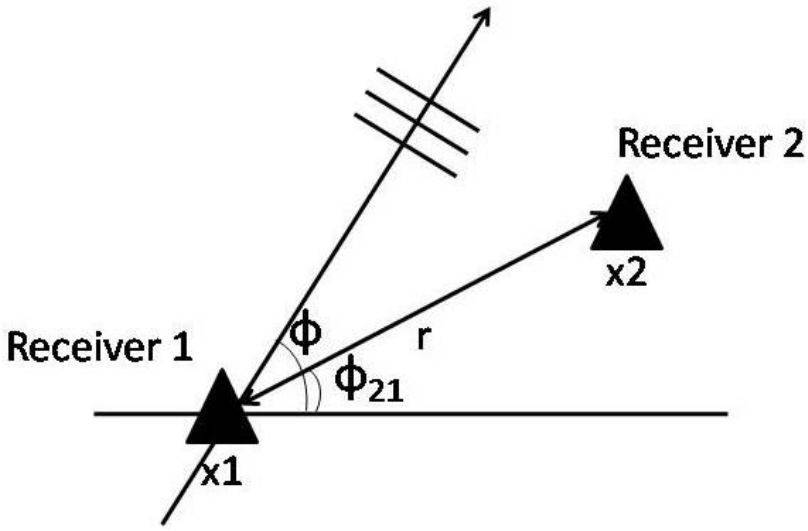

Figure 56: Two dimensional case of a plane wave with two receivers (adapted from [52]).

Table 1: Results from 1D and 2D simulation with random data.

	Acutal		Model				
Fitting Function	c	alpha	c bsl	bsl error	c cos	alpha	cos error
Cosine	5	10	4.43	0.52	4.58	12.19	0.0003
	10	10	5.22	0.34	9.20	11.23	0.00001
	15	10	10.15	0.05	13.80	10.99	0.000001
Bessel	5	10	4.88	0.66	6.88	8.12	0.002
	10	10	10.84	0.06	13.81	6.78	0.00
	15	10	14.17	0.01	20.12	6.69	0.00

B.2 Velocity Model

B.2.1 Simulation: Bessel Function vs. Cosine Function Model

A simulation was done in order to compare the ability of a given model to fit the data accurately. Two different source distributions were investigated, a 2-dimensional source distribution and a 1-dimensional source distribution. These source distributions represented two different environments for investigation, namely a rectangular flat plate and an infinitely long bar. The aim of this simulation was to determine if the correct model fit the determined source distribution best. This was determined by comparing the error calculated from the model fitting the simulated data.

For a two dimensional distribution of sources on a infinite rectangular plate, the mode shape is represented by a zeroth order bessel function of the first kind (see Eq.21). A two dimensional sources distribution was simulated as seen in Figure 57(b), where the inter sensor separation distance is .05 m which is approximately $\lambda/2$. The one dimensional source distribution the mode shape is represented by a cosine function (see Eq.16). In this case, the cosine function was multiplied by a decaying exponential term to account for attenuation.

Table 1, shows the results of the simulation. The results are for 3 different values of 'c' with alpha being held constant. In each case, though the error may have been lower, the correct fitting function had the closest value to the actualy 'c' that was used to create the data.

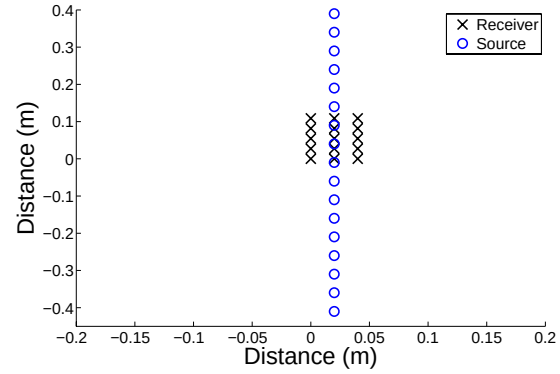

(a)

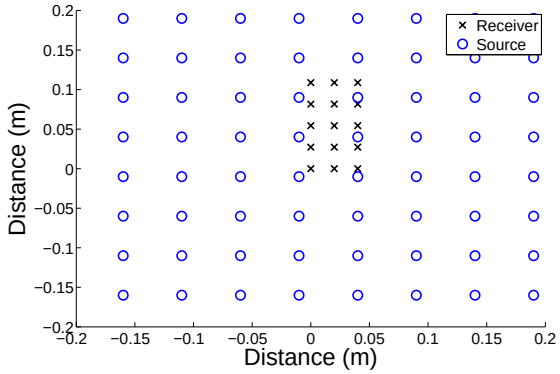

(b)

Figure 57: Sensor lay out along with source distribution for (a) 1-dimensional case and (b) 2 dimensional case

B.2.2 Bessel Function versus Cosine Function Fit

The cosine and bessel function were also investigated as fitting functions for the experimental data. Neither of these functions proved to be a correct model for the data. The values were not consistent, though the coherence increased for increasing contraction level, the 'c' values determined from these fits did not necessarily track that change. Below in table 2 with the results of the comparison between the consine function fit and the bessel function fit.

Table 2: Results from fitting the cosine function (1D) and the bessel function (2D) to the experimental data.

	Cosine Function Fit			Bessel Function Fit		
Sub	20% MVC	40% MVC	60% MVC	20% MVC	40% MVC	60% MVC
1	13.68 ± 0.11	13.52 ± 0	15.66 ± 0	6.42± 0.03	11.36 ± 0.08	14.09 ± 0.02
2	11.53 ± 0.12	15.96 ± 0.01	16.28 ± 0	6.93 ± 0.09	9.37 ± 0.02	11.97 ± 0.02
3	6.59 ± 0.20	14.53 ± 0.03	18.28 ± 0.02	4.33 ± 0.08	9.84 ± 0.13	13.64 ± 0.03
4	6.06 ± 0.27	30 ± 0	29.60 ± 0	4.55 ± 0.06	15.85 ± 0.04	17.89 ± 0.26
5	6.67 ± 0.32	25.43 ± 0.01	5 ± 2.04	5.93 ± 0.05	12.58 ± 0.08	17.21 ± 0.13
6	6.26 ± 0.31	5 ± 2.64	29.54 ± 0	6.50 ± 0.06	21.42 ± 0.03	21.28 ± 0.01
7	8.47 ± 0.05	12.17 ± 0.05	21.71 ± 0	5.03 ± 0.26	9.12 ± 0.11	13.56 ± 0.03

APPENDIX C

EQUIPMENT

Model Number	TRIAXIAL ICP® ACCELEROMETER	Revision: F
356A32		ECN #: 28478

Performance	ENGLISH	SI	
Sensitivity(± 10 %)	100 mV/g	10.2 mV/(m/s²)	
Measurement Range	± 50 g pk	± 491 m/s² pk	
Frequency Range(± 5 %)	1.0 to 4000 Hz	1.0 to 4000 Hz	
Frequency Range(± 10 %)	0.7 to 5000 Hz	0.7 to 5000 Hz	
Resonant Frequency	≥ 25 kHz	≥ 25 kHz	
Broadband Resolution(1 to 10,000 Hz)	0.0003 g rms	0.003 m/s² rms	[1]
Non-Linearity	≤ 1 %	≤ 1 %	[2]
Transverse Sensitivity	≤ 5 %	≤ 5 %	
Environmental			
Overload Limit(Shock)	± 5000 g pk	± 49,050 m/s² pk	
Temperature Range(Operating)	-65 to +250 °F	-54 to +121 °C	
Temperature Response	See Graph	See Graph	[1]
Base Strain Sensitivity	0.001 g/με	0.01 (m/s²)/με	[1]
Electrical			
Excitation Voltage	24 to 30 VDC	24 to 30 VDC	
Constant Current Excitation	2 to 20 mA	2 to 20 mA	
Output Impedance	≤ 200 ohm	≤ 200 ohm	
Output Bias Voltage	7 to 16 VDC	7 to 16 VDC	
Discharge Time Constant	0.4 to 1.5 sec	0.4 to 1.5 sec	
Settling Time(within 10% of bias)	<5 sec	<5 sec	
Spectral Noise(1 Hz)	95 μg/√Hz	932 (μm/s²)/√Hz	[1]
Spectral Noise(10 Hz)	20 μg/√Hz	196 (μm/s²)/√Hz	[1]
Spectral Noise(100 Hz)	6 μg/√Hz	58.9 (μm/s²)/√Hz	[1]
Spectral Noise(1 kHz)	3 μg/√Hz	29.4 (μm/s²)/√Hz	[1]
Spectral Noise(10 kHz)	2 μg/√Hz	19.6 (μm/s²)/√Hz	[1]
Physical			
Sensing Element	Ceramic	Ceramic	
Sensing Geometry	Shear	Shear	
Housing Material	Titanium	Titanium	
Sealing	Hermetic	Hermetic	
Size (Height x Length x Width)	0.45 in x 0.45 in x 0.45 in	11.4 mm x 11.4 mm x 11.4 mm	
Weight	0.19 oz	5.4 gm	[1]
Electrical Connector	8-36 4-Pin	8-36 4-Pin	
Electrical Connection Position	Side	Side	
Mounting Thread	5-40 Female	5-40 Female	
Mounting Torque	4 to 5 in-lb	45 to 55 N-cm	

CE [3]

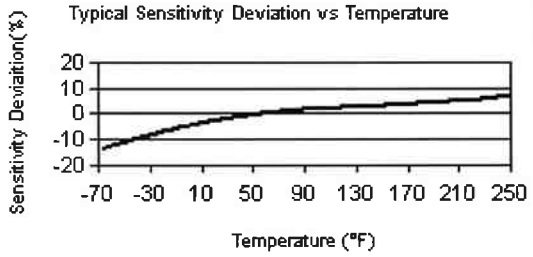

All specifications are at room temperature unless otherwise specified.
In the interest of constant product improvement, we reserve the right to change specifications without notice.

ICP® is a registered trademark of PCB Group, Inc.

OPTIONAL VERSIONS

Optional versions have identical specifications and accessories as listed for the standard model except where noted below. More than one option may be used.

T - TEDS Capable of Digital Memory and Communication Compliant with IEEE P1451.4

TLA - TEDS LMS International - Free Format

TLB - TEDS LMS International - Automotive Format

TLC - TEDS LMS International - Aeronautical Format

TLD - TEDS Capable of Digital Memory and Communication Compliant with IEEE 1451.4

Output Bias Voltage	7.7 to 17.0 VDC	7.7 to 17.0 VDC
Weight	.23 oz	6.4 gm
Mounting	Adhesive	Adhesive

NOTES:

[1] Typical.
[2] Zero-based, least-squares, straight line method.
[3] See PCB Declaration of Conformance PS023 for details.

SUPPLIED ACCESSORIES:

Model 034K10 4-cond. shielded cable, 10 ft (3 m), mini 4-pin plug to (3) BNC plugs (1)
Model 080A Adhesive Mounting Base (1)
Model 080A109 Petro Wax (1)
Model 081A27 Mounting Stud (5-40 to 5-40) (1)
Model 081A90 Mounting stud, 10-32 to 5-40 (1)
Model ACS-1T NIST traceable triaxial amplitude response, 10 Hz to upper 5% frequency. (1)
Model M081A27 Metric mounting stud, 5-40 to M3 x 0.50 long (1)

Entered:	Engineer:	Sales:	Approved:	Spec Number:
Date: 3-28-08	Date: 3-27-08	Date: 3-28-08	Date: 3-28-08	16563

PCB PIEZOTRONICS
VIBRATION DIVISION
3425 Walden Avenue, Depew, NY 14043

Phone: 716-684-0001
Fax: 716-685-3886
E-Mail: vibration@pcb.com

APPLICATION		
NEXT ASS'Y	USED ON	VAR

REVISIONS					
ZONE	REV	DESCRIPTION	ECN	DATE	APP'D
	A	REMOVE "PRELIMINARY"	10203	3/12/99	
	B	CHANGED CABLE	15112	4/8/02	
	C	UPDATED DRAWING	16633	12/31/02	

10427

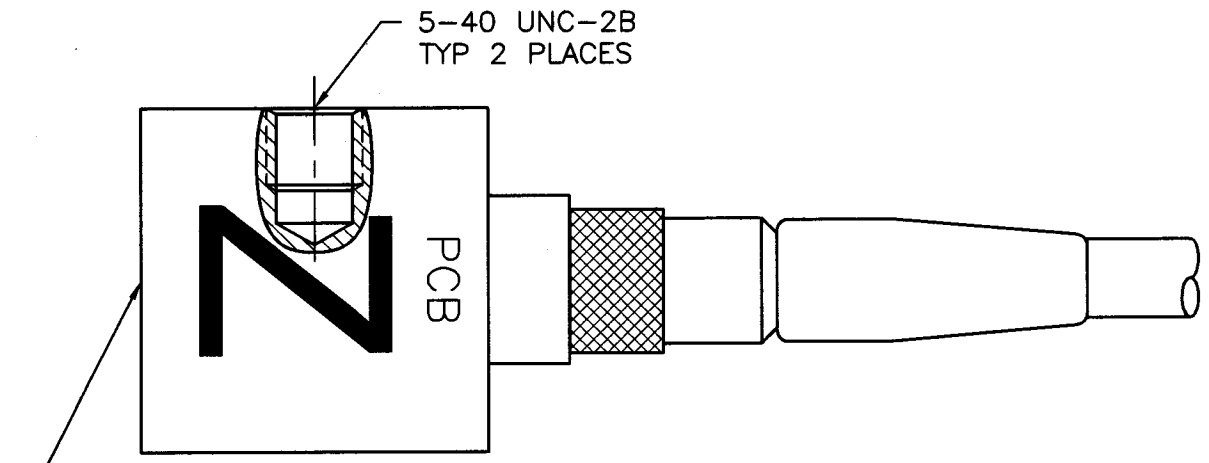

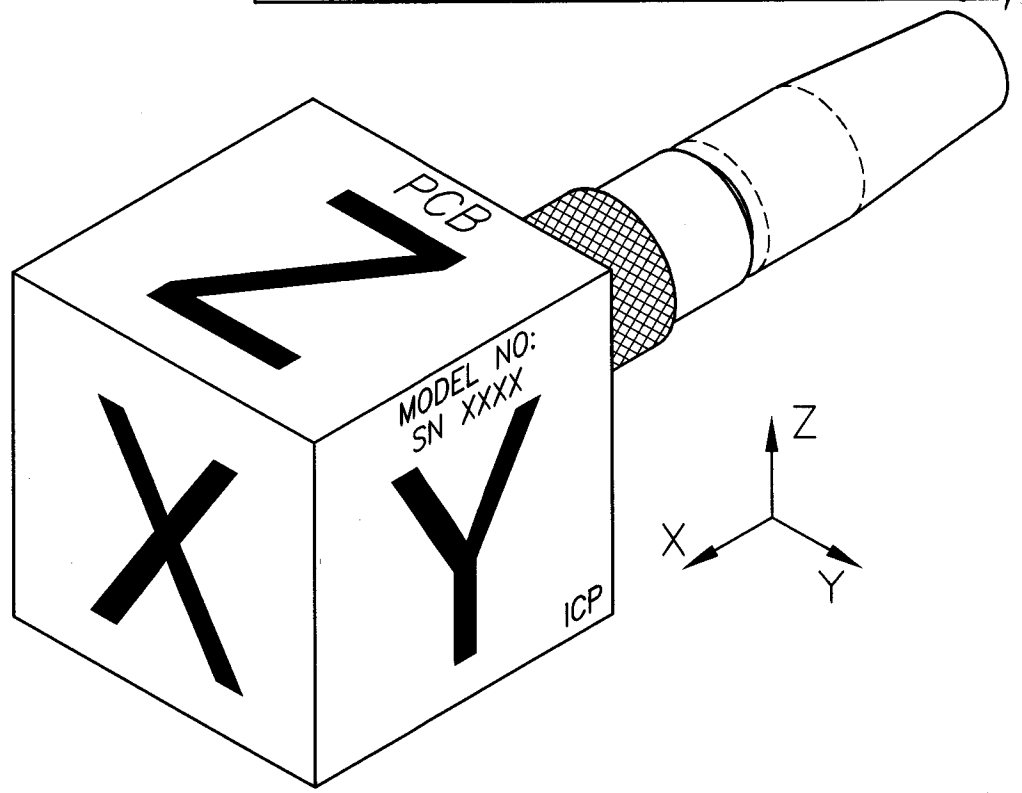

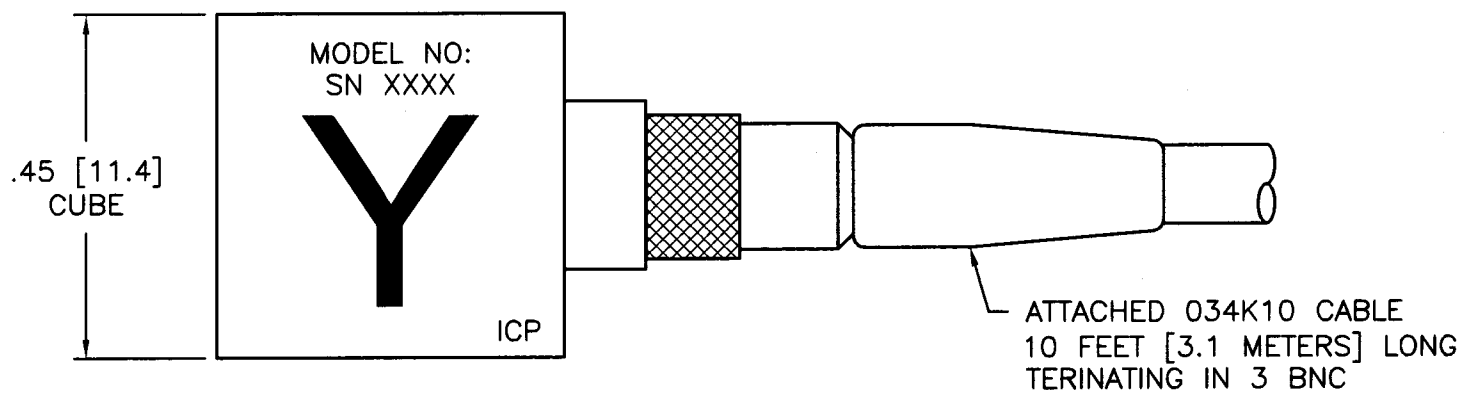

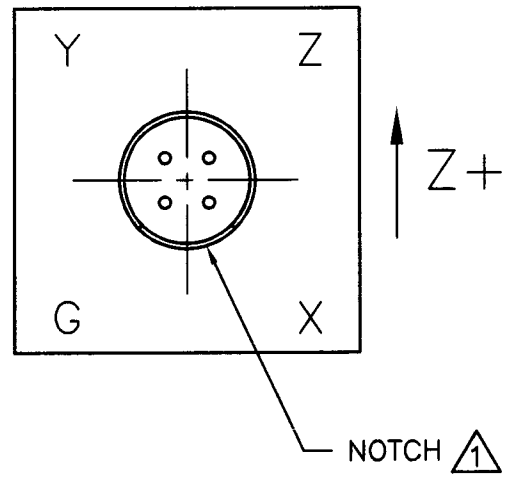

1 THIS VIEW SHOWN WITHOUT CABLE FOR PIN OUTPUT.

UNLESS SPECIFIED TOLERANCES	
DIMENSIONS IN INCHES DECIMALS XX ±.01 XXX ±.005 ANGLES ±2 DEGREES	DIMENSIONS IN MILLIMETERS [IN BRACKETS] DECIMALS XX ±0.3 XXX ±0.13 ANGLES ±2 DEGREES
FILLETS AND RADII .003 - .005	FILLETS AND RADII [0.07 - 0.13]
DD012 REV. B 03/13/98	

DRAWN		1/2/03	MFG	DC	1-9-3
CHK'D		1/9/03	ENGR		1/9/03
APP'D		1/10/3	SALES	CSA	1/9/03

TITLE: OUTLINE DRAWING
.45" CUBE W/ 8/36 4-PIN CONNECTOR
TRIAXIAL ACCELEROMETER

PCB PIEZOTRONICS
3425 WALDEN AVE. DEPEW, NY 14043
(716) 684-0001 EMAIL: SALES@PCB.COM

CODE IDENT. NO.	DWG. NO.	
52681	10427	
SCALE: 4X	SHEET 1 OF 1	

Model Number	ICP® ACCELEROMETER	Revision: L
352C65		ECN #: 16511

Performance	ENGLISH	SI	
Sensitivity (±10 %)	100 mV/g	10.2 mV/(m/s²)	
Measurement Range	±50 g pk	±491 m/s² pk	
Frequency Range (±5 %)	0.5 to 10000 Hz	0.5 to 10000 Hz	
Frequency Range (±10 %)	0.3 to 12000 Hz	0.3 to 12000 Hz	
Frequency Range (±3 dB)	0.2 to 20000 Hz	0.2 to 20000 Hz	
Resonant Frequency	≥35 kHz	≥35 kHz	
Phase Response (±5 °) (at 70° F [21° C])	2 to 6000 Hz	2 to 6000 Hz	
Broadband Resolution (1 to 10000 Hz)	0.00016 g rms	0.0015 m/s² rms	[1]
Non-Linearity	≤1 %	≤1 %	[3]
Transverse Sensitivity	≤5 %	≤5 %	[4]
Environmental			
Overload Limit (Shock)	±5000 g pk	±49050 m/s² pk	
Temperature Range (Operating)	-65 to +200 °F	-54 to +93 °C	[2]
Temperature Response	See Graph	See Graph	
Base Strain Sensitivity	<0.005 g/με	<0.05 (m/s²)/με	[1]
Electrical			
Excitation Voltage	18 to 30 VDC	18 to 30 VDC	
Constant Current Excitation	2 to 20 mA	2 to 20 mA	
Output Impedance	≤300 ohms	≤300 ohms	
Output Bias Voltage	8 to 12 VDC	8 to 12 VDC	
Discharge Time Constant	0.8 to 2.4 sec	0.8 to 2.4 sec	
Settling Time (within 10% of bias)	<10 sec	<10 sec	
Spectral Noise (1 Hz)	60 μg/√Hz	588 (μm/s²)/√Hz	[1]
Spectral Noise (10 Hz)	16 μg/√Hz	157 (μm/s²)/√Hz	[1]
Spectral Noise (100 Hz)	5 μg/√Hz	49 (μm/s²)/√Hz	[1]
Spectral Noise (1 kHz)	1.5 μg/√Hz	14.7 (μm/s²)/√Hz	[1]
Physical			
Sensing Element	Ceramic	Ceramic	
Sensing Geometry	Shear	Shear	
Housing Material	Titanium	Titanium	
Sealing	Welded Hermetic	Welded Hermetic	
Size (Hex x Height)	0.31 in x 0.42 in	7.9 mm x 10.7 mm	
Weight	0.070 oz	2.0 gm	[1]
Electrical Connector	5-44 Coaxial	5-44 Coaxial	
Electrical Connection Position	Side	Side	
Mounting Thread	5-40 Male	5-40 Male	
Mounting Torque	8 to 12 in-lb	90 to 135 N-cm	

CE [5]

Typical Sensitivity Deviation vs Temperature

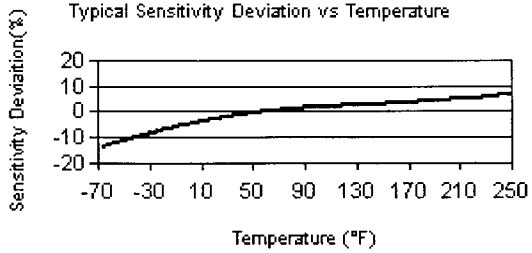

All specifications are at room temperature unless otherwise specified.
In the interest of constant product improvement, we reserve the right to change specifications without notice.

ICP® is a registered trademark of PCB Group, Inc.

OPTIONAL VERSIONS

Optional versions have identical specifications and accessories as listed for the standard model except where noted below. More than one option may be used.

A - Adhesive Mount [6]
Supplied Accessory : Model 080A90 Quick Bonding Gel (1) replaces Model 080A15

HT - High temperature, extends normal operation temperatures

Frequency Range (5 %)	5 Hz	5 Hz
Frequency Range (10 %)	3 Hz	3 Hz
Frequency Range (3 dB)	2 Hz	2 Hz
Temperature Range (Operating)	-65 to +250 °F	-54 to +121 °C
Discharge Time Constant	0.08 to 0.24 sec	0.08 to 0.24 sec
Broadband Resolution (1 to 10000 Hz)	0.0002 g rms	0.002 m/s² rms
Spectral Noise (1 Hz)	75 μg/√Hz	736 (μm/s²)/√Hz
Spectral Noise (10 Hz)	25 μg/√Hz	245 (μm/s²)/√Hz
Spectral Noise (100 Hz)	5 μg/√Hz	49 (μm/s²)/√Hz
Spectral Noise (1 kHz)	1.5 μg/√Hz	14.7 (μm/s²)/√Hz

J - Ground Isolated

Frequency Range (5 %)	8 kHz	8 kHz
Frequency Range (10 %)	10 kHz	10 kHz
Frequency Range (3 dB)	16 kHz	16 kHz
Resonant Frequency	≥30 kHz	≥30 kHz
Electrical Isolation (Base)	$>10^8$ ohms	$>10^8$ ohms
Size (Hex x Height)	0.37 in x 0.55 in	9.5 mm x 14.0 mm
Weight	0.1 oz	2.8 gm

M - Metric Mount

Mounting Thread	M3 x 0.50 Male	M3 x 0.50 Male

Supplied Accessory : Model M080A15 Adhesive Mounting Base (1) replaces Model 080A15

W - Water Resistant Cable

Electrical Connector	Sealed Integral Cable	Sealed Integral Cable
Electrical Connection Position	Side	Side

NOTES:

[1] Typical.
[2] 200°F to 250°F data valid with HT option only.
[3] Zero-based, least-squares, straight line method.
[4] Transverse sensitivity is typically <= 3%.
[5] See PCB Declaration of Conformance PS023 for details.
[6] Mounting stud removed, adhesive mounting base not required.

SUPPLIED ACCESSORIES:

Model 080A109 Petro Wax (1)
Model 080A15 Adhesive Mounting Base (1)
Model ACS-1 NIST traceable frequency response (10 Hz to upper 5% point).

Entered: DS	Engineer: DS	Sales: WDC	Approved: GM	Spec Number:
Date: 11/22/02	Date: 11/22/02	Date: 11/22/2	Date: 11/22/2	8339

PCB PIEZOTRONICS
VIBRATION DIVISION
3425 Walden Avenue, Depew, NY 14043
Phone: 716-684-0001
Fax: 716-685-3886
E-Mail: vibration@pcb.com

8242

APPLICATION		
NEXT ASS'Y	USED ON	VAR

REVISIONS				
REV	DESCRIPTION	ECN	DATE	APP'D
A	CORRECTED OVERALL HEIGHT	8962	4/7/98	KJS
B	ADDED POLARITY	25270	11/2/06	EB 11/06

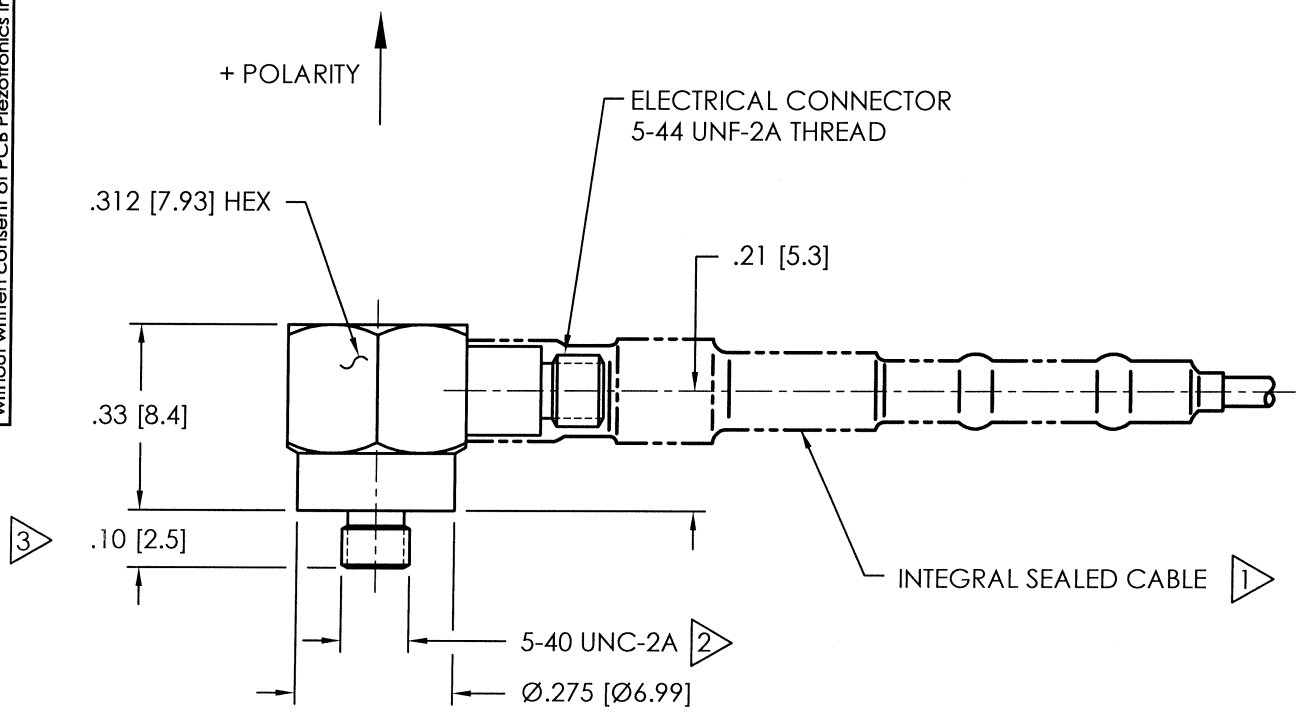

3 STUD REMOVED FOR SENSOR WITH ADHESIVE MOUNT OPTION.

2 M3 X 0.50-6g FOR SENSOR WITH METRIC OPTION.

1 ADD CABLE FOR SENSOR WITH WATER RESISTANT CONNECTOR OPTION.

UNLESS SPECIFIED TOLERANCES	
DIMENSIONS IN INCHES	DIMENSIONS IN MILLIMETERS [IN BRACKETS]
DECIMALS XX ±.03 XXX ±.010 ANGLES ±2 DEGREES	DECIMALS X ±0.8 XX ±0.25 ANGLES ±2 DEGREES
FILLETS AND RADII .003 - .005	FILLETS AND RADII [0.07 - 0.13]

DRAWN	[illegible]	11/2/06	MFG	Dan	11/3/06
CHK'D	ECB	11/3/06	ENGR	[illegible]	11/2/06
APP'D	EB	11/2/06	SALES	[illegible]	11/8/06

TITLE: OUTLINE DRAWING
MODEL 352C65 SERIES
ACCELEROMETER

PCB PIEZOTRONICS INC.
3425 WALDEN AVE. DEPEW, NY 14043
(716) 684-0001 EMAIL: SALES@PCB.COM

CODE IDENT. NO.	DWG. NO.
52681	8242
SCALE: 3X	SHEET 1 OF 1

REFERENCES

[1] "The signal processing toolbox ™: Magnitude squared coherence." The Mathworks ™, Oct 2007.

[2] Achenbach, J., *Wave Propagation in Elastic Solids*. Amsterdam, The Netherlands: Elsevier Science Publishers B.V., 1975.

[3] Akataki, K., Mita, K., Itoh, K., Suzuki, N., and Watakabe, M., "Acoustic and electrical activities during voluntary isometric contraction of biceps brachii muscles in patients with spastic cerebral palsy," *Muscle & Nerve*, vol. 19, pp. 1252–1257, 1996.

[4] Aki, K., "Space and time spectra of stationary waves, with special reference to microtremors," *Bulletin of the Earthquake Research Institute*, vol. 35, pp. 415–457, 1957.

[5] Archer, A. A., Atangcho, P., Sabra, K. G., and Shinohara, M., "Propagation direction of natural mechanical oscillations in the biceps brachii muscle during voluntary contraction," *Journal of Electromyography and Kinesiology*, vol. 22, no. 1, pp. 51 – 59, 2012.

[6] Barry, D. and Cole, N., "Muscle sounds are emitted at the resonant frequencies of skeletal muscle," *IEEE Transactions on Biomedical Engineering*, vol. 37, pp. 525–531, 1990.

[7] Basford, J. R., Jenkyn, T. R., An, K.-N., Ehman, R. L., Heers, G., and Kaufman, K. R., "Evaluation of healthy and diseased muscle with magnetic resonance elastography," *Archives of Physical Medicine and Rehabilitation*, vol. 83, no. 11, pp. 1530 – 1536, 2002.

[8] Baskin, R. J., "Volume change and pressure development in muscle during contraction," *American Journal of Physiology*, vol. 213, pp. 1025–1030, 1967.

[9] Beck, T. W., Dillon, M. A., DeFreitas, J. M., and Stock, M. S., "Cross-correlation analysis of mechanomyogram signals detected in two axes.," *Physiological Measurement*, pp. 1465–1471, 2009.

[10] Beck, T. W., Housh, T. J., Cramer, J. T., Weir, J. P., Johnson, G. O., Coburn, J. W., Malek, M. H., and Mielke, M., "Mechanomyographic amplitude and frequency responses during dynamic muscle actions: a comprehensive review.," *Biomedical Engineering Online*, vol. 4, pp. 1–27, 2005.

[11] Brown, T., Rack, P., and Ross, H., "Different types of tremor in the human thumb," *Journal of physiology-London*, vol. 332, no. , pp. 113–123, 1982.

[12] Brunetti, F., Rocon, E., Pons, J., and Manto, M., "The tremor coherence analyzer (tca): A portbale tool to asses instantaneous inter-muscle coupling in tremor," in *Proceedings of the 26th Annual International Conference of the IEEE EMBS*, pp. 61–64, 2004.

[13] Campillo, M. and Paul, A., "Long-range correlations in the diffuse seismic coda," *SCIENCE*, vol. 299, pp. 547–549, JAN 24 2003.

[14] Carter, G., "Coherence and time-delay estimation," *Proceedings of the IEEE*, vol. 75, pp. 236–255, 1987.

[15] Cescon, C., Farina, D., Gobbo, M., Merletti, R., and Orizio, C., "Effect of accelerometer location on mechanomyogram variables during voluntary, constant-force contractions in three human muscles," *Medical & Biological Engineering & Computing*, vol. 42, pp. 121–127, 2004.

[16] Cescon, C., Nannucci, L., and Orizio, C., "A prototype of hybrid probe for surface emg and mmg joint recordings.," in *In: Proceedings of the XIV Congress ISEK, Vienna, Austria*, pp. 299–300, 2002.

[17] Cescon, C., Madeleine, P., and Farina, D., "Longitudinal and transverse propagation of surface mechanomyographic waves generated by single motor unit activity," *Medical & Biological Engineering & Computing*, vol. 46, pp. 871–877, 2008.

[18] Cescon, C., Madeleine, P., Graven-Nielsen, T., Merletti, R., and Farina, D., "Two-dimensional spatial distribution of surface mechanomyographical response to single motor unit activity," *Journal of Neuroscience Methods*, vol. 159, pp. 19–25, 2007.

[19] Challis, R. and Kitney, R., "Biomedical signal-processing 3. the power spectrum and coherence function," *Medical & Biological Engineering & Computing*, vol. 29, pp. 225–241, 1991.

[20] Chen, D., Durand, L., and Bellemare, F., "Time and frequency domain analysis of acoustic signals from a human muscle," *MUSCLE & NERVE*, vol. 20, pp. 991–1001, 1997.

[21] Clamann, H., "Activity of single motor units during isometric tension," *Neurology*, vol. 20, no. 3, pp. 254–260, 1970.

[22] Cole, N. and Barry, D., "Muscle sounds frequencies of the frog are modulated by skeletal-muscle tension," *Biophysical Journal*, vol. 66, pp. 1104–1114, 1994.

[23] Cox, H., "Spatial correlation in arbitrary noise fields with application to ambient sea noise," *Journal of the Acoustical Society of America*, vol. 54, no. 5, pp. 1289–1301, 1973.

[24] Dresner, M., Rose, G., Rossman, P., Muthupillai, R., Manduca, A., and Ehman, R., "Magnetic resonance elastography of skeletal muscle," *Journal of Magnetic Resonance Imaging*, vol. 13, pp. 269–276, 2001.

[25] English, A., Wolf, S., and Segal, R., "Compartmentalization of Muscles and Their Motor Nuclei - The Partitioning Hypothesis," *Physical Therapy*, vol. 73, pp. 857–867, 1993.

[26] Esposito, F., Malgrati, D., Veicsteinas, A., and Orizio, C., "Time and frequency domain analysis of electromyogram and sound myogram in the elderly," *European Journal of Applied Physiology and Occupational Physiology*, vol. 73, pp. 503–510, 1996.

[27] Farina, D., Li, X., and Madeleine, P., "Motor unit acceleration maps and interference mechanomyographic distribution," *Journal of Biomechanics*, vol. 41, pp. 2843–2849, 2008.

[28] Fung, Y., *Biomechanics: Mechanical Properties of Living Tissues*. New York, New York: Springer-Verlag, 2 ed., 1988.

[29] Gardner, W. A., "A unifying view of coherence in signal processing," *Signal Processing*, vol. 29, no. 2, pp. 113 – 140, 1992.

[30] Gennisson, J.-L., Deffieux, T., Mac, E., Montaldo, G., Fink, M., and Tanter, M., "Viscoelastic and anisotropic mechanical properties of in vivo muscle tissue assessed by supersonic shear imaging," *Ultrasound in Medicine &; Biology*, vol. 36, no. 5, pp. 789 – 801, 2010.

[31] Gennisson, J., Catheline, S., Chaffai, S., and Fink, M., "Transient elastography in anisotropic medium: Application to the measurement of slow and fast shear wave speeds in muscles," *Journal of the Acoustical Society of America*, vol. 114, pp. 536–541, 2003.

[32] Goldenberg, M., Yack, H., Cerny, F., and Burton, H., "Acoustics myography as an indicator of force during sustained contractions of a small hand muscle," *Journal of Applied Physiology*, vol. 70, pp. 87–91, 1991.

[33] Graaff, K. V. D., *Human Anatomy*. New York, New York: McGraw-Hill, 6 ed., 2002.

[34] Greenleaf, J., Fatemi, M., and Insana, M., "Selected methods for imaging elastic properties of biological tissues," *Annual Review of Biomedical Engineering*, vol. 5, pp. 57–78, 2003.

[35] Guo, J.-Y., Zheng, Y.-P., Xie, H.-B., and Chen, X., "Continuous monitoring of electromyography (emg), mechanomyography (mmg), sonomyography (smg) and torque output during ramp and step isometric contractions," *Medical Engineering & Physics*, vol. 32, no. 9, pp. 1032 – 1042, 2010.

[36] Halliday, D., Rosenberg, J., Amjad, A., Breeze, P., Conway, B., and Farmer, S., "A framework for the analysis of mixed time series/point process data - theory and application to the study of physiological tremor, single motor unit discharges and electromyograms," *Progress in Biophysics & Molecular Biology*, vol. 64, no. 2-3, pp. 237–278, 1995.

[37] Huxley, H. E., "The mechanism of muscular contraction," *Science*, vol. 164, no. 3886, pp. 1356–1366, 1969.

[38] Ito, L., Kawakami, Y., Ichinose, Y., Fukashiro, S., and Fukunaga, T., "Nonisometric behavior of fascicles during isometric contractions of a human muscle," *Journal of Applied Physiology*, vol. 85, pp. 1230–1235, OCT 1998.

[39] Jaskolska, A., Madeleine, P., Jaskolski, A., Kisiel-Sajewicz, K., and Arendt-Nielsen, L., "A comparison between mechanomyographic condenser microphone and accelerometer measurements during submaximal isometric, concentric and eccentric contractions," *Journal of Electromyography and Kinesiology*, vol. 17, no. 3, pp. 336 – 347, 2007.

[40] Kwatny, E., Thomas, D. H., and Kwatny, H. G., "An application of signal processing techniques to the study of myoelectric signals," *IEEE Transactions on Biomedical Engineering*, vol. 17, pp. 303–313, 1970.

[41] Larose, E., Roux, P., and Campillo, M., "Reconstruction of Rayleigh-Lamb dispersion spectrum based on noise obtained from an air-jet forcing," *JOURNAL OF THE ACOUSTICAL SOCIETY OF AMERICA*, vol. 122, pp. 3437–3444, DEC 2007.

[42] Lieber, R., Steinman, S., Barash, I., and Chambers, H., "Structural and functional changes in spastic skeletal muscle," *MUSCLE & NERVE*, vol. 29, pp. 615–627, MAY 2004.

[43] Litwiller, D. V., Mariappan, Y. K., and Ehman, R. L., "Magnetic Resonance Elastography," *Current Medical Imaging Reviews*, vol. 8, pp. 46–55, Feb 2012.

[44] Lobkis, O. and Weaver, R., "On the emergence of the Green's function in the correlations of a diffuse field," *JOURNAL OF THE ACOUSTICAL SOCIETY OF AMERICA*, vol. 110, pp. 3011–3017, DEC 2001.

[45] Madeleine, P., Cescon, C., and Farina, D., "Spatial and force dependency of mechanomyographic signal features," *Journal of Neuroscience Methods*, vol. 158, pp. 89–99, 2006.

[46] Madeleine, P., Tuker, K., Arendt-Nielsen, L., and Farina, D., "Heterogeneous mechanomyographic absolute activation of paraspinal muscles assessed by a two-dimensional array during short and sustained contractions," *Journal of Biomechanics*, vol. 40, no. 12, pp. 2663–2671, 2007.

[47] Malhotra, S., Cousins, E., Ward, A., Day, C., Jones, P., Roffe, C., and Pandyan, A., "An investigation into the agreement between clinical, biomechanical and neurophysiological measures of spasticity," *CLINICAL REHABILITATION*, vol. 22, no. 12, pp. 1105–1115, 2008.

[48] Mason, P., "Dynamic stiffness and crossbridge action in muscle," *Biophysics of Structure & Mechanism*, vol. 4, pp. 15–25, 1977.

[49] Modules, S. T., "Structure of skeletal muscle." U.S. National Institutes of Health,National Cancer Institute, Jul 2012.

[50] Muscolino, J. E., *The Muscle and Bone Palpation Manual with Trigger Points, Referral Patterns and Stretching*. St. Louis, Missouri: Mosby, 2008.

[51] Muthupillai, R. and Ehman, R., "Magnetic resonance elastography," *Nature Medicine*, vol. 2, pp. 601–603, MAY 1996.

[52] Nakahara, H., "A systematic study of theoretical relations between spatial correlation and Green's function in one-, two- and three-dimensional random scalar wavefields," *GEOPHYSICAL JOURNAL INTERNATIONAL*, vol. 167, pp. 1097–1105, DEC 2006.

[53] Orizio, C., "Muscle sound - bases for the introduction of a mechanomyogram signal in muscle studies," *Critical Reviews in Biomedical Engineering*, vol. 21, no. 3, pp. 201–243, 1993.

[54] Orizio, C., *Surface Mechanomyogram (Chapter 11 of Electromyography: Physiology, Engineering, and Noninvasive Applications.)*. Wiley-IEEE Press, 2005.

[55] Orizio, C., Gobbo, M., Diemont, B., Esposito, F., and Veicsteinas, A., "The surface mechanomyogram as a tool to describe the influence of fatigue on biceps brachii motor unit activation strategy. Historical basis and novel evidence," *European Journal of Applied Physiology*, vol. 90, pp. 326–336, 2003.

[56] Orizio, C., Liberati, D., Locatelli, C., DeGrandis, D., and Veicsteinas, A., "Surface mechanomyogram reflects muscle fibres twitches summation," *Journal of Biomechanics*, vol. 29, pp. 475–481, 1996.

[57] Orizio, C. and Veicsteinas, A., "Soundmyogram analysis during sustained maximal voluntary contraction in sprinters and long-distance runners," *International Journal of Sports Medicine*, vol. 13, pp. 594–599, 1992.

[58] Oster, G. and Jaffe, J., "Low-frequency sounds from sustained contraction of human skeletal-muscle," *Biophysical Journal*, vol. 30, no. 1, pp. 119–127, 1980.

[59] Ouamer, M., Boiteux, M., Petitjean, M., Travens, L., and Sales, A., "Acoustic myography during voluntary isometric contraction reveals non-propagative lateral vibration," *Journal of Biomechanics*, vol. 32, pp. 1279–1285, 1999.

[60] Pappas, G., Asakawa, D., Delp, S., Zajac, F., and Drace, J., "Nonuniform shortening in the biceps brachii during elbow flexion," *Journal of Applied Physiology*, vol. 92, pp. 2381–2389, 2002.

[61] Romano, A. J., Abraham, P. B., Rossman, P. J., Bucaro, J. A., and Ehman, R. L., "Determination and analysis of guided wave propagation using magnetic resonance elastography," *Magnetic Resonance in Medicine*, vol. 54, no. 4, pp. 893–900, 2005.

[62] Sabra, K. G. and Archer, A., "Tomographic elastography of contracting skeletal muscles from their natural vibrations," *Applied Physics Letters*, vol. 95, 2009.

[63] Sabra, K. G., Conti, S., Roux, P., and Kuperman, W., "Passive in vivo elastography from skeletal muscle noise," *Applied Physics Letters*, vol. 90, 2007.

[64] Sabra, K., Roux, P., and Kuperman, W., "Arrival-time structure of the time-averiaged ambient noise cross-correlation function in an oceanic waveguide," *JOURNAL OF THE ACOUSTICAL SOCIETY OF AMERICA*, vol. 117, pp. 164–174, JAN 2005.

[65] Segal, R., "Neuromuscular compartments in the human biceps brachii muscle," *Neuroscience Letters*, vol. 140, pp. 98–102, 1992.

[66] Shapiro, N., Campillo, M., Stehly, L., and Ritzwoller, M., "High-resolution surface-wave tomography from ambient seismic noise," *SCIENCE*, vol. 307, pp. 1615–1618, MAR 11 2005.

[67] Shinohara, M., Kouzaki, M., Yoshihisa, T., and Fukunaga, T., "Mechanomyography of the human quadriceps muscle during incremental cycle ergometry," *European Journal of Applied Physiology and Occupational Physiology*, vol. 76, pp. 314–319, 1997.

[68] Shinohara, M., Kouzaki, M., Yoshihisa, T., and Fukunaga, T., "Mechanomyogram from the different heads of the quadriceps muscle during incremental knee extension," *European Journal of Applied Physiology*, vol. 78, pp. 289–295, 1998.

[69] Shinohara, M. and Sgaard, K., "Mechanomyography for studying force fluctuations and muscle fatigue," *Exercise and Sport Science Reviews*, vol. 34, pp. 59–64, 2006.

[70] Shinohara, M., "Muscle Activation Strategies in Multiple Muscle Systems," *Medicine and Science in Sports and Exercise*, vol. 41, pp. 181–183, 2009.

[71] Shinohara, M., Sabra, K., Gennisson, J.-L., Fink, M., and Tanter, M., "Real-time visualization of muscle stiffness distribution with ultrasound shear wave imaging during muscle contraction," *Muscle & Nerve*, vol. 42, pp. 438–441, Sep 2010.

[72] Shinohara, M., Yoshitake, Y., and Kouzaki, M., "Alterations in Synergistic Muscle Activation Impact Fluctuations in Net Force," *Medicine and Science in Sports and Exercise*, vol. 41, pp. 191–197, 2009.

[73] Snieder, R., "Extracting the Green's function from the correlation of coda waves: A derivation based on stationary phase," *PHYSICAL REVIEW E*, vol. 69, APR 2004.

[74] Teal, P., Abhayapala, T., and Kennedy, R., "Spatial correlation for general distributions of scatterers," *IEEE SIGNAL PROCESSING LETTERS*, vol. 9, pp. 305–308, OCT 2002.

[75] Wapenaar, K., "Retrieving the elastodynamic Green's function of an arbitrary inhomogeneous medium by cross correlation," *PHYSICAL REVIEW LETTERS*, vol. 93, DEC 17 2004.

[76] Watakabe, M., Mita, K., Akataki, K., and Ito, K., "Reliability of the mechanomyogram detected with an accelerometer during voluntary contractions," *Medical & Biological Engineering & Computing*, vol. 41, pp. 198–202, 2003.

[77] Weaver, R. and Lobkis, O., "Ultrasonics without a source: Thermal fluctuation correlations at MHz frequencies," *PHYSICAL REVIEW LETTERS*, vol. 87, SEP 24 2001.

[78] Winter, D. A., *Biomechanics and Motor Control of Human Movement*. New York, New York: John Wiley & Sons, 1990.

[79] Yoshitake, Y., Shinohara, M., Ue, H., and Moritani, T., "Characteristics of surface mechanomyogram are dependent on development of fusion of motor units in humans," *Journal of Applied Physiology*, vol. 93, pp. 1744–1752, 2002.

[80] Yoshitake, Y., Masani, K., and Shinohara, M., "Laser-detected lateral muscle displacement is correlated with force fluctuations during voluntary contractions in humans," *Journal of Neuroscience Methods*, vol. 173, pp. 271–278, 2008.

[81] Yu, Y., Taylor, P., and Terentjev, E., "Exponential decay of correlations in a model for strongly disordered 2D nematic elastomers," *Physical Review Letters*, vol. 81, pp. 128–131, Jul 6 1998.